

The Evolution of Cataclysmic Variable Stars

David I. Sahman

Department of Physics & Astronomy



*A dissertation submitted in candidature for the degree of
Doctor of Philosophy at the University of Sheffield*

June, 2018

I try to avoid looking backwards or forwards and try to keep looking upwards.

Charlotte Bronte.

Because I have contemplated explaining what I think, not only about the location and movement of this light, but also about its substance and origin, and believing that I have found an explanation that, for lack of evident contradictions, may well be true, I have finally arrived at the belief of being capable of knowing something about this wonder, beyond the point where pure conjecture ends.

Letter by Galileo to O. Castelli regarding the Stella Nova of 1604

In awe, I watched the waxing moon ride across the zenith of the heavens like an ambered chariot towards the ebony void of infinite space wherein the tethered belts of Jupiter and Mars hang, forever festooned in their orbital majesty. And as I looked at all this I thought... I must put a roof on this toilet.

Les Dawson

Declaration

I declare that no part of this thesis has been accepted, or is currently being submitted, for any degree or diploma or certificate or any other qualification at this University nor elsewhere.

This thesis is the result of my own work unless otherwise stated.

The following Chapters have been based on publications as shown below:

Chapter 2 - Sahman et al. (2013)

Chapter 3 - Sahman et al. (2015)

Chapter 4 - Sahman et al. (2018) in preparation.

Chapter 5 - Sahman et al. (2018)

Acknowledgements

There are so many people to thank that I hope I haven't forgotten anyone. Firstly, I owe so much to my supervisor, Prof. Vik Dhillon, who has supported and directed me so wisely over these last eight years. He is a truly dedicated astronomer with whom it has been an absolute pleasure to work, and whom I also feel honoured to be able to call a friend.

And then there are other people in the Astronomy Department at Sheffield who have been so helpful and patient with my often stupid questions, especially Stu Littlefair, followed very closely by Paul Kerry, our IT 'whizz'. When I started there was Clive, Paul, and Simon on the permanent staff, together with Cristina and David as postdocs. Since then the department has been steadily growing and we have been joined by James, Justyn, Richard, Katherine, Claire, Andy, Joachim and Steven.

My next task is to list all the PhD students with whom I have shared loads of laughs, meals and beers on our many nights out and the 'Astro does....' events! In no particular order, I am proud to have rubbed shoulders with Patricia, Marv, Krisada, Richard A., Edgar, Emile, Darren, Manu, Chris, Pav, Tim, Martin M., Martin D., Liam H., Liam G., Jonny, Lydia, Catherine, Becky, Emma, Heloise, Katie, Dan, and Rob. Thanks to all of you for making an old man feel very welcome!

I also have to record my love and gratitude to all members of my family who have actively supported me throughout this wonderful journey, especially my parents, who valued the joy of learning, providing my brothers and sisters and me with a house full of books and curiosity.

Finally, a huge thank you to Marion, for her unending love, support and encouragement, often in the form of cakes and other goodies!

Summary

Cataclysmic variables (CVs) are binary star systems comprising a white dwarf which is accreting material from a Roche-lobe filling companion, usually a late-main sequence or evolved star. The accreted material accumulates on the surface of the white dwarf and ultimately leads to a thermonuclear runaway explosion, called a nova eruption. There are ~ 400 recorded novae and some have shown more than one eruption. These systems are the recurrent novae, and they are one of the leading progenitor candidates of Type Ia Supernovae. In this thesis, I describe how I used high speed spectroscopy to determine the component masses of the stars in the eclipsing recurrent nova CI Aquilae. The masses I determined suggest it is indeed a progenitor of a Type Ia supernova, and will explode in 10 Myr.

The long term impact of nova events on the evolution of CVs is poorly understood, and may be the reason for the diversity of CV types observed at the same orbital period. One theory, known as hibernation theory, proposes that the nova event causes systems to cycle through the various classes of CVs, due to heating and bloating of the secondary. In the second part of this thesis, I undertook searches for nova shells around known CVs, in an effort to determine the frequency and life-cycle of novae. I examined over 150 systems and found one definite shell around V1315 Aquilae. I then used high-resolution spectroscopy to determine the mass and age of this shell. This is the first discovery of a nova shell around a novalike variable. By combining my search results with simulations and the results of other recent searches for nova shells, I find that the lifetime of the novalike state is broadly in line with the nova-induced cycle theory (hibernation theory).

Contents

1	Introduction	1
1.1	Cataclysmic variables - Overview	1
1.2	CV classifications	3
1.2.1	Classical and recurrent novae	3
1.2.2	Dwarf novae	4
1.2.3	Novalike variables	5
1.2.4	Magnetic CVs	5
1.2.5	Helium-rich systems	6
1.3	White dwarfs in CVs	6
1.3.1	Electron degeneracy	7
1.4	CV evolution	7
1.4.1	Pre-CV evolution	7
1.4.2	The canonical theory	8
1.4.3	Orbital period distribution	10
1.5	Angular momentum loss	13
1.5.1	Roche lobe geometry	13
1.5.2	Angular momentum	15
1.5.3	Response to mass transfer	17
1.5.4	Disrupted magnetic braking	19
1.5.5	Gravitational wave radiation	20
1.5.6	Consequential angular momentum loss	20
1.6	Novae characteristics	21
1.6.1	Galactic and extra-galactic novae	21
1.6.2	Light curve classification	23
1.6.3	Light curve speed classes	23
1.6.4	Spectral evolution	24
1.6.5	Nuclear fusion processes	25
1.6.6	Does the WD gain or lose mass during a nova eruption?	26
1.6.7	Nova shells	27

1.7	Nova induced cycle theory aka hibernation theory	30
1.8	CVs as progenitors of Type Ia Supernovae	32
1.8.1	WD with a main sequence or evolved companion	33
1.8.2	WD and WD pair	34
1.8.3	WD pair plus a third star	34
1.8.4	WD with the core remnant of a normal star	35
1.8.5	Single isolated WD	35
1.8.6	Observational evidence for SD and DD models	36
1.9	This Thesis	38
2	CI Aquilae: a Type Ia supernova progenitor?	39
2.1	Introduction	39
2.2	Observations	41
2.3	Data Reduction	42
2.4	Results	43
2.4.1	Light curves	43
2.4.2	Ephemeris and orbital period	44
2.4.3	Average spectrum	44
2.4.4	Trailed spectra and Doppler tomography	47
2.4.5	Radial velocity of the white dwarf	49
2.4.6	Radial velocity of the secondary star	53
2.4.7	Rotational velocity and spectral type of secondary star	56
2.4.8	Distance to CI Aql	60
2.4.9	System parameters	61
2.5	Discussion	66
3	Searching for nova shells around cataclysmic variables	71
3.1	Introduction	71
3.2	Observations	75
3.2.1	WHT Images	75
3.2.2	IPHAS Survey	76
3.3	Data reduction	82
3.3.1	WHT images	82
3.3.2	INT IPHAS images	82
3.4	Results	83
3.4.1	WHT images and radial profiles	83
3.4.2	IPHAS images	86
3.5	Discussion	92
3.5.1	Nova-like variables	93

3.5.2	Asynchronous polars	93
3.5.3	Future surveys	94
4	Searching for nova shells around cataclysmic variables II	96
4.1	Introduction	96
4.2	Observations	97
4.3	Data reduction	101
4.4	INT images and radial profiles	101
4.5	Combined results of our two campaigns and other recent work	102
4.6	Discussion	103
5	Discovery of an old nova shell surrounding the cataclysmic variable	
	V1315 Aql	110
5.1	Introduction	110
5.2	Observations	111
5.2.1	Keck DEIMOS spectra	111
5.2.2	<i>pt5m</i> – La Palma	112
5.3	Data Reduction	114
5.3.1	INT images	114
5.3.2	Keck DEIMOS spectra	114
5.3.3	<i>pt5m</i> images	114
5.3.4	Review of satellite imagery	115
5.4	Results	115
5.4.1	INT image	115
5.4.2	Geometry of the shell	116
5.4.3	Keck DEIMOS spectra	116
5.4.4	Emission lines	116
5.4.5	Systemic radial velocity of V1315 Aql	120
5.4.6	Radial velocities of shell emission lines	122
5.4.7	Line fluxes	123
5.4.8	Time of nova eruption	124
5.4.9	Temperature and density of the shell	125
5.4.10	Mass of the shell	125
5.5	Discussion	127
6	Conclusions and Future Work	128
6.1	Conclusions	128
6.1.1	Recurrent Novae as Progenitors of SNIa	128
6.1.2	Nova-induced cycle theory	130

6.2	Future work	131
6.2.1	Recurrent Novae as Progenitors of SNIa	132
6.2.2	Nova-induced cycle theory	133
A	WHT Nova shell images (in alphabetical order of constellation)	146
B	INT Nova shell images (in alphabetical order of constellation)	151

List of Figures

1.1	Artist’s impression of a Cataclysmic Variable	2
1.2	Figure 9 from Knigge et al. (2011)	9
1.3	Figure 18 from Knigge et al. (2011)	10
1.4	Figure 3 from Dubus et al. (2018)	11
1.5	Cartesian co-ordinate system in Roche geometry	14
1.6	Diagram showing the Roche potential.	15
1.7	The distribution of Galactic novae.	22
1.8	Optical lightcurve from Bode & Evans (2008)	24
1.9	Multi-frequency temporal development of a typical nova outburst.	25
1.10	Nova shell images from Bode & Evans (2008).	28
1.11	Maps of O[III] emission of HR Del.	29
1.12	Nova-induced cycle from Pagnotta (2015).	32
1.13	DD merger simulation from Sato et al. (2015).	35
2.1	CI Aql Light-curves	45
2.2	CI Aql Average blue and red spectra	46
2.3	CI Aql trailed spectra of Mg Ib, Ca I and Fe I from the secondary.	48
2.4	CI Aql trailed spectra of C III/N III $\lambda 4645\text{\AA}$, He II $\lambda 4686\text{\AA}$, H β and H α	49
2.5	CI Aql Doppler map of H α and He II $\lambda 4686\text{\AA}$	50
2.6	CI Aql Radial-velocity curve of He II $\lambda 4686\text{\AA}$	51
2.7	CI Aql Diagnostic diagram	52
2.8	CI Aql Light centre diagram for He II $\lambda 4686\text{\AA}$	53
2.9	CI Aql Radial-velocity curve of the secondary star	55
2.10	CI Aql Skew map and trailed CCFs	57
2.11	CI Aql optimal subtraction plots	58
2.12	CI Aql Orbitally-corrected spectra	59
2.13	CI Aql fractional contribution of the secondary star	59
2.14	CI Aql Monte Carlo system parameter determination	64
2.15	Plot of logP-M ₂ plane of SNIa progenitors	68
2.16	Possible fate of CI Aql	69

3.1	Simulated WFC nova shell images	74
3.2	WHT image and PSFs of V Per	84
3.3	BT Mon nova shell - enlarged	85
3.4	IPHAS $H\alpha$ and $H\alpha - r'$ images	88
3.5	V2275 Cyg IPHAS images	90
3.6	V2275 Cyg IPHAS image	92
4.1	INT WFC photograph and chip layout	98
4.2	PSF test of INT images	102
4.3	Simulated INT nova shell images	105
4.4	Simulation of 200 yr nova shell with radial profile	106
5.1	Image of the nova shell surrounding V1315 Aql	111
5.2	V1315 Aql DEIMOS slit positions	113
5.3	Image of the shell with overlaid circles centred on V1315 Aql	117
5.4	Keck DEIMOS spectrum of V1315 Aql.	118
5.5	Spectra of the seven shell slits of V1315 Aql	119
5.6	Spectra of the five shell slits from 6710–6740Å, showing the S[II] emission lines at 6716 and 6731Å.	120
5.7	$H\alpha$ spectrum of the sky from the South-East side of the V1315 Aql slit.	121
A.1	WHT images in order of constellation	147
A.2	WHT images	148
A.3	WHT images	149
A.4	WHT images	150
B.1	INT images in order of constellation	152
B.2	INT images	153
B.3	INT images	154
B.4	INT images	155
B.5	INT images	156
B.6	INT images	157
B.7	INT images	158

List of Tables

1.1	Classification of nova light curves per Payne-Gaposchkin (1957)	24
2.1	Journal of WHT observations for CI Aql	42
2.2	Fluxes and equivalent widths of prominent lines in CI Aql	47
2.3	System parameters for CI Aql	65
3.1	Journal of WHT observations	77
3.2	Journal of WHT observations	78
3.4	List of CVs examined in the IPHAS database	80
3.5	List of CVs examined in the IPHAS database	81
3.6	Summary of our first search for nova shells	93
4.1	Journal of INT observations	98
4.2	Summary of nova searches	103
5.1	Keck DEIMOS slit positions	112
5.2	Magnitudes of the four flux-calibration stars	115
5.3	Radial Velocities and FWHM of V1315 Aql shell spectra	121
5.4	H α and N[II] flux from V1315Aql shell slits	123

Acronyms/Abbreviations

AAVSO	American Association of Variable Star Observers
AML	Angular Momentum Loss
CAML	Consequential Angular Momentum Loss
CCD	Charge-Coupled Device
CM	Centre of Mass
CV	Cataclysmic Variable
DD	Double Degenerate
DEIMOS	DEep Imaging Multi-Object Spectrograph
DN	Dwarf Nova
DRP	Data Reduction Pipeline
FWHM	Full Width Half Maximum
GR	General Relativity
INT	Isaac Newton Telescope
IPHAS	INT Photometric H α Survey
ISIS	Intermediate dispersion Spectrograph and Imaging System
ISM	Interstellar Medium
N	Nova
NL	Novalike
PSF	Point Spread Function
pt5m	Point 5 metre telescope
RN	Recurrent Nova
SNIa	Type Ia Supernovae
SD	Single Degenerate
SED	Spectral Energy Distribution
VOSA	Virtual Observatory SED Analyser
WD	White Dwarf
WFC	Wide Field Camera
WHT	William Herschel Telescope

Chapter 1

Introduction

1.1 Cataclysmic variables - Overview

Around 50% of stars are formed and spend their lives in a binary system (King et al., 2012), so the study of the evolution of binary star systems is key to our understanding of the Universe. Where the binaries are widely separated, the individual stars essentially evolve as single stars, but if they are sufficiently close (within a few solar radii) then they can interact, and material can be accreted from one to the other (see Section 1.4). This gives rise to some of the most violent phenomena in the Universe including X-ray binaries containing either a black hole or neutron star, binary millisecond pulsars, novae and Type Ia supernovae (see Patat & Hallakoun 2018 for a review). The Type Ia supernovae act as standardisable candles, and have revealed the accelerating expansion of the Universe, driven by dark energy (Riess et al. 1998, Perlmutter et al. 1999). In some binaries, it is expected that the two stars will ultimately merge, giving rise to gravitational waves that can be detected using the next generation of gravitational wave detectors e.g. the Laser Interferometer Space Antenna (Amaro-Seoane et al., 2017).

In this thesis, I will describe my research into a type of binary system known as a cataclysmic variable (CV). They are comprised of a white dwarf (WD) accreting material from a secondary companion, usually a main sequence or evolved star. The

secondary star fills its Roche lobe (see Section 1.5.1) and material passes through the inner Lagrangian point, L1, forming a gas stream which is accreted onto the WD. In systems where the magnetic field of the WD is relatively weak ($B \lesssim 10^6$ G), the material is accreted via an accretion disc.

The accretion of the material onto the surface of the WD occurs via a zone known as the boundary layer. To be accreted onto the surface the gas must be decelerated from its Keplerian velocity to match the rotational velocity of the WD. The kinetic energy of the gas is converted into radiation by frictional forces, and can account for half of the total luminosity of the system (Warner, 1995).

Figure 1.1 shows an artist's impression of a CV. When sufficient material has accumulated on the surface of the white dwarf, it can undergo a thermonuclear runaway explosion, brightening the system by up to 11 mag.

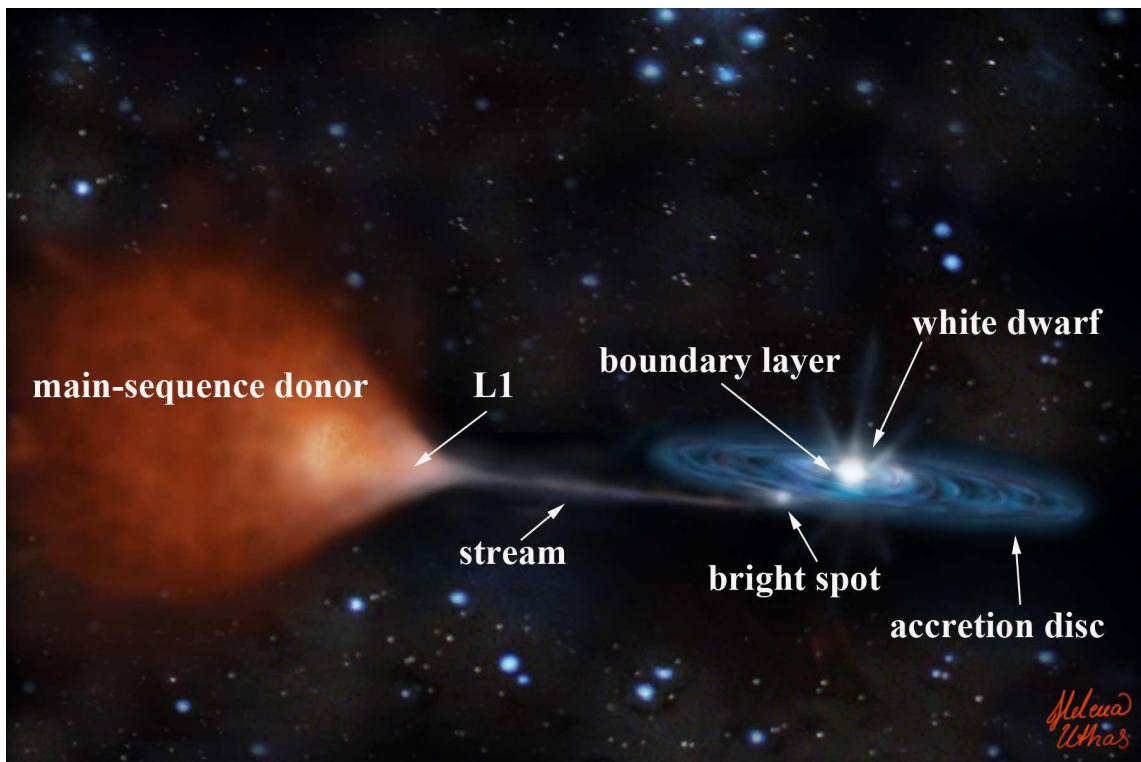


Figure 1.1: Artist's impression of a Cataclysmic Variable, comprising a White Dwarf and a main-sequence donor. The key features are the inner Lagrangian point, L1, gas stream, bright spot, boundary layer and the accretion disc. Credit: Uthas (2011)

1.2 CV classifications

CVs are classified according to the form of their long-term optical light-curves. Their luminosity varies on multiple timescales, from sub-second flickering to gradual changes over 10^4 years or longer. There are a number of categories of CV:

- Classical and recurrent novae (sometimes shortened to just novae).
- Dwarf novae.
- Novalike variables.
- Magnetic CVs
- Helium-rich systems

I will discuss each category in the following sections.

1.2.1 Classical and recurrent novae

Classical and recurrent novae show rapid brightenings of 7-11 magnitudes lasting for periods of a few years. The eruption of a classical nova (hereafter nova) is believed to be due to a thermonuclear runaway explosion of the hydrogen-rich material that has accreted onto the surface of the white dwarf. The material at the bottom of the accreted layer is subjected to huge pressure due to the strong gravitational field of the white dwarf. The temperature also increases as the accretion energy accumulates. Because the gas is degenerate, the pressure is not dependent on the temperature and does not expand. As the temperature and pressure reach the critical level for nuclear fusion of hydrogen, a thermonuclear runaway explosion occurs, ejecting most of the accreted material into space. This is called a nova eruption (see Bode & Evans 2008 for a review). Any system that has displayed a single nova eruption is classified as a *classical nova*. Systems that have shown multiple eruptions are known as *recurrent novae* (RNe).

The recurrent novae have inter-eruption timescales shorter than a human lifespan. The Galactic recurrent novae were classified by Anupama (2008) into three sub-types:-

- *RS Oph, T CrB group* comprising giant secondary stars and long orbital periods > 100 days. Their eruptions show evidence of interaction with pre-existing circumbinary material, probably blown off as wind from the red giant.
- *U Sco group*, also have evolved secondaries but have orbital periods of ~ 1 day. They have some of the fastest eruptions recorded, declining by two magnitudes from maximum in less than 10 days.
- *T Pyx group* has just T Pyx and IM Nor as members. They are short period systems ($P_{orb} < 3$ hrs) with low mass secondaries, but with significantly enhanced mass transfer rates, well above the secular mean for similar CVs (Knigge et al. 2000).

Recurrent novae have been discovered in other galaxies, notably Shafter et al. (2015) found 12 in M31 with a further 8 potential systems. These include the remarkable recurrent nova M31N 2008-12a which has had eleven eruptions, including eight in the past eight years (Darnley et al., 2016).

1.2.2 Dwarf novae

The dwarf novae (DNe) exhibit outbursts of between 2-6 magnitudes on timescales of weeks to years. The outbursts are believed to be due to an instability in the accretion disc which causes a sudden deposition of material onto the surface of the white dwarf. This *disc instability model*, first proposed by Osaki (1974), proposes that the instability is due to variations in opacity, and hence viscosity, of the disc material around the photo-ionisation point of hydrogen. Initially, the gas flowing from the secondary forms a thin accretion disc around the WD. As more gas is accreted, viscous drag will cause frictional heating of the material until it reaches the hydrogen photo-ionisation point. At this stage the opacity and viscosity rise rapidly, causing a sudden surge in the

amount of gas deposited from the disc onto the surface of the WD. This is observed as a DN outburst. After the disc has been emptied of most of the ionised gas, the system returns to its original accretion rate and the cycle repeats (Dubus et al., 2018). DNe also show other flux variability attributed to tidal distortions and precession of the disc, called superoutbursts and superhumps.

1.2.3 Novalike variables

The novalike variables (NLs) are CVs that have not exhibited any eruptions nor outbursts. They are spectroscopically similar to old novae. The observed mass transfer rates in NLs are much higher ($10^{-8} - 10^{-9} M_{\odot} \text{yr}^{-1}$) than the rates in DNe ($10^{-10} - 10^{-11} M_{\odot} \text{yr}^{-1}$). The higher mass transfer rate in NLs causes the gas in the disc to remain fully ionised, which suppresses the disc instability mechanism that causes DNe outbursts. The higher mass transfer rate in the NLs releases greater amounts of energy when accreted onto the WD and hence NLs are intrinsically brighter than DNe discs in quiescence.

1.2.4 Magnetic CVs

If a CV contains a white dwarf with a significant magnetic field (10-100 MG) it is classed as a polar or AM Her star. The magnetic field is so strong that the accretion stream is unable to form a disc, and the material is accreted directly onto the magnetic poles of the white dwarf. In other systems, the magnetic field of the white dwarf is weaker (1-10MG), and these are known as intermediate polars or DQ Her stars. The accretion stream is able to form an outer disc but as the material reaches the Alfvén radius, it is redirected to the magnetic poles. I do not consider magnetic systems in this thesis.

1.2.5 Helium-rich systems

There exists a small number of CVs in which the secondary star is mainly composed of helium (Solheim, 2010). These are known as AM CVn systems. They may have evolved through one or two common envelope events. As a result of their different composition and high density, they have very short orbital periods (< 65 min). Some may be in the final stages of their evolution. I do not consider helium-rich systems in this thesis.

1.3 White dwarfs in CVs

Stars are formed from collapsing clouds of gas and dust. As the temperature and pressure at the centre of the protostar rises, they begin nuclear fusion of hydrogen and join the *main sequence*. The subsequent evolutionary fate of the star is determined largely by its initial mass. Stars with masses in the range $0.08 - 10 M_{\odot}$ end their lives as white dwarfs (Ryan & Norton, 2010). When the nuclear burning of hydrogen has finished, the lowest mass stars, $0.08 - 0.5 M_{\odot}$, are unable to fuse helium in their cores because the temperature is too low. They eject their outer layers as a *planetary nebula* and the cores shrink to become helium (He) WDs. Stars with masses $0.5 - 8 M_{\odot}$ can ignite helium, but when the helium is exhausted they are not massive enough to initiate any further nuclear processing, and they become carbon/oxygen (CO) WDs. Finally stars with masses $8 - 10 M_{\odot}$ can burn carbon and oxygen. When this fuel is used up, nuclear fusion ceases and they become WDs composed of oxygen, neon, and magnesium (ONeMg). The stellar mass distribution shows that most stars have masses $< 8 M_{\odot}$ (e.g. Baldry & Glazebrook 2003) and so evolve to become CO WDs. The majority of white dwarfs in CVs are CO WDs (Smith & Dhillon 1998, Knigge 2006).

1.3.1 Electron degeneracy

In the collapsing core of a star that has ceased nuclear burning, the nuclei are compressed so much that the available quantum states for electrons are reduced to the point where the Pauli exclusion principle prevents them occupying the same quantum state. To compress the material further by the addition of electrons requires the creation of higher energy quantum states. This requirement for additional energy manifests itself as a pressure, called electron degeneracy pressure. The degeneracy pressure can withstand further gravitational compression for WDs up to the Chandrasekhar limit of $\sim 1.4 M_{\odot}$.

The equations of state for degenerate matter at the temperatures and pressures found in white dwarfs tell us that the radius of a white dwarf *decreases* as the mass increases. This is contrary to normal stars where the more massive they are, the bigger they are. The surface of a white dwarf usually contains either hydrogen or helium and this outer envelope acts as a thermal barrier, significantly reducing the rate of heat loss. As a result, WD cooling periods last for gigayears.

1.4 CV evolution

1.4.1 Pre-CV evolution

The widely accepted scenario (e.g. Warner 1995) for the formation of a CV starts with a wide (~ 100 AU) binary star system with both stars on the main sequence. The more massive star (the primary) evolves first to become a red giant. During this phase it expands dramatically and engulfs the secondary. This is called the *common envelope phase* (Paczynski, 1976). The envelope exerts significant drag on the stars, reducing the orbital separation to a few R_{\odot} and reducing the period from years to days. The envelope is eventually ejected by centrifugal forces and carries away additional angular momentum from the system, shrinking the orbital separation and the orbital period even further (a few solar radii). The red giant core remains as a WD and the system

is now a *detached binary system*. In order to become a CV, the secondary must fill its Roche lobe and begin mass-transfer. This may occur due to the normal evolutionary expansion of the secondary, or from shrinkage of the orbital separation due to angular momentum losses. I discuss the various types of angular momentum loss mechanisms in Section 1.5.

1.4.2 The canonical theory

The canonical evolutionary theory (e.g. Knigge et al. 2011) states that CVs evolve to shorter orbital periods as they lose angular momentum due to magnetic braking and gravitational wave radiation (see Sections 1.5.4 and 1.5.5 for a detailed explanation). When the mass of the secondary reaches $\sim 0.35 M_{\odot}$, the star becomes fully convective and its magnetic field structure changes significantly, with far fewer open field lines. Consequently angular momentum loss due to magnetic braking also reduces (Reiners & Basri, 2008). The secondary, which had been over-sized due to the high mass transfer rate, now relaxes within its Roche lobe and mass transfer ceases. Gravitational wave radiation continues to reduce the orbital period and the Roche lobe of the secondary eventually shrinks back onto the surface of the secondary and mass transfer is re-established. This transitional phase is called the *period gap*. Mass transfer then continues until the mass of the secondary is reduced to $\sim 0.08 M_{\odot}$ when core hydrogen burning ceases and the star becomes degenerate. At this point, the response of the secondary to the mass transfer changes. Up until this point, the secondary shrinks in response to mass loss. Once it is degenerate, mass loss causes it to expand.

In the types of CVs studied here, the secondary is lighter than the WD primary, hence the orbital separation is increased due to mass transfer from the secondary to the primary, since mass is moving towards the common centre of gravity. The expansion of the secondary due to mass transfer means it can fill its Roche lobe at the wider separation and the system evolves to longer orbital periods. Systems that have passed through this *period minimum* are called *period bouncers*. They are extremely faint due

to the very low mass transfer rate ($\sim 10^{-11} M_{\odot} \text{ yr}^{-1}$). A number of such systems have been identified (Littlefair et al. 2006, 2008). Figure 1.2, taken from Knigge et al. (2011), shows the mass–period relation of secondary stars in CVs. The systems evolve from top right to the lower left, as the secondary loses mass. The lines show the standard and a revised best fit model, using a broken power law model. The vertical black line is the observed location of the period minimum, $P_{\min} = 83 \pm 3$ min, from Gänsicke et al. (2009).

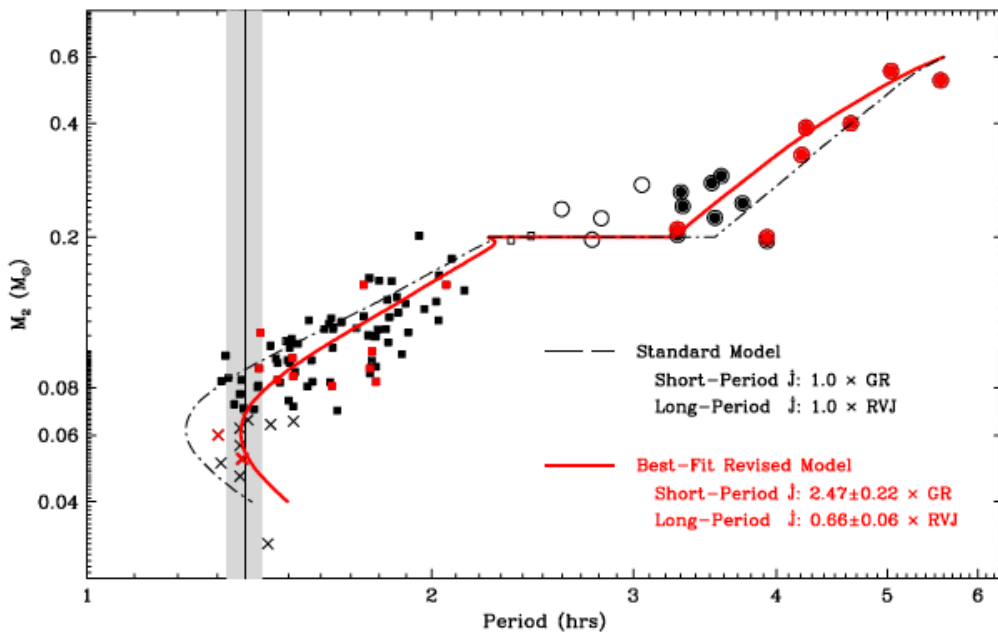


Figure 1.2: Self-consistent model fits to the observed properties of CV donors in the period-mass plane. The different symbols represent various types of CV. Superhumpers are shown in black, eclipsers in red. Filled squares correspond to short-period CVs, filled circles to long-period systems, and crosses to candidate period bouncers. The black dash-dotted line shows the predicted evolution of donor properties according to the standard model for CV evolution, which is characterised by $f_{GR} = f_{MB} = 1$. The red solid line shows the evolution of donor properties along the best-fit model track. This revised model is characterised by $f_{GR} = 2.47 \pm 0.22$ (i.e. enhanced AML) below the gap and $f_{MB} = 0.66 \pm 0.05$ (i.e. slightly reduced AML) above. The vertical line in the top panel marks the observed location of the period spike, corresponding to P_{\min} . Reproduced from Figure 9 from Knigge et al. (2011).

The canonical CV evolution scheme implies that systems with high mass transfer rates, the novalikes, would be predominantly found with periods > 3 hours i.e. above the period gap, where both magnetic braking and gravitational braking occur. At periods < 2 hours, below the period gap, we would expect to find only dwarf novae with their

the lower transfer rates, because only gravitational braking occurs (see Sections 1.5.4 and 1.5.5). In the next section we will compare the observed orbital period distribution with the theoretical distribution of CVs with orbital periods below 6 hr.

1.4.3 Orbital period distribution

Figure 1.3 is taken from Knigge et al. (2011) and shows the orbital period distribution of all non-magnetic CVs in the catalogue of Ritter & Kolb 2003¹ (hereafter RK catalogue). The DNe are shown in red.

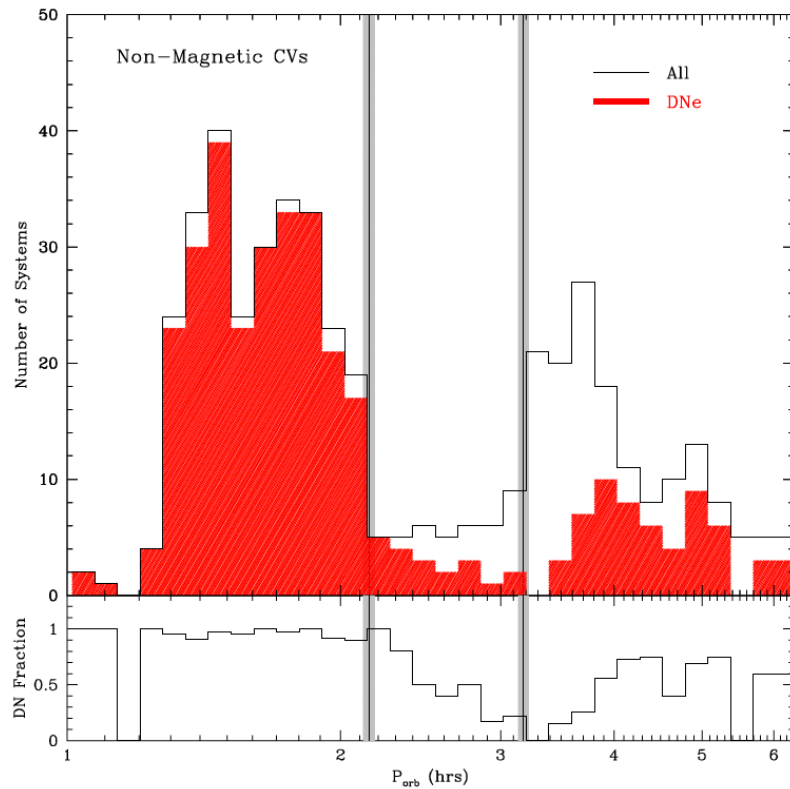


Figure 1.3: Top panel: the solid black histogram shows the orbital period distribution of all non-magnetic CVs (i.e. novalikes and dwarf novae) in the RK catalogue (v7.11) with orbital periods below 6 hr. The red shaded histogram shows the subset of DNe within this sample. Bottom panel: the DN fraction - defined as the ratio of DNe to all non-magnetic CVs within a given period bin - is shown as a function of orbital period. In both panels, the vertical lines and grey shaded regions mark the location of the upper and lower period gap edges, along with their errors. Figure 18 from Knigge et al. (2011)

Contrary to the theoretical prediction, we see that some novalikes are found below

¹<http://www.mpa-garching.mpg.de/RKcat/>

the period gap and a considerable number of DNe are found above the period gap. A recent paper by Dubus et al. (2018) using the European Space Agency (ESA) mission *Gaia* Data Release 2² (Gaia DR2) distances found that the mass transfer rates of known novalikes and dwarf novae show the expected distribution around the unstable region of the orbital period – mass transfer rate plane as predicted by the disc instability model as shown in Figure 1.4. This Figure also shows that novalikes and dwarf novae coexist at the same orbital period with two orders of magnitude differences in their mass transfer rates.

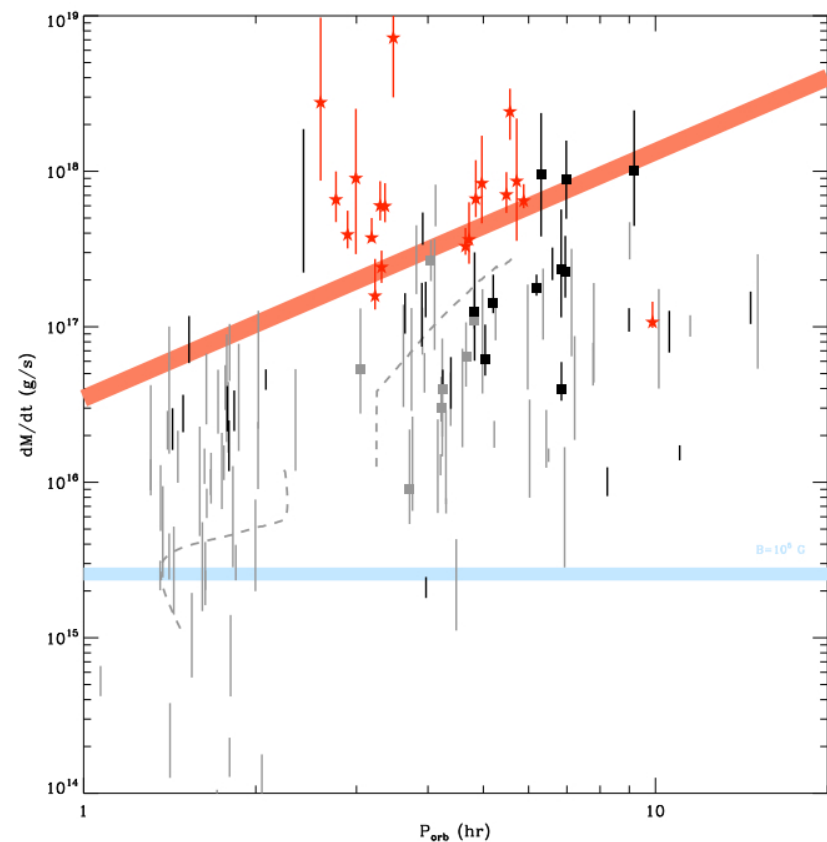


Figure 1.4: Mass transfer rates of cataclysmic variables compared to the stability criterion. Systems above the (red) upper solid line are hot and stable. Systems below the lower (blue) line will be cold, stable discs if the white dwarf magnetic field $B \geq 10^5 \text{G}$. The dashed line is the expected secular mass transfer rate (Knigge et al., 2011). Square symbols indicate Z Cam type dwarf novae, (red) stars indicate nova-likes. The filling fraction, f , of each lightcurve is defined as the fraction of its bins that contain a measurement. Dwarf novae with $f \geq 0.5$ are shown in black and those with $f < 0.5$ are in grey. Figure 3 from Dubus et al. (2018)

²<https://www.cosmos.esa.int/gaia>

How can this be explained? It is possible that CVs cycle between NL and DN states on timescales shorter than the gigayear evolutionary timescale of the binary, thereby explaining the coexistence of NLs and DNe at the same orbital period. Two mechanisms for such a cycle have been proposed. Both mechanisms invoke cyclical variation in the irradiation of the secondary, which in turn drives cyclical variation of \dot{M} with time-scales of the order of $\sim 10^4 - 10^7$ yr.

The first idea is that there is an irradiation feedback mechanism (see Büning & Ritter 2004 and references therein). The flux from the WD illuminates the inner face of the secondary which flattens the temperature gradient in the photosphere, leading to an expansion in the radius of the secondary and an increase in the mass transfer rate, \dot{M} , above the secular mean. The enhanced \dot{M} drives an increase in the radius of the secondary's Roche lobe. Eventually the expansion of the secondary star cannot keep pace with the Roche lobe expansion, leading to a lower \dot{M} and hence a reduction in the irradiating flux. Consequently, the secondary begins to shrink and the feedback mechanism operates in reverse as the mass-transfer rate reduces. Büning & Ritter (2004) found that this mechanism could produce limit cycles in \dot{M} of the appropriate time-scales (see Figure 5 of Knigge et al. 2011), causing CVs to cycle between DN and NL states. However, their models show that systems just above the period gap are actually stable and do not undergo cycles. Hence, although this model explains why some NLs and DNe may coexist at the same orbital period, it does not explain why the irradiation-driven feedback mechanism would make the NL fraction highest around 3 h and decline towards longer periods.

The second hypothesis is that a nova eruption may cause systems to cycle between novae, novalike and dwarf nova states. I discuss this “nova-induced cycle” theory in Section 1.7.

1.5 Angular momentum loss

The evolution of CVs is believed to be driven by angular momentum loss from the binary. This drives mass transfer from the secondary to the primary and gives rise to the eruptive events that we witness. I will discuss the main sources of angular momentum loss in the following sections, but first we need to understand the geometry of two stars orbiting each other in close proximity.

1.5.1 Roche lobe geometry

Newton's derivation of Kepler's third law gives the relationship between the orbital separation, a , the orbital period, P_{orb} , and the masses of the primary and secondary, M_1, M_2 :

$$a^3 = \frac{G(M_1 + M_2)P_{orb}^2}{4\pi^2}, \quad (1.1)$$

where G is Newton's gravitational constant. The masses and orbital periods of CVs result in orbital separations of the order of a few solar radii. At these separations, the gravitational fields of the two stars interact, and the shape of the secondary star can become distorted. The white dwarf's diameter is of the order of one Earth diameter so its shape is largely unaffected by the tidal force.

To understand the interaction of the gravitational fields of the stars, we use the Roche model, named after the French mathematician Edouard Roche, who formalised the mathematics of two-body gravitational fields. The formalisation by Kopal (1959) uses a co-rotating Cartesian co-ordinate system (x, y, z) with the centre of the WD as the origin, and the secondary located at $(a, 0, 0)$, as shown in Figure 1.5.

The gravitational potential, Φ , at position (x, y, z) is given by

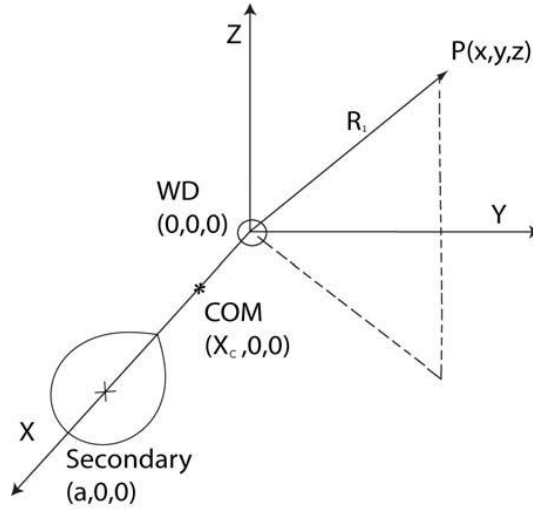


Figure 1.5: The Cartesian co-ordinate system in Roche geometry. The origin is located at the centre of the WD, and the secondary is located at $(a, 0, 0)$. The frame co-rotates with the binary system.

$$\Phi = -\frac{GM_1}{(x^2 + y^2 + z^2)^{1/2}} - \frac{GM_2}{((x - a)^2 + y^2 + z^2)^{1/2}} - \frac{2\pi^2}{P_{orb}^2} \left[\left(x - \frac{aM_2}{M_1 + M_2} \right)^2 + y^2 \right]. \quad (1.2)$$

where the first term is the gravitational potential from the primary, the second term is the potential from the secondary, and the third term represents the potential from the centrifugal force. From Equation 1.2 we can derive surfaces of equipotential as shown in Figure 1.6. There are five points where the rate of change of the equipotential is zero, and they are called the Lagrangian points, numbered L1-L5 in Figure 1.6.

The figure-of-eight contour represents the critical potential of the two volumes called Roche-lobes. These represent the maximum size a star can attain within the binary system. In CVs, the high density of the WD means it never fills its Roche lobe whereas the secondary stars are at or near their Roche lobe. The inner Lagrangian point, L1, is the point through which material will pass from the Roche-lobe filling secondary to the primary and begin a free-fall trajectory onto the white dwarf.

The shape of the Roche-lobe filling secondary star is deformed to match that of the equipotential, the so-called ‘teardrop’ shape. We use the equation derived by Eggleton (1983) to approximate the radius of a spherical star, R_2 , with the same volume as the

Roche Equipotentials

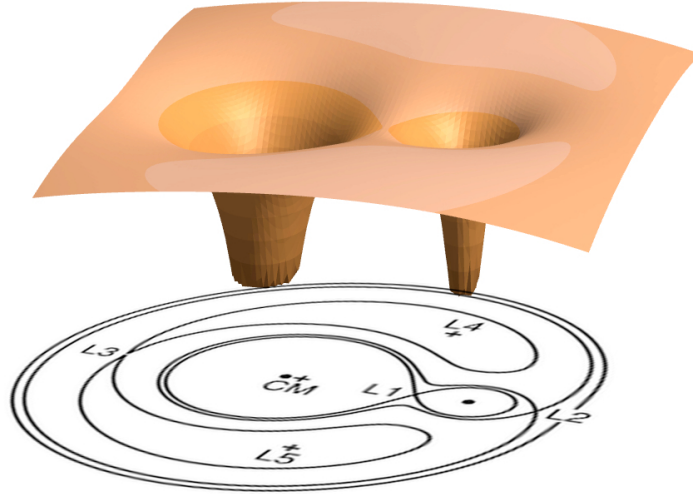


Figure 1.6: Diagram showing the Roche potential. The upper portion of the diagram shows a 3D representation of the Roche potential surface in the orbital plane of a CV. The more massive WD is located to the left and has the larger gravitational potential compared to the secondary to the right. The contour plot below shows a number of equipotential contours, and the five Lagrangian points are marked L1-L5. The centre of mass is marked with a cross labelled ‘CM’

Roche lobe, R_L .

$$\frac{R_2}{a} \approx \frac{R_L}{a} = \frac{0.49q^{2/3}}{0.6q^{2/3} + \ln(1 + q^{1/2})}, \quad (1.3)$$

where q is the mass ratio M_2/M_1 . Equation 1.3 is accurate to about $\pm 1\%$ for all values of q .

1.5.2 Angular momentum

The angular momentum of a binary star system (J) can be expressed as

$$J = M_1 a_1 \frac{2\pi a_1}{P_{orb}} + M_2 a_2 \frac{2\pi a_2}{P_{orb}} = M_1 M_2 \left(\frac{Ga}{M} \right)^{1/2}, \quad (1.4)$$

where M is the combined mass of the system, i.e. $M = M_1 + M_2$ and a_1 and a_2 are the distances of the two stars from the centre of mass ($a = a_1 + a_2$). We can differentiate

this equation logarithmically to give

$$\frac{\dot{J}}{J} = \frac{\dot{M}_1}{M_1} + \frac{\dot{M}_2}{M_2} + \frac{1}{2} \frac{\dot{a}}{a} - \frac{1}{2} \frac{\dot{M}}{M}. \quad (1.5)$$

If there is no net mass loss from the system it is said to be conservative such that $\dot{M}_1 = -\dot{M}_2$ and $\dot{M} = 0$. Substituting these values into Equation 1.5 and rearranging gives:

$$\frac{\dot{a}}{a} = 2 \frac{\dot{J}}{J} - 2(1-q) \frac{\dot{M}_2}{M_2}. \quad (1.6)$$

Equation 1.6 shows that when angular momentum is conserved ($\dot{J} = 0$), mass transfer from the secondary to the primary will cause a to increase, where $M_2 < M_1$.

We can evaluate the effect of mass transfer on the Roche lobe radius by using the modified form of the Paczyński (1971) equation derived by Smith & Dhillon (1998):

$$R_L = 0.47a \left(\frac{M_2}{M} \right)^{1/3}. \quad (1.7)$$

Equation 1.7 can be logarithmically differentiated as follows:

$$\frac{\dot{R}_L}{R_L} = \frac{\dot{a}}{a} + \frac{1}{3} \frac{\dot{M}_2}{M_2} - \frac{1}{3} \frac{\dot{M}}{M}. \quad (1.8)$$

Substituting \dot{a}/a from Equation 1.6 and assuming $\dot{M} = 0$ gives:

$$\frac{\dot{R}_L}{R_L} = 2 \frac{\dot{J}}{J} - \frac{\dot{M}_2}{M_2} \left(\frac{5}{3} - 2q \right), \quad (1.9)$$

Equation 1.9 shows that the response of the Roche lobe is dependent on the mass ratio q . Assuming the conservative case of $\dot{J} = 0$ then the Roche lobe radius will increase in response to mass transfer if $q < 5/6$.

So, we have the mathematical tools to understand how CVs respond to mass transfer.

1.5.3 Response to mass transfer

The evolution of a CV depends on the response of the secondary's radius and its Roche lobe radius as mass is transferred to the primary. We use an expression of the form $R \propto M^\xi$ to describe the mass-radius relationship. Hence the exponent ξ of the secondary is:

$$\xi = \frac{d \ln R_2}{d \ln M_2}. \quad (1.10)$$

Similarly the response of the Roche lobe ξ_L is given by:

$$\xi_L = \frac{d \ln R_L}{d \ln M_2}. \quad (1.11)$$

Combining this with Equation 1.9, and assuming conservative mass transfer and conservation of angular momentum (i.e. $\dot{M} = 0$, $\dot{M}_1 = -\dot{M}_2$, $\dot{J} = 0$) gives:

$$\xi_L = 2q - \frac{5}{3}. \quad (1.12)$$

If the response of the secondary fails to keep it within its Roche lobe, then mass transfer will be unstable, possibly leading to another common envelope phase (see Section 1.4.1). In order for mass transfer to be stable, the response of the secondary must exceed the response of its Roche lobe i.e. $\xi > \xi_L$. Combining this inequality with Equation 1.12 gives:

$$q < \frac{\xi}{2} + \frac{5}{6}. \quad (1.13)$$

The value of ξ depends on the timescale on which the secondary responds to mass loss,

$$\tau_{\text{ML}} = \frac{M_2}{\dot{M}_2}, \quad (1.14)$$

τ_{ML} is dependent on two other timescales. Firstly, the *dynamical timescale*,

$$\tau_{dyn} = [G, \bar{\rho}(R)]^{-\frac{1}{2}}, \quad (1.15)$$

where $\bar{\rho}$ is the mean density with a radius R . This is the timescale for the star to adiabatically return to hydrostatic equilibrium. Secondly, the *Kelvin-Helmholtz timescale* is the time for the secondary to reach a new thermal equilibrium, and is given by:

$$\tau_{KH} \sim \frac{GM_2^2}{R_2 L_2}, \quad (1.16)$$

where L_2 is the luminosity of the secondary. In general, $\tau_{KH} \gg \tau_{dyn}$, so stars reach hydrostatic equilibrium much faster than thermal equilibrium. So if the mass loss rate is much slower than the thermal timescale (i.e. $\tau_{ML} \gg \tau_{KH}$), then the secondary remains in thermal equilibrium and the mass-radius exponent, ξ , is that of a normal main sequence star, $\xi_{KH} \sim 0.8$ (Knigge et al., 2011). Substituting this into Equation 1.13, gives a mass ratio of $q < 1.23$ for stable mass transfer.

If mass loss is rapid, with $\tau_{ML} \ll \tau_{KH}$, then mass transfer occurs on a dynamical timescale. Politano (1996) calculated the range of ξ_{dyn} for stars up to $0.8 M_\odot$, giving the maximum value of q as follows:

$$q = \begin{cases} \frac{2}{3}, & M_2 \leq 0.4342 M_\odot \\ 2.244(M_2 - 0.4343)^{1.364} + \frac{2}{3}, & 0.4342 \leq M_2 < 0.8 M_\odot \end{cases} \quad (1.17)$$

In CVs with $M_2 > 0.8 M_\odot$ mass transfer is stable if $q < 1.23$.

In practice we find that most CVs have $q < \frac{5}{6}$ (Patterson et al., 2005) in which case the Roche lobe expands with mass loss (see Equation 1.9), but the secondary will shrink. So mass loss will not proceed unless angular momentum is being lost from the system.

I shall now go on to discuss in detail the two main processes of angular momentum loss, magnetic braking and gravitational wave radiation, and briefly explain a third

mechanism, consequential angular momentum loss.

1.5.4 Disrupted magnetic braking

The concept of a magnetic braking mechanism in binary star systems was first proposed by Verbunt & Zwaan (1981). The secondary stars in CVs with masses $>0.35 M_{\odot}$ have significant magnetic fields. They eject an ionised wind which is coupled to the open magnetic field lines as it moves away from the star. This exerts a magnetic braking torque on the star, removing angular momentum and hence reducing its rotational speed. However, the secondary is tidally locked to the primary so the angular momentum is removed from the combined system, thereby reducing the orbital period. Angular momentum is lost from the system, keeping the secondary in contact with its Roche lobe and thus driving mass transfer.

The orbital period distribution (see Figure 1.3) shows a dearth of systems in the orbital period range 2 – 3 hr, known as the period gap. Rappaport et al. (1983) suggested that as the secondary star loses mass, its core will become fully convective when it reaches $M_2 \sim 0.35 M_{\odot}$ (spectral type M3 – M4). The star's magnetic field topology would change, with far fewer open field lines, and the strength of the field would reduce significantly. The angular momentum loss due to magnetic braking would consequently reduce. The secondary, which has been out of thermal equilibrium up to this point due to the high mass loss rate, would relax back inside its Roche lobe, causing mass transfer to cease. Angular momentum losses would now be driven mainly by gravitational wave radiation (see following section). The orbital period of the CV would reduce further until the secondary re-established contact with its Roche lobe and mass transfer recommenced. Hence the period gap is explained because the systems in this range have their magnetic braking disrupted, so mass transfer ceases and therefore their luminosity is significantly reduced.

The disrupted magnetic braking (DMB) theory also successfully explains the higher accretion rates above the period gap and the bloating of the secondary stars, as well

as explaining the gap itself (Knigge et al., 2011). However, more direct support comes from observations of the populations of post-common envelope binaries (PCEB), which are seen as detached WD–main sequence pairs. Measurements from PCEBs found in the SDSS survey by Zorotovic et al. (2016) found an excess of systems in the 2 – 3 hr period range, above the numbers expected from PCEB models, and they also found that the average WD mass of these detached CV systems was higher than the PCEBs. Zorotovic et al. (2016) conclude that this excess comprises CVs in the period gap.

1.5.5 Gravitational wave radiation

The second mechanism believed to be responsible for angular momentum loss in CVs is gravitational wave radiation, first proposed by Einstein. The theory of general relativity (GR) tells us that two stars in orbit around each other will lose angular momentum via gravitational wave radiation according to the formula

$$\frac{\dot{J}}{J} = \frac{-32}{5} \frac{G^3}{c^5} \frac{M_1 M_2 (M_1 + M_2)}{a^4}, \quad (1.18)$$

where c is the speed of light. At orbital periods below 2 hours, where magnetic braking has reduced significantly, gravitational wave radiation is the main driver of angular momentum loss.

1.5.6 Consequential angular momentum loss

The material that is transferred from the secondary accretes onto the surface of the white dwarf with the release of copious amounts of energy ($10^{30} - 10^{33}$ erg s^{-1}). This can drive ionised winds from the accretion region, which will be tied to the magnetic field of the WD, and consequently additional angular momentum is removed from the system (Livio & Pringle 1994). This is called consequential angular momentum loss (CAML). It should be stressed that CAML only operates in conjunction with the other angular momentum loss processes described in Sections 1.5.4 and 1.5.5 above. Recent

modelling by Schreiber et al. (2016) has shown that CAML can help explain a number of differences between the theoretical and observed properties of CV populations, specifically why the average WD mass in CVs is higher than average mass of single WDs, and the disparity between the predicted and observed orbital period distribution and space densities of CVs.

So we now have robust semi-empirical models to describe the evolution of CVs, driven by angular momentum losses. I will now focus on one class of CV, the *novae*, which form the central theme of my thesis.

1.6 Novae characteristics

The term nova derives from the Latin phrase *stella nova* (new star) first used by Tycho Brahe to describe a bright new star that appeared in 1592, which turned out to be what we now call a supernova. Previous sightings of new heavenly bodies have been recorded by Chinese, Korean and Japanese astronomers since the 6th century BCE. In the West, novae only really began to be observed in significant numbers after the development of the telescope in the mid-17th century, by early astronomers like Johannes Kepler. The advent of astronomical photography led to a further step change in the number of novae discovered each year (Payne-Gaposchkin, 1957). In modern times, wide field-of-view ground-based and satellite surveys reveal new novae on an almost weekly basis, in neighbouring galaxies as well as our own (Shafter, 2017).

1.6.1 Galactic and extra-galactic novae

Figure 1.7 shows the Galactic distribution of novae brighter than $m = 10$ discovered since 1900 from Shafter (2017), who estimates that the Galactic nova rate is 50 – 100 per year. The wide range is due to the uncertainty in the completeness of nova detection rates which they estimate at $\sim 90\%$, whereas Schaefer (2014) found a much lower rate of $\sim 43\%$. The Galactic novae are concentrated towards the Galactic plane and in the bulge, although a few novae have been seen in the halo, suggesting a Population

II origin. It has also been suggested by della Valle et al. (1992) that there are two distinct populations of novae, those in the Galactic plane are faster and brighter whilst the bulge population are slower and fainter.

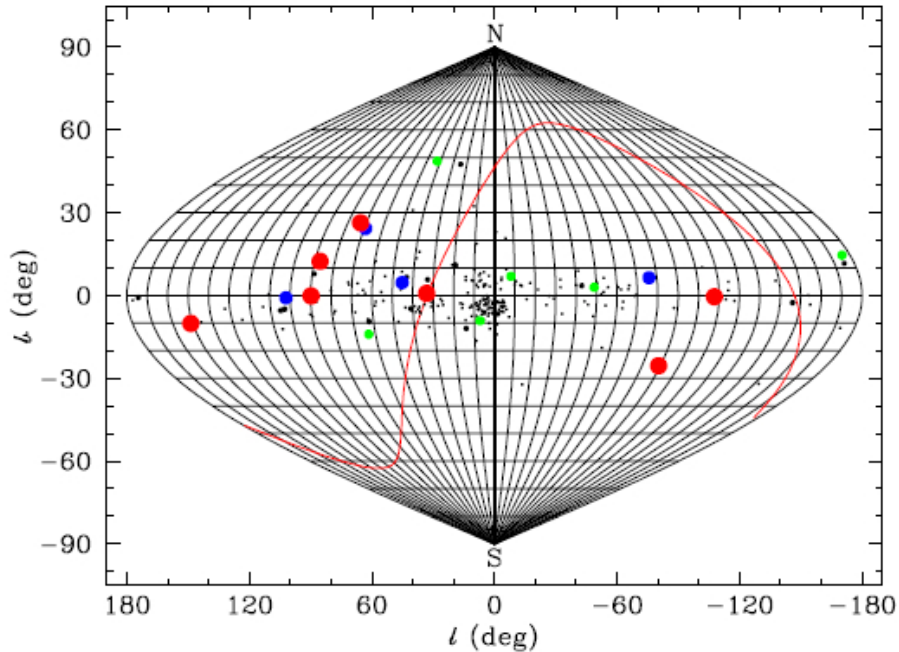


Figure 1.7: The distribution of Galactic novae brighter than $m = 10$ discovered since 1900 are displayed in Galactic coordinates (b is Galactic latitude and l is Galactic longitude). Key: red filled circles: $m \leq 2$, smaller blue filled circles: $2 \leq m \leq 3$, smaller green filled circles: $3 \leq m \leq 4$, smaller black filled circles: $4 \leq m \leq 5$, smallest black dots: $5 \leq m \leq 10$. The solid red line represents the Celestial equator. From Shafter (2017).

In external galaxies, novae are routinely detected by ongoing synoptic surveys, and over 1 000 have now been detected in M31 alone. The nova rate in M31 was estimated to be 65_{-15}^{+16} per year by Darnley et al. (2006). The rate in M87 was measured at 363_{-45}^{+33} per year by Shara et al. (2016), although this result was subsequently reviewed by Shafter et al. (2017) who found that this figure was probably an upper limit due to the uncertainties in identifying bona fide novae from incomplete light-curves, and in extrapolating observations near the centre of M87 to the entire galaxy. They also found that other galaxies that have significant numbers of recorded nova outbursts include M33, M32, NGC205, LMC, SMC & M81. The nova rates in these galaxies are broadly

comparable to our Galaxy, when adjusted for the different stellar populations (Shafter et al., 2017).

1.6.2 Light curve classification

An example of a typical optical light curve from a nova eruption is shown in Figure 1.8, taken from Bode & Evans (2008). The key features are:

- Initial rise/pre-maximum halt and final rise - the initial rise to maximum brightness is very rapid lasting only a few days and hence only a few novae have been observed during this phase. Some of those that have been observed show a pre-maximum halt, although the underlying cause of this is uncertain (Hillman et al., 2014). Novae brighten by up to 11 mags during this phase (Warner, 1995).
- Early decline - having reached a maximum, novae reduce in brightness quickly, reducing by 2 mags in 10–100 days.
- Transition phase - this is the phase where novae can exhibit a wide variety of behaviours, including rebrightenings, a dip/rebrightening, or oscillations.
- Final decline - as the nova eventually fades and disappears, it moves into the nebular phase, showing features associated with HII regions.

1.6.3 Light curve speed classes

The speed of decline of novae can vary significantly and it was Payne-Gaposchkin (1957) that first suggested a classification scheme based on the speed class. The speed of decline (t_n) is classified according to the number of days it takes to decline n magnitudes from its maximum. Table 1.1 shows the Payne-Gaposchkin (1957) classification scheme. It is now recognised that the speed of decline is a continuous variable dependent on the system parameters, but the speed class terminology persists in the literature.

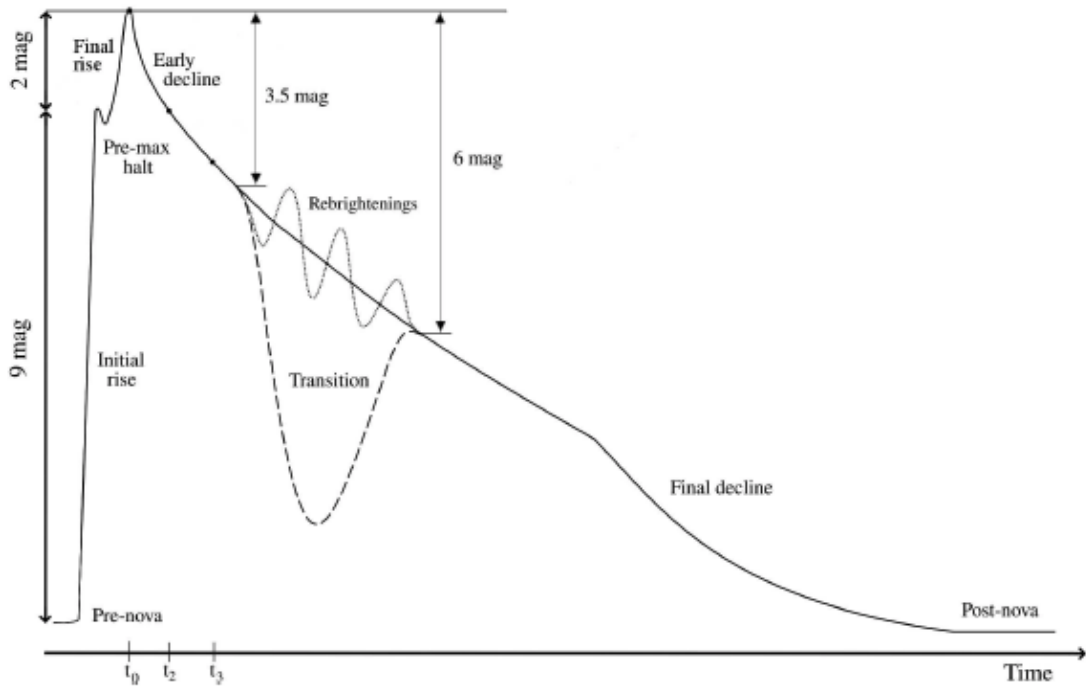


Figure 1.8: Optical light curve of a generic nova. Taken from Bode & Evans (2008).

Table 1.1: Classification of nova light curves per Payne-Gaposchkin (1957)

Speed class	t_2 (days)	\dot{m}_V (mag d ⁻¹)
Very fast	< 10	> 0.20
Fast	11 – 25	0.18 – 0.08
Moderately fast	26 – 80	0.07 – 0.025
Slow	81 – 150	0.024 – 0.013
Very slow	151 – 250	0.013 – 0.008

1.6.4 Spectral evolution

In many respects, the spectral evolution of a nova event follows the photometric development. The pre-maximum spectrum is dominated by broad blue-shifted absorption lines from the expanding photosphere, which strengthen as the nova reaches maximum light. This is the fireball stage and is powered by the shock passing through and ejecting the overlying layers of gas on the surface of the WD. Degeneracy is lifted from the WD atmosphere and it begins to expand. The gas is fully ionised and expands until recombination begins. The next phase sees the disappearance of UV emission, the so-called ‘iron-curtain’, where the expelled gas has recombined and is now optically

thick in the UV. The third phase sees a lifting of the iron-curtain as the gas becomes less dense as it expands. This exposes the outer layers of the expanding shell to harder radiation from the continuing hydrogen fusion on the WD surface and leads to further ionisation of the shell. The peak of the flux is now in the UV and FUV. As the shell continues to expand, the system moves into the transition phase. In many cases, this is the point where significant dust formation begins, leading to a dip in the UV and optical emission which is reprocessed into the IR. Radio emission grows significantly at this point from free-free emission in the gas cloud. As the shell expands further and the dust begins to cool the IR flux drops and the surface of the WD is revealed, where continuing hydrogen fusion on the surface gives rise to super-soft X-ray radiation which persists until the nuclear fusion ceases. The multi-frequency evolution of a typical nova light curve is shown in Figure 1.9.

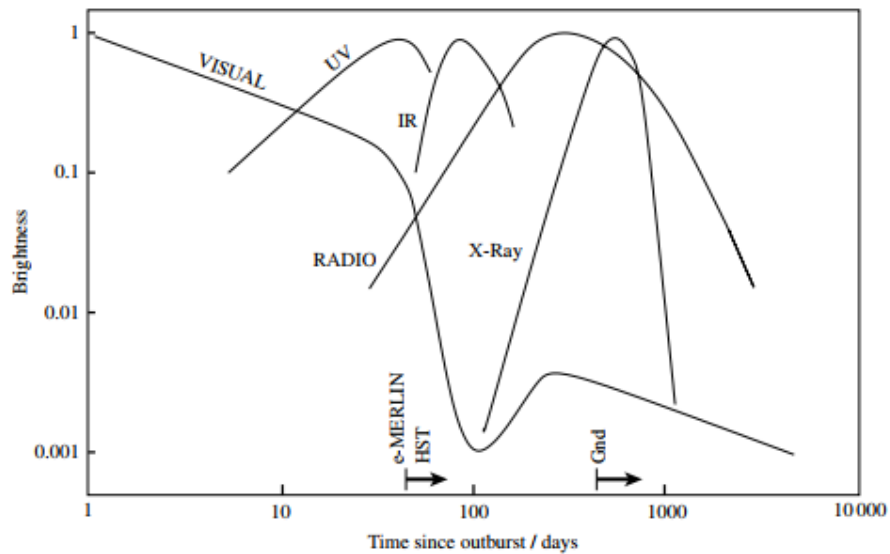


Figure 1.9: Schematic of the multi-frequency temporal development of a typical nova outburst. Taken from Bode & Evans (2008).

1.6.5 Nuclear fusion processes

The hydrogen-rich material that has accreted onto the surface of the WD is quickly redistributed across the whole WD surface. The pressure at the base of the layer is

enormous due to the WD mass and size, and the temperature continuously increases due to heat from the accreted material above and from the WD below. Eventually the temperature reaches $> 10^7\text{K}$ and hydrogen fusion via the p-p chain begins. In the degenerate layer, pressure does not increase with temperature so the thermonuclear reaction proceeds exponentially. Eventually the degeneracy is lifted and the gas can expand. This is what powers the expulsion of the outer layers. During this phase, some material, specifically C, N and O, are dredged up from the WD core, and the CNO chain of nuclear reactions begin, adding to the explosive power. Other studies suggest that the p-e-p chain is also a significant contributor to the energy generated (Starrfield et al. 2012).

1.6.6 Does the WD gain or lose mass during a nova eruption?

This is one of the key questions in nova research. If the WDs are gaining mass then they may be the progenitors of SNIa. Observations and models suggest that about 5% of the accreted mass is consumed by the nuclear fusion processes. All, or almost all, the remainder is blown off the WD and forms the nova remnant shell. The mass of the ejecta is of the order of $10^{-5} M_{\odot}$, and is ejected with velocities of $500 - 3000 \text{ km s}^{-1}$ (Warner, 1995).

In a detailed study of two recurrent novae, CI Aql and U Sco, Schaefer (2011) began a program to measure the orbital period change across their nova eruption, which gives an accurate measure of the mass ejected from the system. The initial results, after 24 years of monitoring, show that for U Sco the M_{ejecta} is very close to the mass accreted between successive nova eruptions, calculated using a mass transfer rate derived by Shen & Bildsten (2007). For CI Aql, the results show M_{ejecta} is less than the accreted mass so the WD may be growing in mass. It is hoped that the forthcoming eruptions of these two systems will refine these results.

A number of groups have developed models of the long term effects of accretion onto WDs of differing masses and composition. Nomoto & Leung (2018) provides a

comprehensive review of the conflicting findings of each group and sets out how different treatment of opacity, the number of mass shell grids, initial WD temperature, mass-loss algorithm, the assumed conditions for stable nuclear burning and mass retention efficiency can lead to different results. Further issues arise because most models are 1-dimensional and take no account of rotation nor the dredge up of core WD material due to shear mixing at the boundary layer.

1.6.7 Nova shells

A sizeable fraction of novae produce visible remnants. Out of the 93 novae listed by Strobe et al. (2010), some 29 are recorded as having shells, giving a rate of 31%. Warner (1995) provides a more comprehensive list of 45 remnants dating back to 1891. Bode & Evans (2008) presents images of 32 shells, shown in Figure 1.10. Some remnants may be too distant or too faint to observe but that does not account for the significant number that did not form a visible shell. Figure 1.10 shows that some of the nova shells are roughly circular in shape, many display bipolar shape, with polar blobs and equatorial rings.

A further example of bilobal structure in a shell is given in Figure 1.11 which shows velocity maps of the O[III] emission from the shell surrounding HR Del. There are clearly two polar structures and the shell has a very clumpy appearance. Earlier observations by Harman & O'Brien (2003) using the HST WFPC2 also showed these features.

Ribeiro et al. (2011, 2013, 2013, 2014) looked at KT Eri, RS Oph, V2491 Cyg and V959 Mon and found that the emission line profiles were best modelled by a bipolar structure. They also modelled radio light curves from a bipolar shell and compared it to spherical models. They found that in the worst cases the mass estimate was doubled by the assumption of sphericity, and the electron temperatures were halved. A panchromatic study of four bright novae (V1369 Cen, T Pyx, V339 Del and V959 Mon) by Mason et al. (2018) showed that all four are best modelled by bi-conical geometry

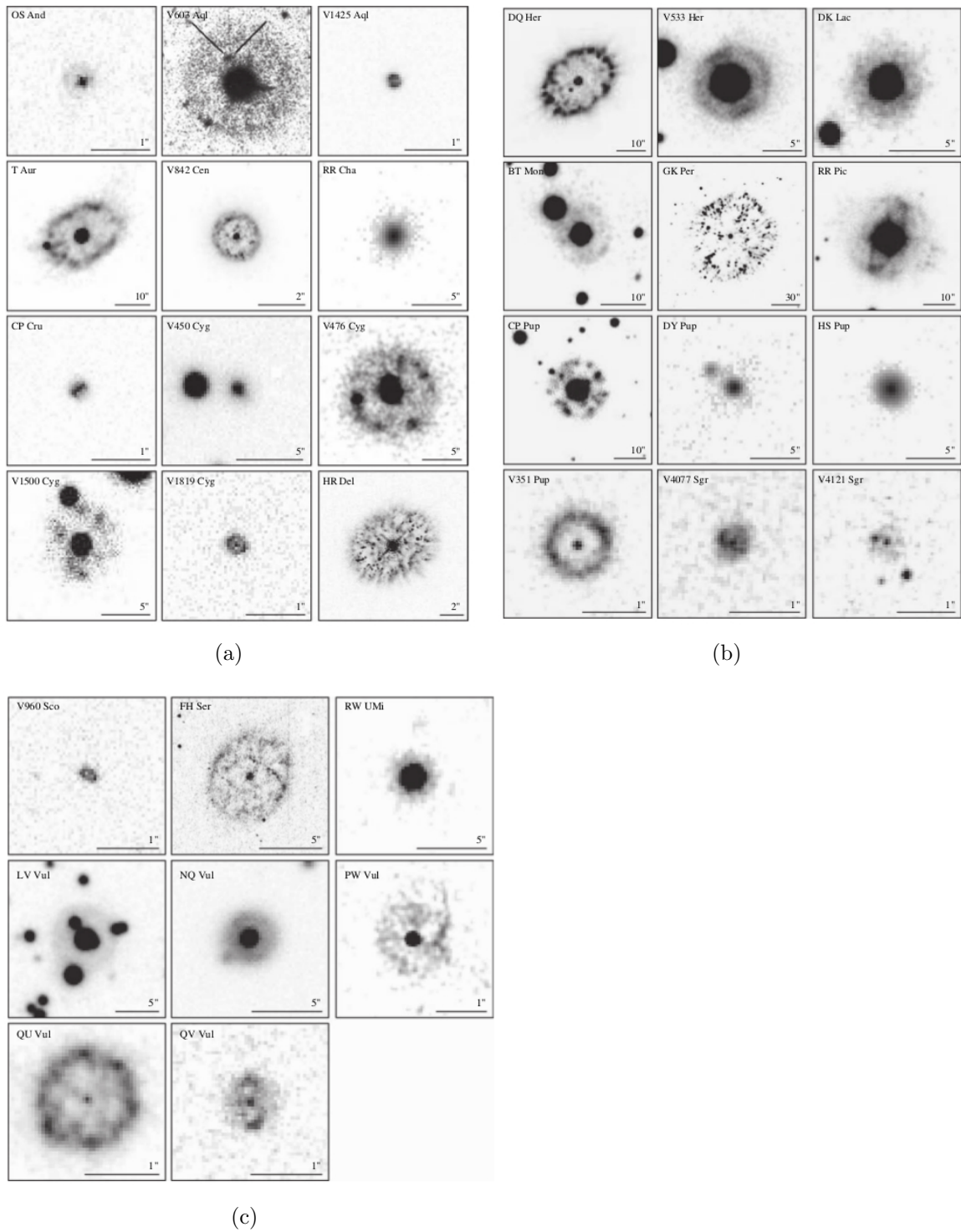


Figure 1.10: Nova shell images from Bode & Evans (2008).

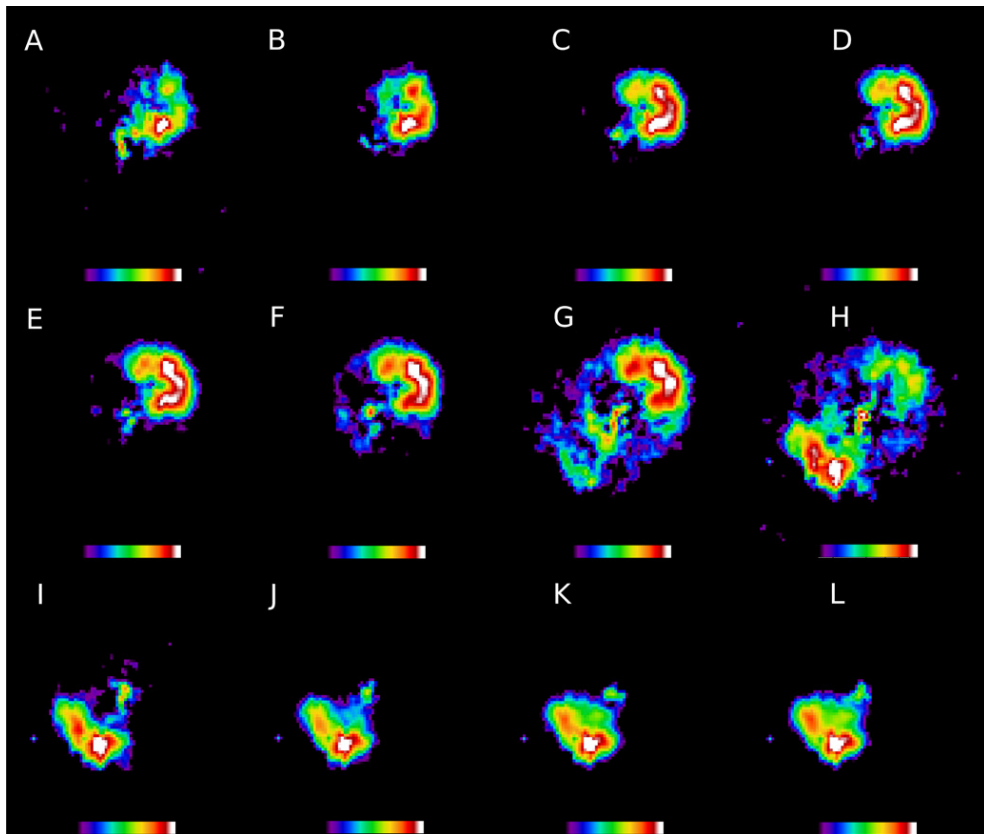


Figure 1.11: Maps of O[III] 5007Å from 900 km s^{-1} to 540 km s^{-1} from panels (A) to (L) with steps of 120 km s^{-1} or 2\AA . The blue-shifted polar cap at the upper right and red shifted polar cap at the lower left can be seen. All maps have equal intensity scales from 1×10^{-16} to $2 \times 10^{-15} \text{ erg s}^{-1} \text{ cm}^{-2}$ and the same velocity range. From Moraes & Diaz (2009).

resulting from a bipolar ejection. They found that features such as equatorial rings, belts and polar caps could result from projection effects. It appears that these bipolar features are present in most nova shells, and can be seen in many of the shells shown in Figure 1.10.

1.7 Nova induced cycle theory aka hibernation theory

As noted in Section 1.4.3, the orbital distribution of CVs shows that novalikes and dwarf novae co-exist at the same orbital period, and have different mass transfer rates, \dot{M} . We briefly discussed one theory to explain the range of \dot{M} , which suggested that the irradiation of the secondary by the WD could cause enhanced \dot{M} for a limited time. However, it was noted that this theory had a number of weaknesses.

Another hypothesis to explain the variations in \dot{M} is a *nova-induced cycle*, also known as *hibernation theory*. The nova eruption will cause mass to be lost from the system and hence the orbital separation will increase. In turn, the radii of the Roche lobes would increase, causing mass transfer to reduce. However, some fraction of the energy released in the nova event will heat up the WD, leading to increased irradiation and subsequent bloating of the secondary. This would cause an increase in the accretion rate which would counteract the effect on the increased separation. Collazzi et al. (2009) found that the accretion rates for most classical and recurrent nova eruptions, as measured via their *B*-band magnitudes, remain at similar NL levels across the nova eruption. As the WD cools, the radius of the secondary would return to its secular value, \dot{M} will reduce to $\sim 10^{-10} M_{\odot}$ and the system changes to a DN. If the secondary relaxes within its Roche lobe, then mass transfer would cease and the system would go into hibernation. Eventually angular momentum losses would bring the secondary back into contact with its Roche lobe and accretion would recommence at DN levels. As the accretion energy heats up the WD, the secondary will in turn be heated and bloated, and accretion rates will rise, possibly to NL levels. Ultimately another nova

eruption will occur and the cycle repeats. In this model, therefore, CVs are expected to cycle between nova, NL and DN states and possibly hibernation, on timescales of $10^4 - 10^6$ yrs, thereby explaining the co-existence of these CV sub-types at the same orbital period. The cycle is illustrated graphically in Figure 1.12.

The theory was first proposed by Shara et al. 1986 to explain why the observed space density of novae and novalikes was two orders of magnitudes below theoretical population synthesis models at the time. The theory had some early criticisms and conflicting results by Naylor et al. (1992), Mukai & Naylor (1995), and Somers et al. (1996, 1997), and the theory still does not enjoy wholehearted acceptance (Knigge et al., 2011).

The cyclical evolution of CVs through nova, NL and DN phases received observational support from the discovery that BK Lyn appears to have evolved through all three phases since its likely nova outburst in the year AD 101 (Patterson et al., 2013). However, the AAVSO light curve of BK Lyn suggests that it has now reverted back to a NL state, indicating that the object is a Z Cam-type DN that has likely been transitioning from the NL to DN state for much less than the ~ 2000 -yr estimate of Patterson et al. (2013). Further support for the nova-induced cycle theory has come from the discovery of nova shells around the dwarf novae Z Cam and AT Cnc (Shara et al. 2007, Shara et al. 2012), verifying that they must have passed through an earlier nova phase. Shara et al. (2017) also found a nova shell from Nova Sco 1437 and were able to associate it with a nearby dwarf nova using its proper motion. Mróz et al. (2016) found that V1213 Cen (Nova Cen 2009) exhibited dwarf nova outbursts six years before the nova event, and was two orders of magnitude brighter afterwards, in a novalike state. Some candidate systems in hibernation have also been found (e.g. Gänsicke et al. 2004; Thorstensen et al. 2009).

As I discuss in Chapter 5, the theory is supported by the discovery of nova shells around three dwarf novae (Shara et al. 2007, 2012, 2017), verifying that they must have passed through an earlier nova phase. A more obvious place than DNe to find nova shells is actually around NLs, as the nova-induced cycle theory suggests that the high

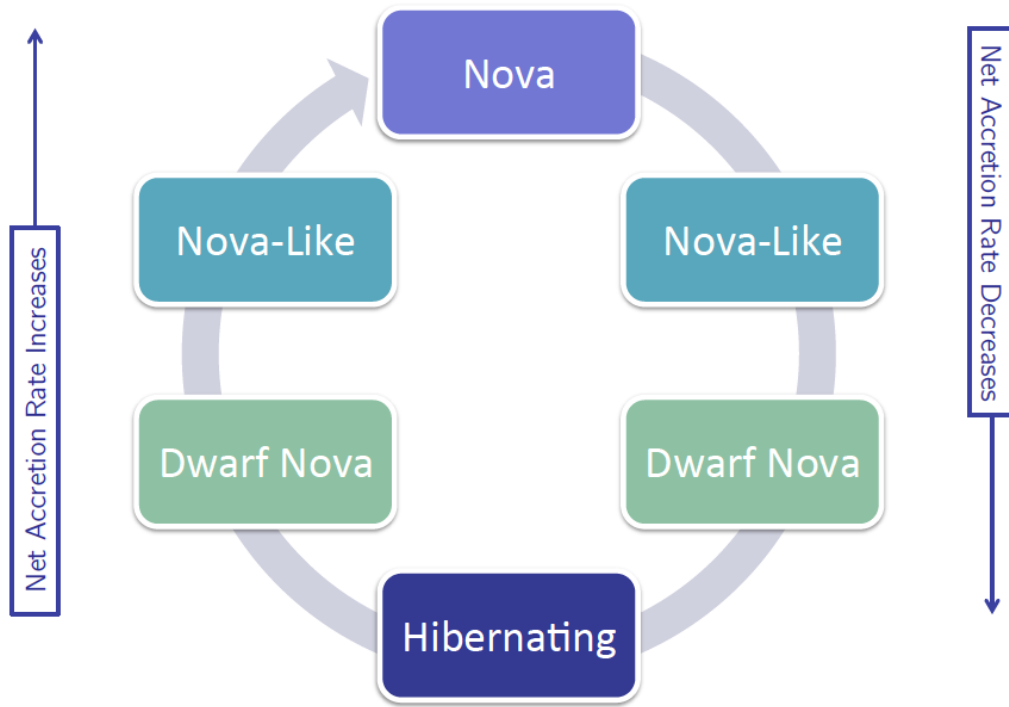


Figure 1.12: Graphic showing the nova-induced cycle. From Pagnotta (2015)

\dot{M} in NLs could be due to a recent nova eruption. Finding shells around the highest accretion-rate NLs would lend further support to the existence of nova-induced cycles and hence help explain why systems with different \dot{M} are found at the same orbital period.

We can now go on to consider the ultimate fate of CVs, and whether they are the progenitors of type Ia supernovae.

1.8 CVs as progenitors of Type Ia Supernovae

Type Ia Supernovae (SNIa) play a key role in modern cosmology. The rate of decline of their light curves and their intrinsic luminosities are directly correlated (Phillips, 1993) and so they provide an ideal standard candle to measure cosmological distances more reliably than other techniques currently available. The discovery of the accelerating expansion of the Universe by Riess et al. (1998) and Perlmutter et al. (1999) was made using SNIa. However, despite over thirty years of research, their progenitors are

not yet satisfactorily explained. The canonical view (Hoyle & Fowler, 1960) is that SNIa are due to the thermonuclear explosion of a near-Chandrasekhar mass (M_{Ch}) carbon-oxygen (CO) white dwarf. See Livio & Mazzali (2018) and Patat & Hallakoun (2018) for recent reviews.

The core of the WD is fused into iron-group elements and some intermediate mass elements. The luminosity is powered by the radioactive decay of $\sim 0.6 M_{\odot}$ of ^{56}Ni which releases of $\sim 10^{51}$ erg and a similar contribution from the other $\sim 0.8 M_{\odot}$ radioactive species of iron-group elements. Hence approximately 2×10^{51} erg is available. The unbinding of a $1.4 M_{\odot}$ WD takes $\sim 0.5 \times 10^{51}$ erg. The radiated energy accounts for only $\sim 0.5 \times 10^{49}$ erg, so the remaining energy is imparted as kinetic energy of the ejecta, giving rise to ejection speeds of 10^4 km s^{-1} .

Other key features of SNIa are lack of hydrogen or helium in their spectra, violent explosions pointing to a runaway process, and they are observed in both young and old stellar populations.

A number of possible progenitor models have been put forward, and the principal theories are listed below:

- WD and a main sequence or evolved companion
- WD and WD pair
- WD pair plus a third star
- WD and the core remnant of a normal star
- Single isolated WD

I discuss each of these suggested progenitors in the following sections.

1.8.1 WD with a main sequence or evolved companion

This scenario consists of a WD in a close binary orbit with a companion which is non-degenerate e.g. a main sequence star, a helium star or a red giant (Whelan &

Iben, 1973). It is known as the single degenerate (SD) model and at one time was the favoured progenitor model (Livio & Mazzali, 2018). In the SD, the WD accretes matter from its companion, either by Roche-lobe overflow or by wind-accretion, and gradually approaches M_{Ch} , despite mass loss during nova eruptions. Just prior to the point at which the white dwarf would undergo gravitational collapse, carbon fusion begins in the core of the white dwarf, and leads to a runaway thermonuclear explosion which disrupts the entire WD. This would explain the homogeneity seen in the luminosities of SNIa.

This model includes many classes of CVs, including recurrent and classical novae and symbiotic stars.

1.8.2 WD and WD pair

In this case, two CO WDs, with a combined mass greater than M_{Ch} , lose angular momentum through the emission of gravitational waves. This causes their orbital separation to shrink, leading to the lighter WD filling its Roche lobe and becoming tidally disrupted, eventually forming an accretion disc around the primary WD and ultimately into a single merged WD (see Figure 1.13). In certain conditions (Sato et al., 2015), this ultimately leads to an explosion as a SNIa. This channel is commonly referred to as the double degenerate (DD) model.

1.8.3 WD pair plus a third star

In this scenario, two WDs are driven to merger through their interaction with a passing third star (Rosswog et al., 2009). Similarly, the orbit of the two WDs in the inner binary of a hierarchical triple system can be driven to high eccentricity by the third star, through Kozai-Lidov resonances (Lidov 1961, Kozai 1962), eventually leading to merger. Numerical simulations by Kushnir et al. (2013) provide evidence that this scenario could account for a significant fraction of SNIa. However, their models assumed a zero impact parameter for all collisions, which is clearly unlikely to

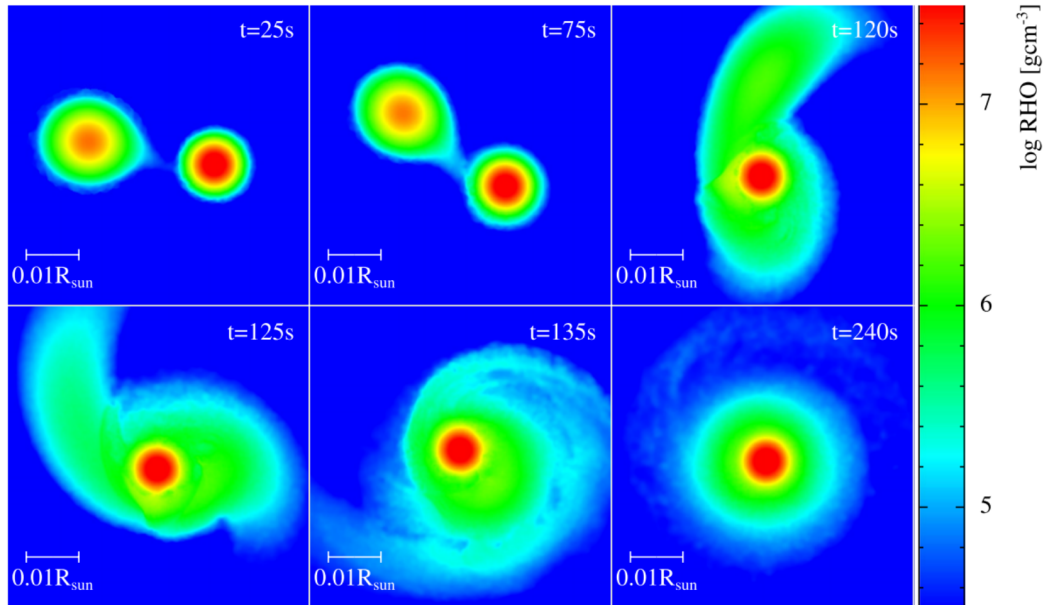


Figure 1.13: Graphic showing the simulation the merger of two WDs, in the equatorial plane. The colours indicate density on a logarithmic scale, as shown in the key on the right. From Sato et al. (2015)

be the case, and so further modelling of non-zero cases is needed.

1.8.4 WD with the core remnant of a normal star

Sometimes called the core-degenerate (CD) scenario (Livio & Riess, 2003), this model envisages the merger of the WD and the core of an AGB star during the common envelope stage or shortly after the common envelope phase, within $\sim 10^5$ yr of it. It was first invoked to explain the detection of $H\alpha$ in the spectra of the peculiar SNIa SN 2002ic (Hamuy et al., 2003). The model was subsequently developed by Ilkov & Soker (2012) who proposed that the CD model is a feasible channel for all SNIa, if proper account is taken of magnetic braking to aid the spin down of any merged WD that is $> M_{\text{Ch}}$. However, population synthesis models by Zhou et al. (2015) showed that they can only account for a small fraction of the total SNIa rate.

1.8.5 Single isolated WD

In a recent review, Chiosi et al. (2015) explored the possibility that isolated CO WDs could undergo SNIa explosions triggered by pycno-nuclear runaway reactions (nuclear

reactions caused by high density) between carbon and light elements, predominantly hydrogen and helium. Their semi-empirical models suggest that impurities of light elements embedded in the C-O ionic lattice lead to sufficient reaction rates of ${}^1\text{H} + {}^{12}\text{C}$ and ${}^4\text{He} + {}^{12}\text{C}$ to ignite Carbon-Carbon burning and hence to a thermonuclear runaway. However, their models assume trace levels of H and He in the core of the WD, whereas existing WD formation theories suggest that hydrogen is entirely depleted in WD cores. Also their models suggest that WDs with masses as low as $0.85 M_{\odot}$ could explode as SNIa. This implies that most would occur significantly below M_{Ch} and cannot therefore explain the bulk of SNIa, which have $\sim 1.4 M_{\odot}$ of residual mass.

1.8.6 Observational evidence for SD and DD models

The SD and DD models remain as the two favoured progenitor scenarios. However, the observational evidence provides no clear preference for either model, and each has its strengths and weaknesses (Livio & Mazzali, 2018). The DD can readily explain the lack of hydrogen seen in most SNIa spectra, as all the hydrogen has been processed by the time of the merger (Hamuy et al. 2003; Livio & Riess 2003). The DD is also favoured by the non-detection of any confirmed progenitors or survivors of nearby SNIa (Kerzendorf et al. 2009; Schaefer & Pagnotta 2012), and the lack of spectral features from the impact of the supernova forward shock with the secondary star (Badenes et al., 2007) or the circumstellar material blown off the secondary prior to the explosion (Leonard, 2007). For example, the nearest SNIa in decades, SN2011fe in M101, has been observed at multiple wavelengths and at multiple epochs, and shows no trace of interactions with either circumstellar material or a progenitor, nor any evidence of a companion (Nugent et al. 2011; Horesh et al. 2012; Bloom et al. 2012; Brown et al. 2012). This rules out most SD channels for this event. However, there is evidence against the DD from large-scale surveys looking at populations of white dwarfs (e.g. Napiwotzki et al. 2007; Badenes & Maoz 2012) which have detected insufficient numbers of high mass white dwarf pairs to account for the observed SNIa rate. Simulations of

double white dwarf mergers also suggest that most mergers would lead to accretion induced collapse to form a neutron star rather than SNIa explosions (Shen et al. 2012).

Studies of the delay time distribution of SNIa since star formation show a bimodal distribution, suggesting that perhaps both the SD and DD channels contribute to the overall SNIa rate (Andersen & Hjorth, 2018). Some SNIa seem to be derived from super- M_{Ch} white dwarfs, which favours the DD, whereas other low-luminosity SNIa suggest they were derived from sub- M_{Ch} white dwarfs (Goldstein & Kasen, 2018), which neither model can easily account for, but which are better explained as a sub-class of the DD models comprising sub- M_{Ch} CO and He white dwarf pairs (Sim et al. 2012). In these ‘double detonation’ models, the He-rich material is transferred to the CO white dwarf. As the temperature and pressure of the accreted layer build up, it detonates and the shock creates a detonation in the core of the CO white dwarf. Pakmor et al. (2013) and Shen et al. (2013) have found that these models can also explain other features of SNIa previously only explained by SD channels.

A small number of SNIa spectra show variable sodium absorption lines, and the variability has been attributed to the impact with circumstellar material (Simon et al., 2009), thereby supporting the SD. However Shen et al. (2012) give other DD-based interpretations of these results e.g. the SD scenarios require a certain amount of fine-tuning for the white dwarf to accumulate mass due to the mass loss in nova events (Hachisu et al. 1999). However, support for this fine tuning has come from Schaefer (2011), who measured a small change in the orbital period of CI Aql across its 2000 eruption thereby showing a net increase in the mass of the white dwarf. Further modelling by Hillman et al. (2016) also shows that WDs can grow in mass despite repeated hydrogen and helium flashes in the accreted layer.

One of the more favoured candidates in the SD model are recurrent novae (RNe). The recurrence of outbursts is attributed to the near- M_{Ch} mass of the white dwarf in these systems, because the higher gravitational pressure at the base of the accreted layer means that less mass needs to be accreted to trigger a nova eruption. This has been confirmed for the recurrent nova U Sco, which was found to have a white

dwarf mass of $1.55 \pm 0.24 M_{\odot}$ (Thoroughgood et al., 2001). This made U Sco the only dynamical (and hence reliable) white dwarf mass determination in a RN. The technique of dynamical mass determination requires the system to be both eclipsing and to show spectral features of the secondary star.³ This is the technique I used to determine the masses of the two stars in CI Aql.

1.9 This Thesis

The results of my research into the evolution of CVs are set out in the following chapters. In Chapter 2, I present my determination of the masses of the two stars in CI Aql, together with other system parameters, using time-resolved spectroscopy. In Chapter 3, I set out the results of my first campaign to search for nova shells around CVs using deep $H\alpha$ images, and a search through an $H\alpha$ survey centred on the Galactic plane. I report on a number of tentative discoveries from this first campaign. Then in Chapter 4, I present the results of my second nova shell search, and discuss the combined findings from both of my searches and those of other researchers, in the context of the nova induced cycle theory. In Chapter 5, I present my discovery of a nova shell around V1315 Aql, and describe the various shell parameters that I was able to determine using high resolution spectroscopy. Finally, in Chapter 6, I summarise my research and discuss possible future work.

³It is also possible to use ellipsoidal variations in non-eclipsing systems to determine the inclination, but this is less reliable due to the presence of flickering and other phase-dependent light variations, e.g. due to a bright spot.

Chapter 2

CI Aquilae: a Type Ia supernova progenitor?

The contents of this chapter have been published in Monthly Notices of the Royal Astronomical Society, in a manuscript entitled ‘*CI Aql: a Type Ia supernova progenitor?*’ by Sahman, Dhillon, Marsh, Moll, Thoroughgood, Watson and Littlefair (Sahman et al., 2013). The observations were taken by Chris Watson and Tim Thoroughgood on 2003 June 10–12 using the 4.2m William Herschel Telescope (WHT) on La Palma. The spectra were reduced by Sarah Moll under the supervision of Vik Dhillon. All subsequent data analysis and the following text are my own work.

2.1 Introduction

As I discussed in Section 1.8, the determination of accurate masses of the components of RNe is essential to constrain models of their evolution and to establish whether they are potential progenitors of SNIa. We can measure the orbital periods very accurately using high speed photometry. However, determining the masses of the two stars is more problematic. There are a number of techniques for the determination of masses in CVs, but the most reliable uses a combination of the radial velocity of the secondary, K_R , the projected rotational velocity of the secondary, $v\sin i$ and the

eclipse full width at half depth, $\Delta\phi_{1/2}$ (see Smith & Dhillon 1998 for a review). These methods do have biases e.g. due to the irradiation of the secondary, but these can be corrected for. This is the method I used to determine the masses of the two stars in the recurrent nova CI Aql.

CI Aql was first recorded in outburst in 1917 (Reinmuth, 1925). Duerbeck (1987) suggested that it was either a dwarf nova with a long cycle length or a nova whose maximum was missed. The second recorded outburst of CI Aql was reported in May 2000 (Takamizawa et al. 2000; Yamaoka & Shirakami 2000), with a magnitude of $m_V \sim 7.5$, which secured its place amongst the 10 known RNe. Schaefer (2001) found archival evidence of another outburst in 1941. This led him to propose that CI Aql has an outburst recurrence timescale of approximately 20 years, with the 1960 and 1980 outbursts failing to have been observed. However, the timescales of RN outbursts often vary, and the low accretion rate prior to the 2000 outburst, implied from their light-curve analysis model, led Lederle & Kimeswenger (2003) to suggest that there were no outbursts between those of 1941 and 2000. CI Aql shows eclipses on an orbital period of 14.8 hours, and has a quiescent magnitude of $m_V \sim 15.7$ (Lederle & Kimeswenger, 2003). The pre-outburst quiescent optical spectrum showed emission lines of helium and the Bowen complex on a reddened continuum, with all Balmer lines in absorption (Greiner et al., 1996). Lynch et al. (2004) took infrared spectra at eight epochs between days 3 to 391 from peak brightness of the 2000 outburst. They found that the spectra were very similar to other RNe, except for an over-abundance of nitrogen lines, suggesting that there was mixing of the white dwarf material with the accreted matter. This implies that the ejecta contained dredged-up white dwarf material, weakening the hypothesis that only accreted matter is ejected during the nova event. However, Schaefer (2011) measured the period change across the outburst in 2000, from which he derived the mass of the ejecta. Comparing this to the mass transfer rate measured by Hachisu & Kato (2003) and the recurrence period measured in Schaefer (2010), he found that the WD mass was increasing i.e. the nova eruption ejected less mass than had been accreted since the previous eruption. Subsequently,

Wilson & Honeycutt (2014) attempted to measure the change in the WD mass across the 2000 nova eruption using my measured parameters and their previous quiescent photometry. Unexpectedly they found that the WD mass had *increased* across the eruption which is physically impossible. They attribute this odd result to the lack of accurate ephemeris data just prior to the eruption.

The discovery of the 2000 outburst of CI Aql drew attention to this RN system, as it is eclipsing and the secondary is visible in the spectra, making it an ideal candidate for mass determination. In this chapter, I use time-resolved spectroscopy of CI Aql to determine the radial and rotational velocity of the companion star and orbital inclination of the system, and hence measure the masses of the two component stars.

2.2 Observations

The data were recorded over three nights from 2003 June 10–12 with the WHT, when the target recurrent nova CI Aql was in quiescence. A full orbit was observed ($P_{\text{orb}} = 14.8$ hr) during this time, including a primary eclipse. The spectra were taken with ISIS, a double-armed, intermediate resolution spectrograph ($R = 158 - 2400$ in blue and $R = 158 - 1200$ in red). It utilises dichroic beamsplitters to allow simultaneous observing in the red and blue arms. There is a $\sim 200\text{\AA}$ range of reduced throughput at the dichroic crossover wavelength from reflection to transmission.

We obtained 184 spectra of CI Aql simultaneously in red and blue wavebands with a slit width of 1 arcsec. For the red arm, the Marconi2 CCD (2148×4700 pixels) was used, with the R1200R grating, giving a wavelength range of $\lambda\lambda 6041\text{--}6877\text{\AA}$ and a resolution of 43 km s^{-1} . The blue arm was configured with the EEV12 CCD (2148×4200 pixels) and the R1200B grating, giving a wavelength range of $\lambda\lambda 4570\text{--}5370\text{\AA}$ and a resolution of 55 km s^{-1} . All exposures were 600s. A comparison star was placed on the slit each night to correct for slit losses. Spectra of several stellar templates of luminosity classes III–V ranging from F8 to M0 spectral type were also taken. A flux standard star and telluric correction star were also observed on each night to convert between counts and

Table 2.1: Journal of WHT observations for CI Aql. Orbital phase is calculated using the ephemeris presented in Section 2.4.2.

UT date (at start of night)	UT start	UT end	No. of spectra	Phase start	Phase end
2003 June 10	23: 44	05: 02	29	0.37	0.71
2003 June 11	23: 21	05: 09	31	1.95	2.34
2003 June 12	23: 41	05: 37	32	3.58	3.99

flux, and to remove atmospheric absorption lines from the spectra, respectively. Arc frames were taken between every five CI Aql spectra to calibrate the wavelength scale, and to account for spectrograph flexure at different telescope positions; the root-mean-square error in the fourth-order polynomial fits to the arc lines was $\sim 0.009\text{\AA}$. Flat-field frames and bias frames were also taken to correct for detector artefacts during the data reduction. At the end of the first night, the bias frames for the blue chip exhibited a sinusoidal pattern down the CCD, caused by a faulty controller. This pattern was present throughout night 1. A new controller was used for nights 2 and 3 and the pattern was no longer present.

The seeing varied between 1 and 3 arcsec and the sky was photometric on all three nights except for cirrus for two hours on the second night and some cirrus early on the third night. A journal of the observations is given in Table 2.1.

2.3 Data Reduction

All spectra were reduced by Sarah Moll under the supervision of Prof. V. Dhillon using the STARLINK packages FIGARO and PAMELA. Subsequent analysis of the spectra was performed by me using Tom Marsh's MOLLY software. As noted in Section 2.2, the bias frames for the blue chip on night 1 showed a sinusoidal pattern caused by a faulty CCD controller. This pattern varied throughout the night so it was not possible to remove it by averaging the bias frames and subtracting. Instead, each science frame for all three nights was debiased using a clipped mean of the bias overscan strip.

Pixel-to-pixel sensitivity variations were corrected using a master tungsten lamp flat-field, compiled from the median of 40 exposures with counts in the range 20,000 – 50,000. Any flats with counts outside this range were discarded. The sky was subtracted by fitting second-order polynomials in the spatial direction to the sky regions on either side of the object spectra. The data were then optimally extracted (Horne & Marsh, 1986) to give raw spectra of CI Aql and the comparison star. Arc spectra were extracted from the same locations on the detector as the targets. The wavelength scale for each spectrum was interpolated from the wavelength scales of two neighbouring arc spectra. The root-mean-square errors in the fourth-order polynomial fits to the arc lines was $\sim 0.008\text{\AA}$ in the red, and $\sim 0.010\text{\AA}$ in the blue. A third-order spline fit to the continuum of the spectro-photometric standard star was used to remove the large-scale variations of instrumental response with wavelength. The slit-loss correction was performed by dividing the CI Aql spectra by spline fits to the comparison star spectra, and then multiplying the resulting spectra by a spline fit to a wide-slit comparison star spectrum.

2.4 Results

2.4.1 Light curves

The slit-loss corrected light curves of CI Aql are presented in Figure 2.1. The red ($\lambda\lambda 6079\text{--}6838\text{\AA}$) and blue ($\lambda\lambda 4585\text{--}5319\text{\AA}$) continuum light curves show a primary eclipse of approximate depth 0.6 magnitude, and a dip of depth 0.1 magnitude at phase 0.5. The continuum light curves have two components, an eclipse of the white dwarf, and ellipsoidal modulation of the secondary, the latter being confirmed using the equations given by Morris & Naftilan (1993) and the coefficients for limb and gravity darkening of Claret & Bloemen (2011), in conjunction with the parameters derived in Section 2.4.9: assuming an F-type star, with gravity darkening of 0.1424, a linear limb darkening coefficient of 0.4885, and solar metallicity, gives a flux change of 0.20. This

is apparent in both the red and blue continuum light curves.

Schaefer (2010) notes that there is flickering present throughout the light curve, except during the primary eclipse. This suggests that the flickering originates in the disc. The light curve in Figure 2.1 shows flickering around phase 0.7, which is consistent with this picture.

The middle panel of Figure 2.1 shows the light curve for He II, which exhibits a broad eclipse-like feature that appears to begin earlier and end later than the continuum eclipse. This is consistent with an origin on the inner hemisphere of the secondary star.

The lower two panels show the light curves for the H β and H α lines. The H β and H α lines are in absorption, although H α goes into emission around phase 0.5. Both light curves show weakest absorption at phases 0 and 0.5, suggesting that the absorption originates on the inner hemisphere of the secondary whilst the emission originates from the white dwarf or the disc.

2.4.2 Ephemeris and orbital period

The time of mid-eclipse was determined by fitting a Gaussian to the eclipse minimum of the continuum light curves in Figure 2.1, giving a value of $T_{mid-eclipse} = \text{HJD } 2452802.5145(3)$. This zero-point was used in conjunction with the orbital period reported in Lederle & Kimeswenger (2003), $P = 0.6183634(3)$ day, to place our data on a phase scale. Note that Schaefer (2011) used data from 80 eclipse timings to derive a period of $P = 0.6183609(5)$ day, which is not sufficiently different to affect the results presented here. Schaefer (2011) also found no evidence for a non-zero value of \dot{P} .

2.4.3 Average spectrum

The average blue and red spectra are shown in Figure 2.2. Note that the spectra have not been corrected for orbital motion, and so the weaker spectral features will be smeared out. Absorption features from the secondary star, such as Mg Ib, Ca I and Fe I are visible, as well as high-excitation emission features such as He II and the C III/N III

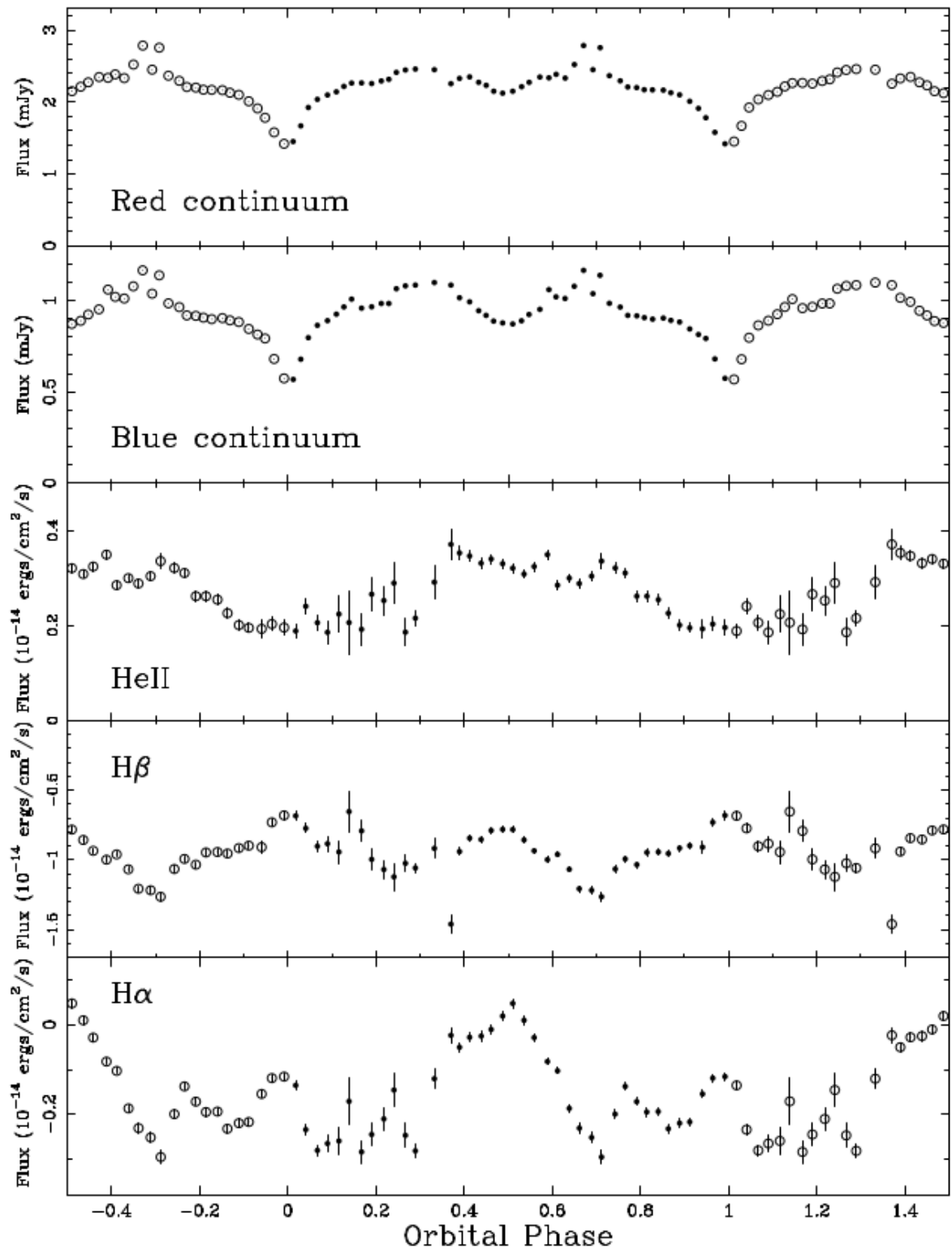


Figure 2.1: Continuum and emission-line light-curves of CI Aql. The data with open circles have been folded over from the real data (solid points) for clarity.

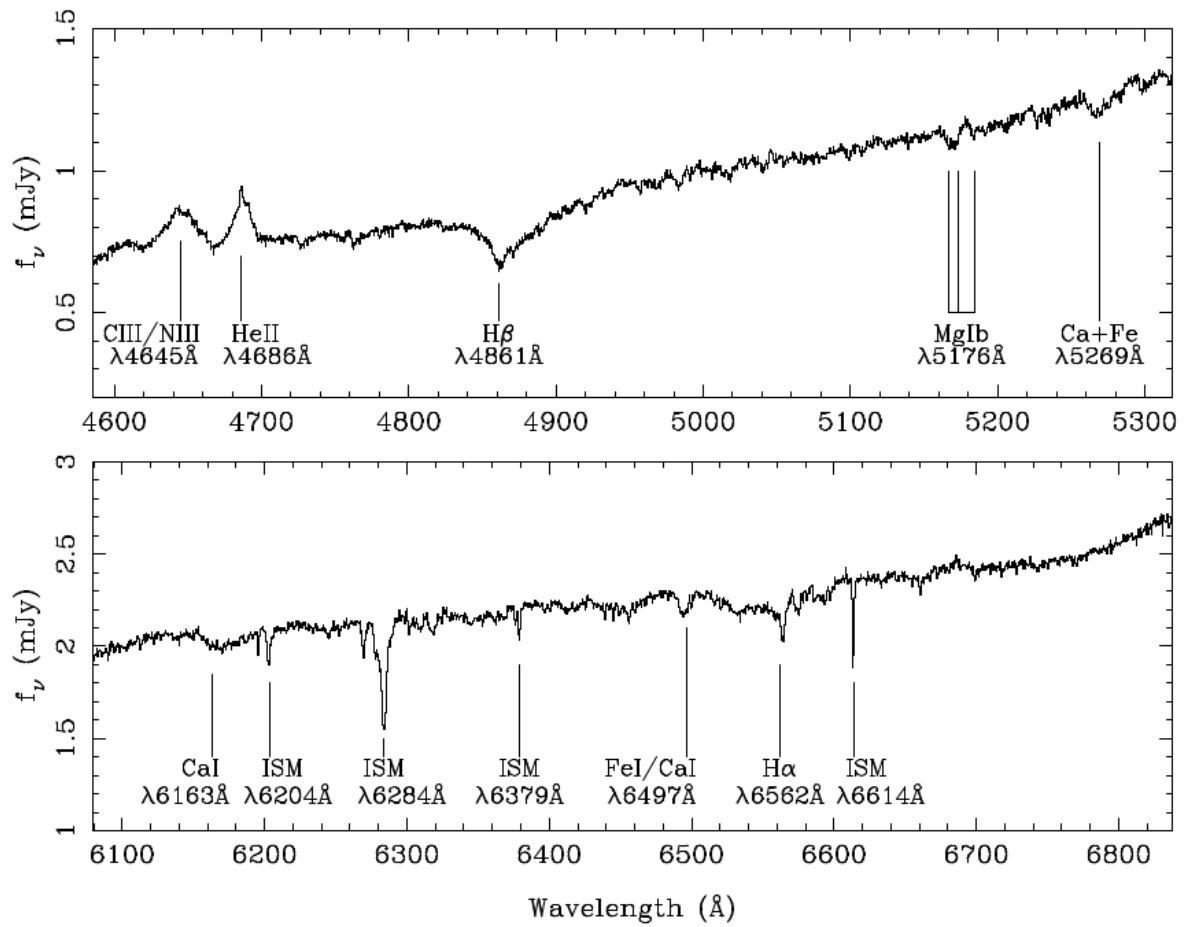


Figure 2.2: The average blue (top) and red (bottom) spectra of CI Aql, uncorrected for orbital motion.

Table 2.2: Fluxes and equivalent widths of prominent lines in CI Aql, measured from the average spectrum.

Line	Flux $\times 10^{-14}$ (erg cm $^{-2}$ s $^{-1}$)	EW (\AA)	FWHM (km s $^{-1}$)	FWZI (km s $^{-1}$)
He II $\lambda 4686\text{\AA}$	3.07 ± 0.04	3.07 ± 0.04	860 ± 100	1720 ± 200
C III/N III $\lambda 4645\text{\AA}$	3.91 ± 0.05	3.80 ± 0.05	1500 ± 300	2790 ± 400
H β	-11.05 ± 0.08	-10.02 ± 0.07	1700 ± 400	6700 ± 1000

complex. The Balmer lines are in absorption but my later analysis (see Section 2.4.4) will show them to be a combination of absorption and emission components. Table 2.2 shows the fluxes, equivalent widths and velocity widths of the more prominent lines in the average spectra.

2.4.4 Trailed spectra and Doppler tomography

The trailed spectrum of the $\lambda\lambda 5150\text{--}5290\text{\AA}$ region is shown in Figure 2.3, highlighting absorption features of Mg Ib, Ca I and Fe I. Note that the increased noise around phases 0.1–0.4 is due to clouds. The absorption lines show a clear sinusoidal motion, which is red-shifted after phase 0 and crosses to blue-shifted at phase 0.5, indicating that they originate on the secondary. This part of the spectrum is used in the determination of the radial velocity of the secondary (see Section 2.4.6)

The trailed spectra of the C III/N III, He II, H β and H α lines are shown in Figure 2.4. The C III/N III and He II trails show sinusoidal motion, which is blue-shifted after phase 0 and crosses to red-shifted at phase 0.5. This indicates that the lines originate from the disc or the white dwarf. The He II trail shows two components, a narrow, approximately constant-velocity feature centred on zero velocity, and a sinusoidal feature. The constant-velocity feature must be located very close to the centre of mass of the system, and the source of this feature is explored below. The H β trail is dominated by an absorption feature that moves in phase with the Mg Ib, Ca I and Fe I features in Figure 2.3, and so most likely originates on the secondary. The H α trail shows two distinct elements moving in anti-phase to each other. There is a strong emission feature (dark grey-scales) associated with the disc and an absorption feature

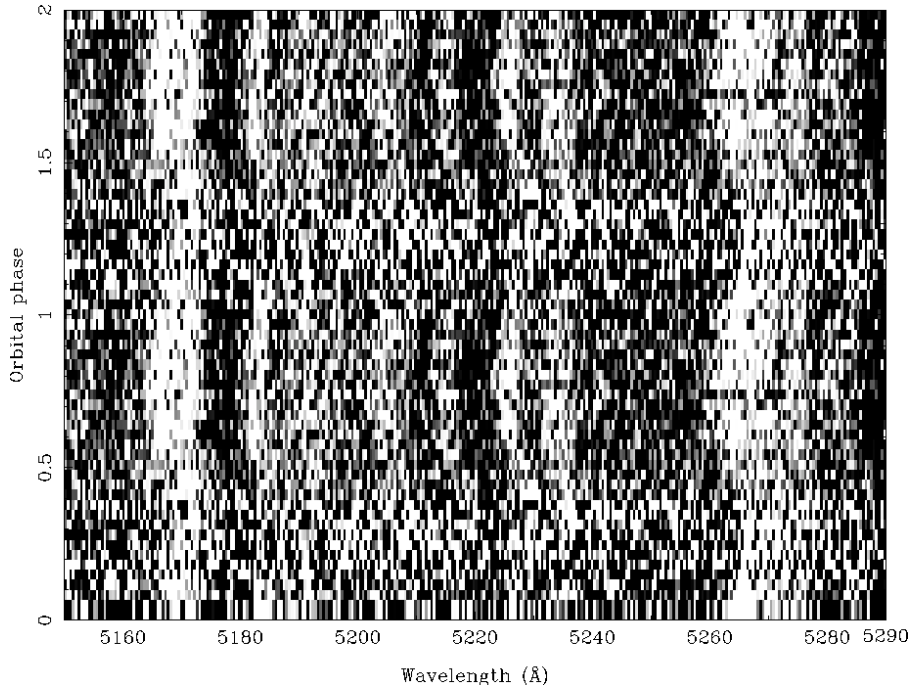


Figure 2.3: Trailed spectra of the $\lambda\lambda 5150 - 5290\text{\AA}$ region, showing absorption features (lighter grey-scales) of MgIb, CaI and FeI from the secondary. The data have been folded in orbital phase for clarity. Note that the noisier data visible around phases 0.1–0.4 are due to a period of cloud. This is also evident in Figures 2.4, 2.6, 2.9 & 2.10.

(light grey-scales) from the secondary.

In order to help determine the origin of the features in the trailed spectra, I constructed Doppler tomograms. Doppler tomography is an indirect imaging technique that maps emission/absorption features in the spectrum into velocity space. For a detailed review of Doppler tomography see Marsh (2000). This technique assumes, amongst other things, that all points are equally visible at all times and that the flux from any point in the rotating frame is constant. These assumptions are violated to some extent in CI Aql e.g. occultation of the bright spot by the disc, causing features to smear in the maps. Nevertheless, the location and relative strengths of the strongest features are reliably reproduced, as can be confirmed by inspecting the trailed spectra. Figure 2.5 shows Doppler maps for the He II $\lambda 4686\text{\AA}$ and H α lines. The He II emission appears to emanate from two principal areas, the disc and the centre of mass of the system, which is coincident with the irradiated face of the secondary. This explains the narrow constant velocity feature seen in the trailed spectra in Figure 2.4. The H α map contains a region of strong emission, indicated by darker grey-scales, which is

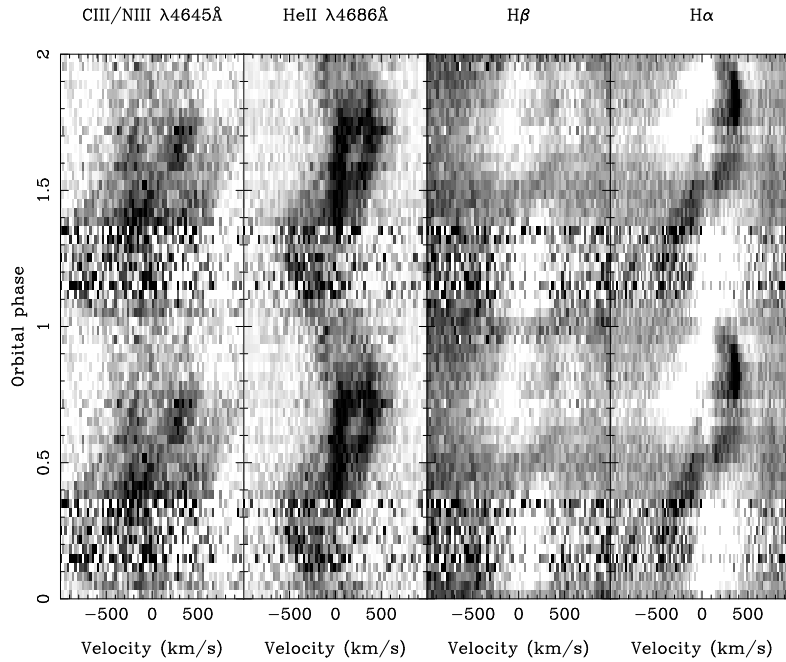


Figure 2.4: Trailed spectra of the C III/N III $\lambda 4645\text{\AA}$, He II $\lambda 4686\text{\AA}$, H β and H α lines, with emission/absorption shown in dark/light grey-scales. The data have been folded in orbital phase for clarity.

located on the disc, and a region of strong absorption, indicated by lighter grey-scales, coincident with the secondary.

2.4.5 Radial velocity of the white dwarf

It is not possible to measure the radial velocity of the white dwarf directly. Instead, I measured the motion of the emission-line wings, since these are presumably formed in the inner parts of the accretion disc and should therefore reflect the motion of the white dwarf with the highest reliability. I used the double-Gaussian method of Schneider & Young (1980), since this technique is sensitive mainly to the motion of the line wings. The continuum-subtracted spectra were binned on to a constant velocity-interval scale about each of the emission-line rest wavelengths. The Gaussian widths were varied from 150 to 300 km s^{-1} (FWHM) and their separations varied from 400 to 1200 km s^{-1} . I then fitted the radial velocities, v , to the function

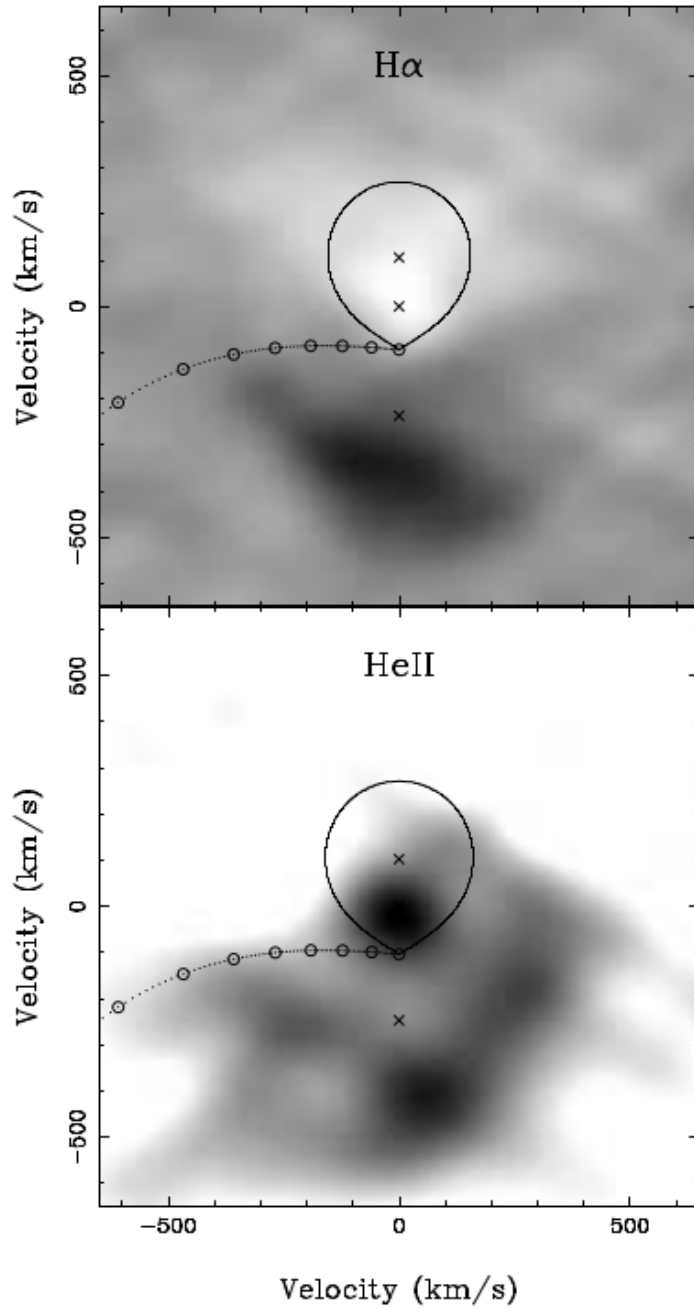


Figure 2.5: Doppler map of H α (top) and He II $\lambda 4686\text{\AA}$ (bottom). The three crosses represent the centre of mass of the secondary (upper cross), the centre of mass of the system (middle cross), and the centre of mass of the white dwarf (lower cross). The Roche lobe of the secondary star and the predicted trajectory of the gas stream have been plotted using the mass ratio, $q=M_2/M_1 = 2.35$ derived in Section 2.4.9. The series of circles along the path of the gas stream mark the distance from the white dwarf at intervals of $0.1R_{L1}$, ranging from $1.0R_{L1}$ at the secondary star to $0.3R_{L1}$ at the point of closest approach, where R_{L1} is the distance from the white dwarf to the inner Lagrangian point.

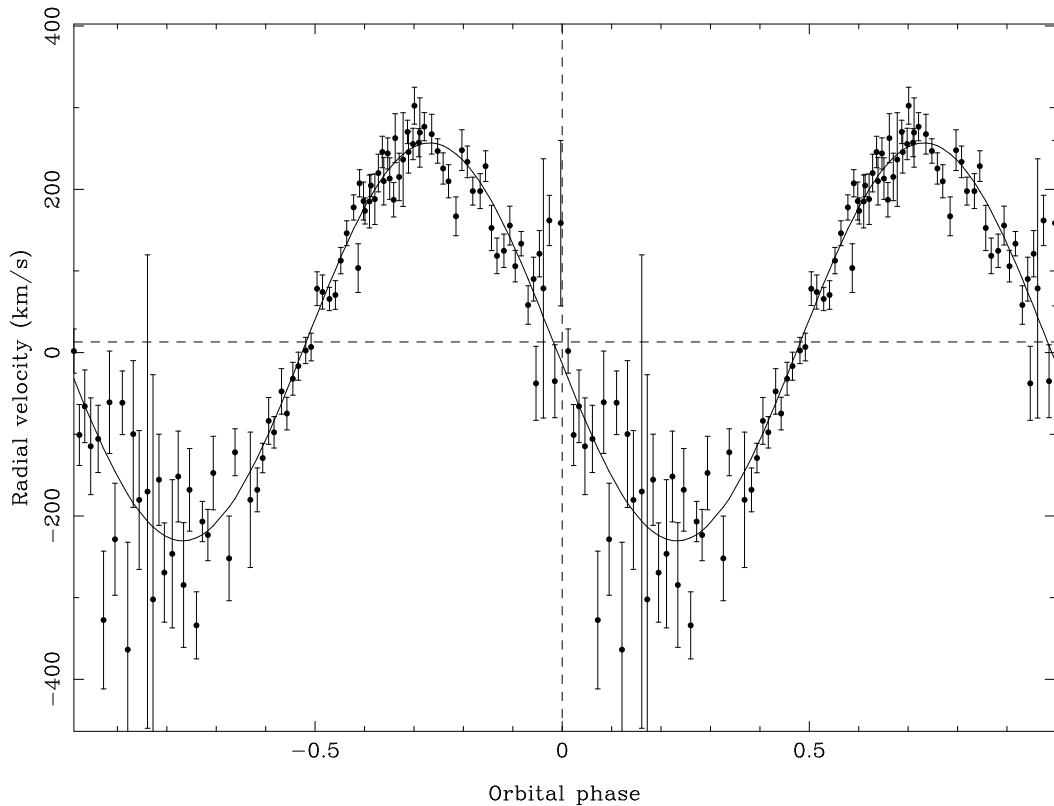


Figure 2.6: Radial-velocity curve of He II $\lambda 4686\text{\AA}$ measured using a double-Gaussian fit with a separation of 900 km s^{-1} . The data have been folded for clarity. The horizontal dashed line represents the systemic velocity.

$$v = \gamma - K \sin[2\pi(\phi - \phi_0)], \quad (2.1)$$

where γ is the systemic velocity, K is the trial radial velocity semi-amplitude of the white dwarf, ϕ is the orbital phase and ϕ_0 is the offset between phase zero and the phase at which the radial velocity crosses from red to blue shifted. An example of a radial velocity curve for He II $\lambda 4686\text{\AA}$ for a Gaussian width of 200 km s^{-1} and separation of 900 km s^{-1} is shown in Figure 2.6.

The radial-velocity curves of the Balmer lines are contaminated by absorption from the secondary star and cannot be used as a reliable indicator of the motion of the white dwarf. The radial velocity curve of He II $\lambda 4686\text{\AA}$, on the other hand, has only a negligible phase offset which suggests that it is a good representation of the radial

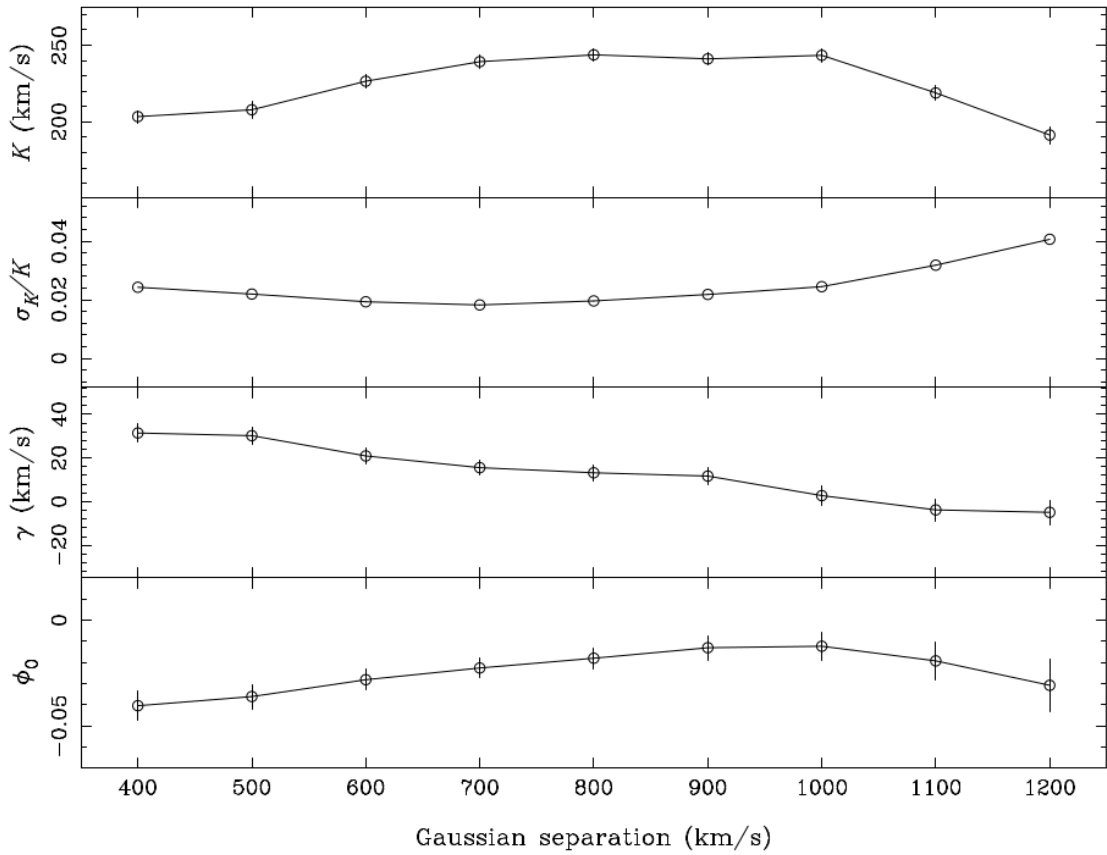


Figure 2.7: Diagnostic diagram for CI Aql based on the double-Gaussian radial-velocity fits to He II $\lambda 4686\text{\AA}$.

velocity of the white dwarf, K_W . In order to determine K_W I plotted a diagnostic diagram (Shafter et al., 1986) – see Figure 2.7. K approaches K_W as ϕ_0 approaches zero, and the point at which the fractional error σ_K/K starts to increase is taken as the optimum Gaussian separation. Figure 2.7 shows that this occurs around a Gaussian separation of 900 km s^{-1} , giving a value of $K_W = 244 \pm 10 \text{ km s}^{-1}$ and $\gamma = 13 \pm 4 \text{ km s}^{-1}$. Since the optimum value of K_W derived from the diagnostic diagram is signal-to-noise dependent, I also constructed a light-centre diagram (Marsh, 1988) – see Figure 2.8. In the co-rotating coordinate frame, the white dwarf has a radial velocity of $(0, -K_W)$, and it can be seen that the largest Gaussian separations are almost coincident with this. Extrapolating the last point to the K_y axis gives a radial velocity for the white dwarf of $K_W = 244 \pm 10 \text{ km s}^{-1}$, in agreement with the result from the diagnostic diagram.

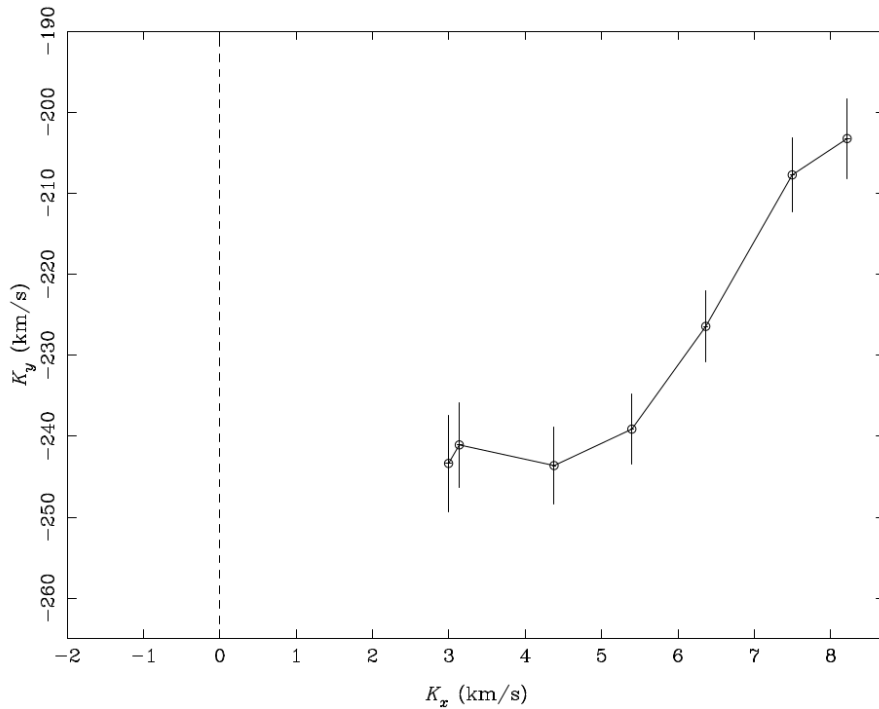


Figure 2.8: Light centre diagram for He II $\lambda 4686\text{\AA}$ in CI Aql. The Gaussian separation of the points increases from right to left.

2.4.6 Radial velocity of the secondary star

The calculation of the radial velocity, K_R , the rotational velocity, $v \sin i$, and the spectral type and luminosity class of the secondary star requires an iterative process. An initial value of K_R is derived by cross-correlation and skew-mapping. To do this, I estimated a pair of initial values of K_R and $v \sin i$ to broaden the spectra to account for the radial and rotational velocities of the secondary. The resulting value of K_R is applied to the optimal subtraction technique, as described in Section 2.4.7, which gives a revised value of $v \sin i$. This is then substituted back into the cross-correlation and the process is repeated until the values of K_R and $v \sin i$ converge.

I performed iterations using the majority of the templates (I omitted some of the later-type templates when it became clear that the spectral type is quite early - see Section 2.4.7). The secondary star in CI Aql is best observed via the absorption lines seen in the trailed spectra of Figure 2.3. I compared regions of the spectrum rich in absorption lines with the template stars, from which I had removed their radial

velocities. I normalised each template spectrum by dividing by its mean, and then subtracting a higher-order spline fit to the continuum. This ensures that line strength is preserved along the spectrum. The CI Aql spectra were normalised in the same way. The smearing of the CI Aql spectra due to orbital motion during the exposure was always less than 5 km s^{-1} , which is insignificant compared to the rotational velocity, so no correction was required. The template spectra were broadened by the rotational velocity of the secondary, $v \sin i$ (see Section 2.4.7). Regions of the spectrum devoid of emission and contaminating absorption features e.g. interstellar medium (ISM), were then cross-correlated with each of the templates, yielding a time series of cross-correlation functions (CCFs) for each template star. I measured the position of the peak of each CCF using a parabolic approximation to three points around the maximum, and then fitted a sine curve to the resulting peaks. The lowest reduced χ^2 (3.78) was found with an F8IV template in the red and the resulting radial-velocity curve is shown in Figure 2.9. This gives $\gamma = 42 \pm 3 \text{ km s}^{-1}$ and $K_R = 111 \pm 4 \text{ km s}^{-1}$. Other templates give values lying in the range $K_R = 106 - 115 \text{ km s}^{-1}$ in the red, and $K_R = 96 - 100 \text{ km s}^{-1}$ in the blue, with no clear trend with spectral type. The systemic velocity, γ , measured from the secondary star is slightly higher than that derived indirectly from the white dwarf via the He II diagnostic diagram (see Section 2.4.5); this may be due to systematic errors or evidence for a weak outflow in the He II emitting region at the disc centre.

Due to noise in the individual CCFs, the radial velocity curves, such as the one shown in Figure 2.9, are rather noisy and the derived value of K_R may be improved using the technique of skew mapping (see Smith et al. 1998 for details).

To produce skew maps, the CCFs were back-projected in the same way as time-resolved spectra in standard Doppler tomography (Marsh & Horne, 1988). If there is a detectable secondary star, we expect a peak at $(0, K_R)$ in the skew map. This can be repeated for each of the templates. Figure 2.10 shows a red skew map produced by cross-correlating with an F8IV template star, together with the trailed CCFs. The peak of this skew map, which gave the strongest peak, gives a value of $K_R = 105 \pm 5 \text{ km s}^{-1}$,

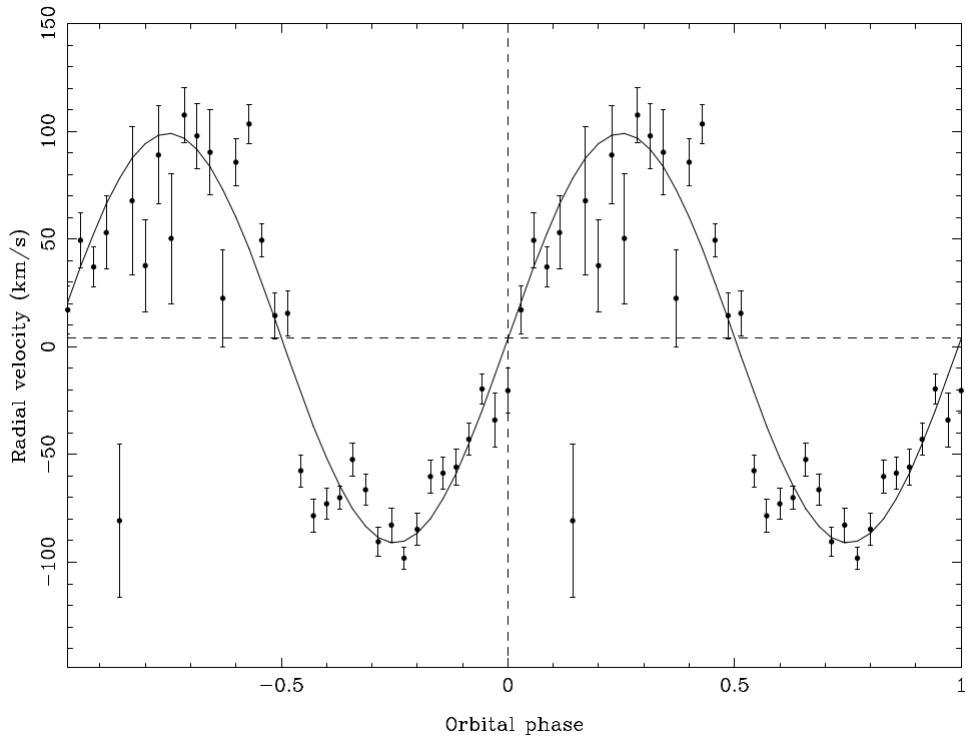


Figure 2.9: Radial-velocity curve of the secondary star in CI Aql, computed from the cross-correlation functions of the red spectra with an F8IV template.

consistent with the radial-velocity curve technique described above. Other templates give peak values lying in the range $K_R = 103 - 109 \text{ km s}^{-1}$, with no clear trend with spectral type. Taking into account all of the uncertainties in the two techniques, I therefore adopt a value of $K_R = 105 \pm 10 \text{ km s}^{-1}$.

The Doppler maps in Figure 2.5 suggest that there is irradiation of the inner face of the secondary star by the accretion regions. This could affect the distribution of the absorption-line flux which would in turn skew the measured value of K_R from its true value (the radial velocity of the centre of mass of the secondary star). It is possible to correct K_R by modelling the distribution of absorption-line flux and comparing the resulting absorption-line light curves and radial-velocity curves with the observed data (see Thoroughgood et al. 2004 for an example). Unfortunately, the radial-velocity curve presented in Figure 2.9 is too noisy to distinguish a non-sinusoid caused by irradiation. The noise in the radial velocity curve dominates the errors in the mass determination compared to the likely shift due to irradiation. To double check this, I computed

the absorption line flux as a function of orbital phase using optimal subtraction (see Section 2.4.7). The resulting light curve was extremely noisy and showed no evidence of variable absorption at phase 0.5, further supporting my conclusion that correcting my observations for irradiation is not appropriate.

2.4.7 Rotational velocity and spectral type of secondary star

Using the value of K_R derived in Section 2.4.6, I corrected the CI Aql spectra for orbital motion and then averaged them. I rotationally broadened the spectral-type templates by a range of velocities (50 – 200 km s⁻¹), using a linear limb-darkening coefficient of 0.5, and then performed optimal subtraction (Marsh et al. 1994). This technique subtracts a constant times the normalised template spectrum from the normalised, average CI Aql spectrum, adjusting the constant to minimise the scatter in the residuals. The scatter is computed from the reduced χ^2 between the residual spectrum and a smoothed version of itself, avoiding regions of emission or contaminating absorption. By finding the value of rotational broadening that minimises reduced χ^2 , I obtain an estimate of both $v \sin i$ and the spectral type of the secondary star. There should, strictly speaking, be a small correction due to the intrinsic rotational velocity of the template star, but as the templates are late-type stars they are assumed to be sufficiently old to have lost most of their angular momentum by magnetic braking and to have very small values of $v \sin i$ (of the order of 1 km s⁻¹; Gray 1992).

Figure 2.11 shows the results of the optimal subtraction technique in the blue and red for a representative sample of the template stars. The minimum of the lowest curve gives both the value of $v \sin i$ and the spectral type of the secondary. Encouragingly, the two wavelength ranges and the different templates all give very similar minima, ranging from $v \sin i = 151 - 164$ km s⁻¹, with no clear trend with spectral type. In the blue the best fitting template is an F8IV star with $v \sin i = 160$ km s⁻¹, whilst in the red it is a G4IV star with $v \sin i = 159$ km s⁻¹, although the F8IV is almost equally preferred in the red with a value of $v \sin i = 157$ km s⁻¹. I therefore adopt the

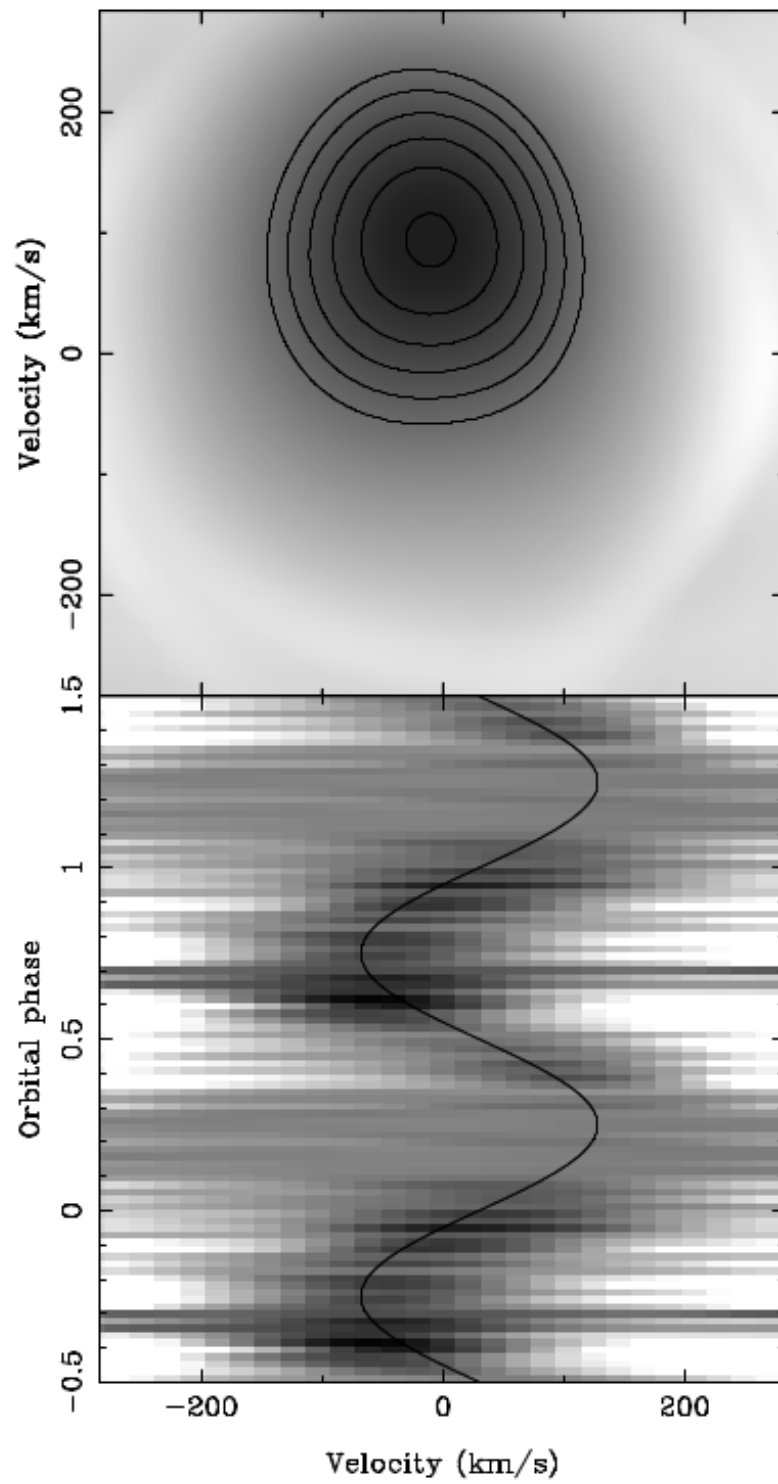


Figure 2.10: Skew map (top) and trailed CCFs (bottom) of CI Aql, computed in the red with an F8IV template.

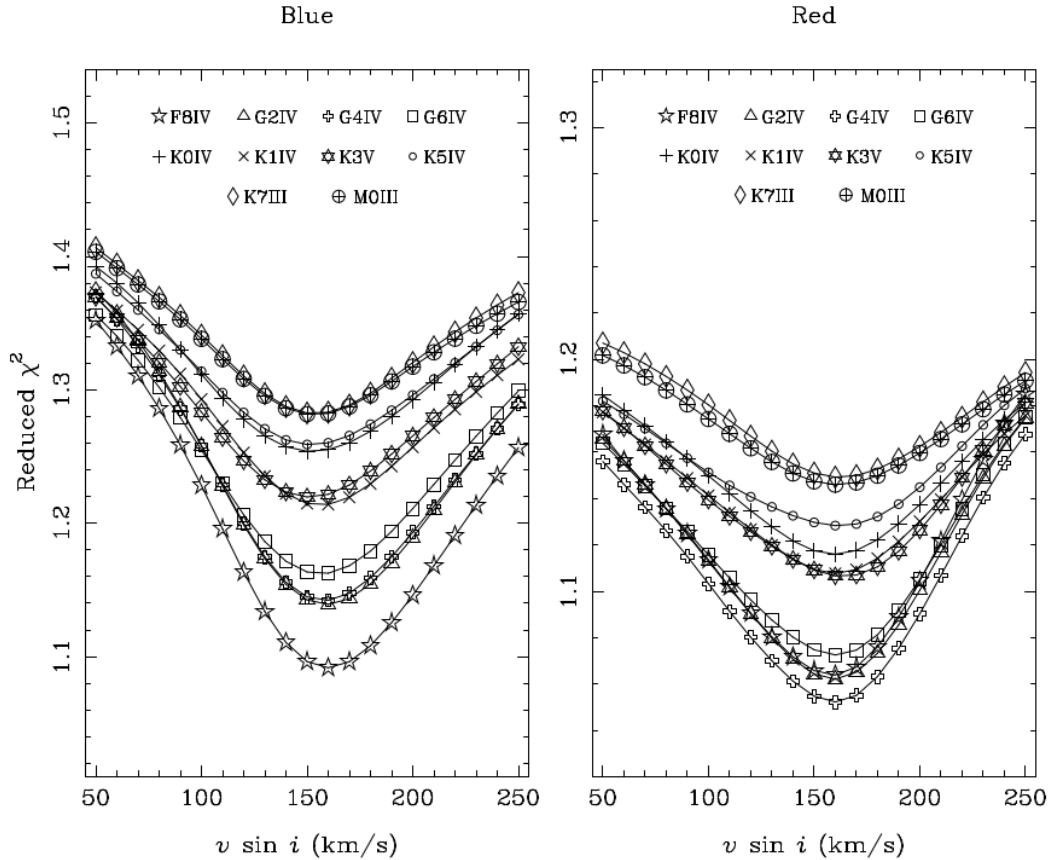


Figure 2.11: Reduced χ^2 from the optimal subtraction technique plotted against $v \sin i$ for a range of templates in the blue and red wavelength ranges.

F8IV as the best-fitting template for my subsequent analysis and select a final value of $v \sin i = 158 \pm 7 \text{ km s}^{-1}$.

The mass and radius of the secondary star are derived in Section 2.4.9 using a Monte Carlo analysis. The results are consistent to within the error bars with those of a slightly-evolved A0 star according to the values published by Gray (1992). The presence of the Mg Ib, Ca I and Fe I absorption features also helps to constrain the spectral type of the secondary star, as these features disappear in stars earlier than A0 (see Pickles 1998). My optimal subtraction analysis shows that the secondary star is no later than F8. It is regrettable that we did not take spectra of templates earlier than F8, which would have allowed me to constrain the spectral type more tightly.

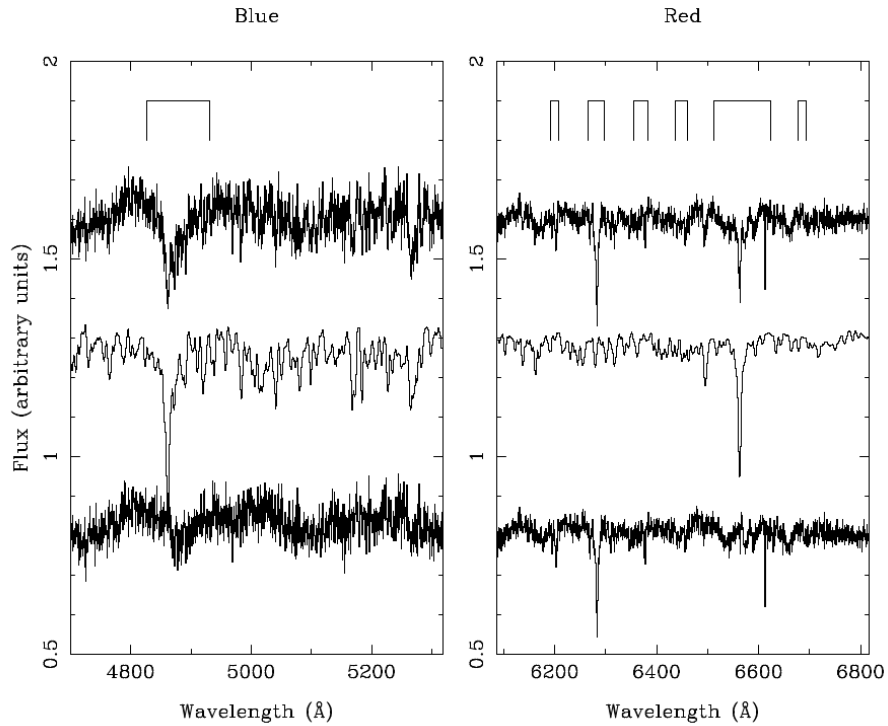


Figure 2.12: Orbitally-corrected spectra of CI Aql (top), the best-fitting F8IV template (middle) and the residuals after optimal subtraction (bottom). The brackets above the plots indicate the regions excluded from the optimal subtraction because they contain strong Balmer and ISM absorption features.

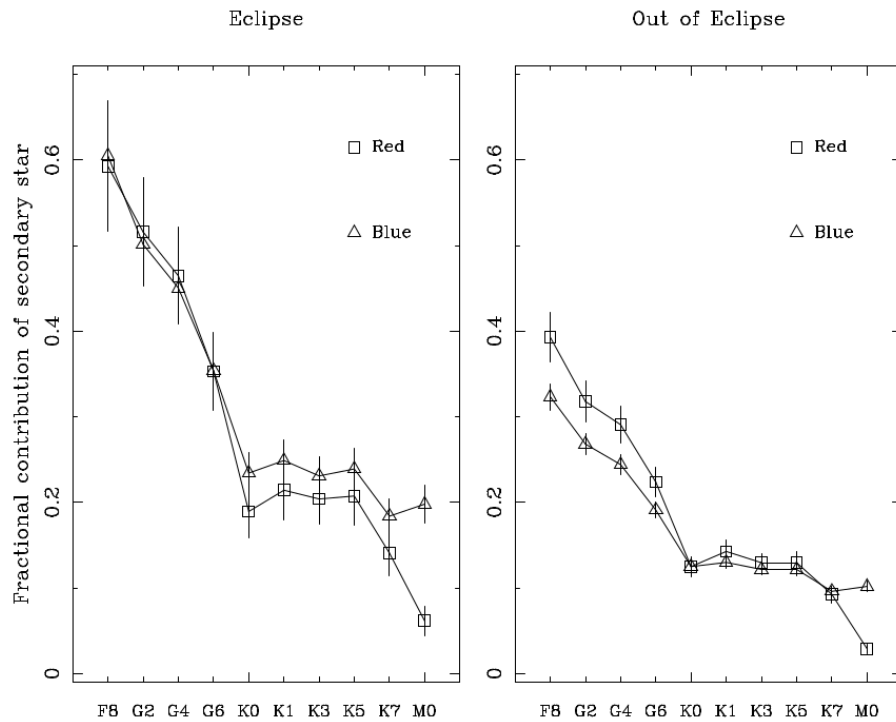


Figure 2.13: The fractional contribution of the secondary star to the total light in eclipse (left-hand panel) and out of eclipse (right-hand panel) in the red wavelength range (squares) and blue wavelength range (triangles).

2.4.8 Distance to CI Aql

As noted above, we did not take spectra of templates earlier than F8, which constrains my calculation of the distance since I can only place a lower limit using my best-fitting template (F8IV).

Figure 2.12 shows the best-fitting template (F8IV), subtracted from the orbitally-corrected average spectrum of CI Aql. Some structure remains in the residuals probably due to the lack of an early enough template spectrum. The optimal subtraction technique also returns the value of the constant by which the template spectra must be multiplied which, for normalised spectra, is the fractional contribution of the secondary star to the total light. The results are plotted in Figure 2.13, measured from the average CI Aql eclipse and non-eclipse spectra.

By finding the apparent magnitude of the secondary star from its contribution to the total light during eclipse, and estimating its absolute magnitude, I can calculate the distance to CI Aql. The apparent magnitude can be found from the light curves (see Figure 2.1), by assuming that the red wavelength range is equivalent to the Johnson R-band and the blue range is equivalent to the V-band. At mid-eclipse, the flux in the red wavelength range is 1.4 ± 0.1 mJy, giving an apparent magnitude of $m_R = 15.8 \pm 0.1$, whilst in the blue, the flux is 0.55 ± 0.05 mJy, giving $m_V = 17.1 \pm 0.1$. In the red wavelength range the secondary star contributes 59% and in the blue it contributes 61%. This gives us approximate apparent magnitudes of $m_R = 16.4 \pm 0.1$ and $m_V = 17.6 \pm 0.1$ for the secondary star. Using the absolute magnitude of an F8IV star of $M_V = 2.4$ (see Gray & Corbally 2009), the distance can be calculated with the distance modulus equation:

$$5 \log(d/10) = m_V - M_V - A_V, \quad (2.2)$$

where d is the distance to the star, and A_V is the extinction in the V-band. The extinction to CI Aql was calculated by Lynch et al. (2004) to be $A_V = 4.6 \pm 0.5$ using

the intrinsic flux ratios of the Ly β -fluoresced OI lines. I find a distance with this method of $d = 1.3 \pm 0.2$ kpc.

The distance can also be estimated using the Barnes-Evans relation (Barnes & Evans 1976):

$$F_\nu = 4.2207 - 0.1V_0 - 0.5\log\phi = 3.977 - 0.429(V - R)_0, \quad (2.3)$$

where V_0 and $(V - R)_0$ are the unreddened V magnitude and $V - R$ colour of the secondary star, and $\phi = 2R_2/d$ is the stellar angular diameter in milliarcseconds. I used a value of $(V - R)_0 = 0.37$ for an F8V star from Ducati et al. (2001), noting that luminosity class makes negligible difference. Using my measured value of $R_2 = 2.07 \pm 0.06 R_\odot$ (see Section 2.4.9), I find a distance of 1.2 ± 0.1 kpc.

My distances are lower than other published estimates for CI Aql. Lynch et al. (2004) measured the distance to be 2.6 ± 0.3 kpc, using the relationship between the time taken to drop two magnitudes, t_2 , and the absolute visual peak magnitude, M_V , of the 2000 outburst. Hachisu et al. (2003) used theoretical models to derive a distance of 1.55 kpc. The distance was calculated by Iijima (2012) as 2.1 – 2.7 kpc, depending on the assumed value of the maximum luminosity of the 2000 outburst and using the extinction $A_V = 4.6 \pm 0.5$ presented by Lynch et al. (2004). It should be stressed however, that my distance estimates are almost certainly lower limits as the spectral type of the secondary star is likely to be earlier than F8, in which case M_V and $(V - R)_0$ decrease, thereby increasing the distance measurement.

The distance to CI Aql in the recent Gaia DR2 is given as $2.8^{+0.4}_{-0.5}$ kpc. Using my value of $m_V = 17.6 \pm 0.1$ and reddening of $A_V = 4.6 \pm 0.5$ gives an absolute magnitude of 0.5. This equates to a spectral type of the secondary of A1IV, or A0V.

2.4.9 System parameters

My measurements of the radial velocities of the white dwarf and secondary star, $K_W = 244 \pm 10$ km s $^{-1}$, $K_R = 105 \pm 10$ km s $^{-1}$, and the rotational broadening, $v \sin i =$

$158 \pm 7 \text{ km s}^{-1}$, can now be used in conjunction with the period, P , and my measurement of the eclipse full-width at half-depth, $\Delta\phi_{1/2} = 0.09 \pm 0.01$ (an average value measured from the blue and red continuum light curves shown in Figure 2.1), to determine accurate system parameters for CI Aql. Only four of these five measurements are needed to calculate the system parameters. However, ignoring the error bars, I obtain different results for the system parameters depending on which set of four measurements are used. Hence, I have opted for a Monte Carlo approach similar to that of Horne et al. (1993). For a given set of values of K_R , $v \sin i$, $\Delta\phi_{1/2}$ and P , the other system parameters are calculated as follows. R_2/a can be estimated because the secondary star fills its Roche lobe; R_2 is the equatorial radius of the secondary star and a is the binary separation. R_2 is approximately given by the volume-equivalent radius of the secondary star's Roche lobe, R_V , which is given by

$$\frac{R_2}{a} \approx \frac{R_V}{a} = \frac{0.49q^{2/3}}{0.6q^{2/3} + \ln(1 + q^{1/2})}, \quad (2.4)$$

where $q = M_2/M_1$ (Eggleton 1983; recalling from Section 1.5.1 that M_1 is the mass of the white dwarf and M_2 is the mass of the secondary). This expression is accurate to better than 1% and is close to the equatorial radius of the secondary star as seen during eclipse. The secondary star rotates synchronously with the orbital motion, so I can combine K_R and $v \sin i$ to get

$$\frac{R_2}{a}(1 + q) = \frac{v \sin i}{K_R}. \quad (2.5)$$

This gives two simultaneous equations so I can calculate the mass ratio q and R_2/a . The orbital inclination, i , is uniquely determined by q and $\Delta\phi_{1/2}$. I determine the inclination using a Roche lobe simulation similar to that of Horne et al. (1982), which differs by $\sim 1\%$ from the value derived using a simple geometric relation for the point eclipse by a spherical body (see, for example, Dhillon et al. 1992). Newton's derivation

of Kepler's Third Law gives us

$$\frac{K_R^3 P}{2\pi G} = \frac{M_1 \sin^3 i}{(1+q)^2}, \quad (2.6)$$

which, with the values of q and i calculated above, gives the mass of the primary star. The mass of the secondary star can then be obtained using the mass ratio q . The radius of the secondary star, R_2 , is obtained from the equation

$$v \sin i = \frac{2\pi R_2 \sin i}{P}, \quad (2.7)$$

and a is calculated from Equation (2.5) with q and i now known.

The Monte Carlo simulation takes 30,000 sample values of K_R , $v \sin i$ and $\Delta\phi_{1/2}$, treating each as being normally distributed about their measured values with standard deviations equal to the errors on the measurements. I treat the period, P , as a constant since it has been measured to a far higher degree of accuracy. I then calculate M_1 , M_2 , i , R_2 , and a , as outlined above, rejecting any $(K_R, v \sin i, \Delta\phi_{1/2})$ triplets which give $\sin i$ greater than 1. Each solution is also subject to rejection if the calculated value of K_W is inconsistent with my measured value of $K_W = 244 \pm 10 \text{ km s}^{-1}$ derived in Section 2.4.5. The probability of rejection is determined in accordance with a Gaussian probability law, i.e. if the calculated value of K_W exactly equals my measured value then it is 100% certain to be accepted, if it lies within 1σ of my measured value of K_W (with σ equal to my measured error on K_W), the probability of rejection is 68 per cent, at 2σ it is 95 per cent, etc.

Each accepted M_1, M_2 pair is then plotted as a point in Figure 2.14, and the masses and their errors are computed from the mean and standard deviation of the distribution of points. The solid curves in Figure 2.14 satisfy the white dwarf radial-velocity constraint, $K_W = 244 \pm 10 \text{ km s}^{-1}$ and the secondary star radial velocity constraint, $K_R = 105 \pm 10 \text{ km s}^{-1}$. I find that $M_1 = 1.00 \pm 0.14 M_\odot$ and $M_2 = 2.32 \pm 0.19 M_\odot$. The full results of the Monte Carlo simulations are shown in Table 2.3. Note that

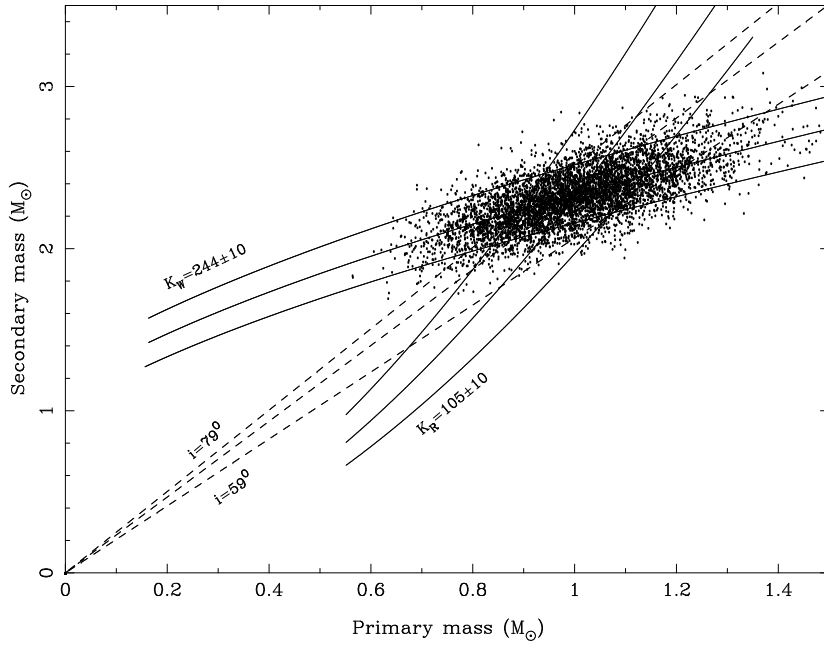


Figure 2.14: Results of the Monte Carlo system parameter determination for CI Aql. Each dot represents an (M_1, M_2) pair. The dashed lines show constant inclinations of $i = 59^\circ, 69^\circ, 79^\circ$. The solid curves satisfy the observed constraints on $K_W = 244 \pm 10 \text{ km s}^{-1}$ and $K_R = 105 \pm 10 \text{ km s}^{-1}$.

computing the system parameters without the K_W constraint gives very similar results and a derived value of $K_W = 246 \pm 10 \text{ km s}^{-1}$, giving confidence that the assumptions and techniques detailed in Section 2.4.5 are valid.

I also estimated the radius of the accretion disc using the half-width of the top of the eclipse (i.e. timing the first and last contacts of eclipse and dividing by 2), $\Delta\phi$, measured from the continuum light curves (Figure 2.1) and the light curves given by Schaefer (2011). The radius of the disc is given by

$$R_D = a \sin i(2\pi\Delta\phi) - R_C, \quad (2.8)$$

Table 2.3: System parameters for CI Aql and their associated statistical errors.

Parameter	Measured value	Monte Carlo value
γ (km s ⁻¹)	42 ± 3	
K_W (km s ⁻¹)	244 ± 10	244 ± 7
K_R (km s ⁻¹)	105 ± 10	
$v \sin i$ (km s ⁻¹)	158 ± 7	
$\Delta\phi_{1/2}$	0.09 ± 0.01	
P (days)	0.6183634(3)	
i (°)		69 ± 2
M_1 (M_\odot)		1.00 ± 0.14
M_2 (M_\odot)		2.32 ± 0.19
q		2.35 ± 0.24
R_2 (R_\odot)		2.07 ± 0.06
a (R_\odot)		4.56 ± 0.14
R_D (R_{L1})		0.45 ± 0.10
Distance - Gaia DR2 (kpc)	2.8 ^{+0.4} _{-0.5}	

where R_C is the half-chord on the secondary, given by

$$R_C = a \sqrt{\left[\left(\frac{R_2}{a} \right)^2 - \cos^2 i \right]}. \quad (2.9)$$

Using my measured value of $\Delta\phi = 0.08 \pm 0.02$, and q and i derived above, I calculate the disc radius $R_D = 0.45 \pm 0.10 R_{L1}$, where R_{L1} is the distance from the WD to the inner Lagrangian point.

One of the assumptions that I have made in the above calculations is that the measured $\Delta\phi_{1/2}$ corresponds to the phases when the Roche lobe of the secondary star eclipses the centre of the disc, i.e. that $-\frac{\Delta\phi_{1/2}}{2}$ and $+\frac{\Delta\phi_{1/2}}{2}$ represent the start and end of the eclipse of the centre of the disc. I can verify that the centre of the accretion disc is indeed eclipsed in CI Aql as follows. Assuming an axisymmetric brightness distribution on the accretion disc, which seems reasonable given the lack of evidence for a bright spot, if the flux from the white dwarf/disc component drops by more than half at mid eclipse then the centre of the disc must be eclipsed. From Figure 2.1 we can see that the blue out-of-eclipse average flux is approximately 0.92 mJy, whereas the minimum flux during eclipse is approximately 0.56 mJy. My measured value of

the contribution of the secondary out of eclipse from Figure 2.13 is 32% and in eclipse it is 61%. Therefore the flux from the white dwarf/disc component out of eclipse is 0.63 mJy whereas in eclipse the flux reduces to 0.22 mJy. Hence the flux from the white dwarf/disc component reduces by 65% during eclipse, thereby demonstrating that the centre of the disc is indeed eclipsed. I also need to verify that the eclipse of the disc centre commences at phase $-\frac{\Delta\phi_{1/2}}{2}$ and ends at phase $+\frac{\Delta\phi_{1/2}}{2}$, i.e. that the brightness profile of the disc, the curved limb of the secondary star and the uneclipsed portions of the disc do not skew my measurement of $\Delta\phi_{1/2}$. I therefore ran a series of light-curve simulations using the CI Aql system parameters, where a Roche lobe eclipses a disc with a range of different radii and axisymmetric brightness profiles. I found negligible variation in the value of $\Delta\phi_{1/2}$ measured from these simulated light curves. For clarity, I should stress that the error on i quoted in Table 2.3 is purely statistical, derived from the mean and standard deviation of the output from the Monte Carlo simulation, and hence does not include the effect of any systematic errors introduced by, for example, the assumption of an axisymmetric disc brightness distribution.

My measurement of the inclination compares well with the value of $i = 71^\circ$ found by Lederle & Kimeswenger (2003), who used a 3D model of CI Aql to fit its light curve. Their slightly higher inclination is most likely due to the use of a smaller assumed mass, and hence radius, of the secondary in CI Aql.

2.5 Discussion

There are two prerequisites for an RN, a high-mass white dwarf and a high mass-transfer rate (\dot{M} ; Anupama 2008). I have found that CI Aql does indeed have a relatively high mass white dwarf ($M_1 = 1.00 \pm 0.14 M_\odot$). Hachisu et al. (2003) calculated the \dot{M} of CI Aql by estimating the mass ejected during the 2000 outburst. Assuming that there were no other outbursts since 1917, their model showed the rate to be $\dot{M} = 1 \times 10^{-7} M_\odot \text{ yr}^{-1}$. If there was another outburst in 1947, as suggested by Schaefer (2001), then the rate increases to $\dot{M} = 1.3 \times 10^{-7} M_\odot \text{ yr}^{-1}$. Both these

values are much higher than the average mass-transfer rates in CVs, which are of order $10^{-8} - 10^{-9} M_{\odot} \text{ yr}^{-1}$ (see Knigge et al. 2011 for a review).

Mass transfer can be driven by either angular momentum loss or the evolution of the secondary. The models of Langer et al. (2000), Han & Podsiadlowki (2004) and Hachisu et al. (2008a) suggest that, in systems with the parameters of CI Aql, it is the evolution of the secondary that is the key contributor to the high \dot{M} . In these models, the evolutionary expansion brings the star into contact with its Roche lobe and, because $M_2 > M_1$, thermal-timescale mass transfer begins and the system exhibits nova outbursts. Eventually, the nuclear evolution of the star causes it to expand further, thereby increasing the mass-transfer rate, which leads to steady hydrogen burning on the surface of the white dwarf. Such systems are supersoft X-ray sources (Shen & Bildsten, 2007). The white dwarf mass grows considerably during this phase, ultimately exploding as a SNIa.

The zero-age main-sequence radius of a $2.3 M_{\odot}$ star is $1.8 R_{\odot}$ and increases to my observed value of $2.07 R_{\odot}$ after approximately 300 Myr, according to the models of Langer et al. (2000). This suggests that the secondary star in CI Aql is a core hydrogen burning star that has begun to evolve away from the main sequence towards the giant branch. This expansion has brought it into contact with its Roche lobe, and thermal-timescale mass transfer has recently started.

I note that my measured values for the component star masses of CI Aql, when plotted on Figure 1 of Hachisu et al. (2008b), places it in the region of a MS + WD binary system that will evolve to produce a SNIa (see Figure 2.15).

An approximate estimate of the time until the system explodes as a SNIa can be found using the models of Langer et al. (2000), which suggest that CI Aql will explode as a SNIa in less than 10 Myr. Similarly, Ivanova & Taam (2004) developed numerical models of the evolution of binaries consisting of evolved MS stars and high mass WD companions, that are undergoing thermal-timescale mass transfer. Their models show the parameters of WD+MS binaries that produce SNIa and are consistent with those of Hachisu et al. (2008a). Figure 2.16, taken from Ivanova & Taam (2004), shows

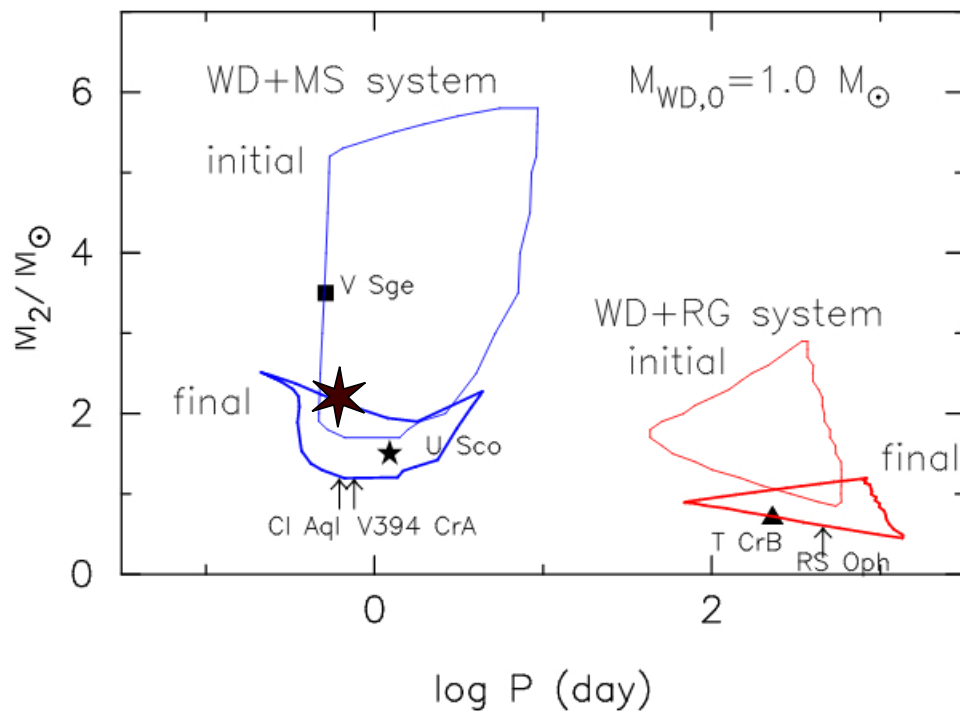


Figure 2.15: The regions that produce SNe Ia are plotted in the $\log P$ – M_2 (orbital period – secondary mass) plane for the (WD+MS) system (left) and the (WD+RG) system (right). Currently known positions of the recurrent novae and super-soft X-ray sources are indicated by a five-pointed star for U Sco, a triangle for T CrB, a square for V Sge, and by arrows for the other three recurrent novae, V394 CrA, CI Aql, and RS Oph. Two sub-classes of the recurrent novae, the U Sco type and the RS Oph type, correspond to the WD + MS channel and the WD + RG channel of SNe Ia, respectively. The six-pointed star indicates the location of CI Aql using my results. Figure taken from Hachisu et al. (2008b)

the evolutionary fates of binary systems that begin mass transfer with various initial WD and secondary star masses. The parameters of CI Aql place it in the region that produces SNIa.

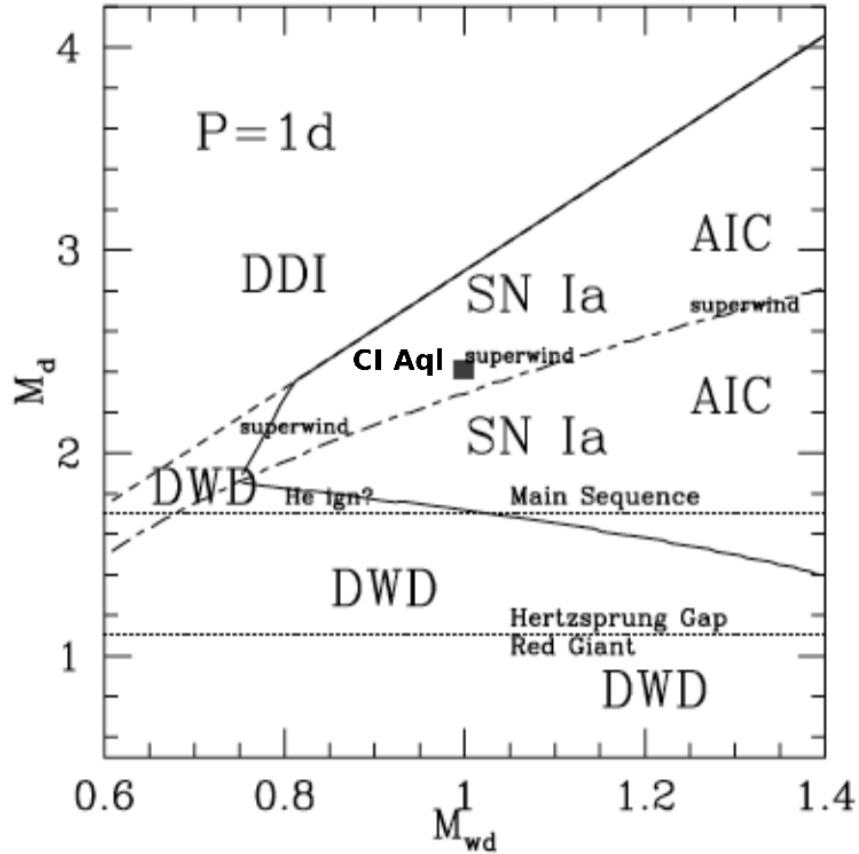


Figure 2.16: Possible evolutionary fates of systems characterised by secondary donors of initial mass M_d and WDs of initial mass M_{wd} in units of M_{\odot} for an orbital period of 1 day based on a semi-analytical models. The solid curve delineates the area where the white dwarf can accrete sufficient mass for near Chandrasekhar mass models of SNIa and AIC models of neutron star formation. The dashed curve represents the condition of the occurrence of a DDI. Double WD systems are formed at locations marked DWD. For reference, donors which undergo mass transfer above the upper dotted line lie close to the main sequence, those below are in the Hertzsprung gap, and those below the lower dotted line are red giants. Above the short dashed - long dashed line the mass transfer leads to the development of a superwind from the WD. The location of CI Aql, using my measured parameters, is indicated by the small box. Figure taken from Ivanova & Taam (2004)

In a very recent paper, Hachisu & Kato (2018) propose that CI Aql is not a SNIa progenitor. They argue that there is not enough time for sufficient matter to transfer from the secondary onto the WD before the mass of the secondary drops below that

of the WD and the mass ratio is reversed. At this point, the thermal timescale mass transfer will cease and hence they argue that CI Aql is not a SNIa progenitor. However, at this point the usual angular momentum processes will continue to drive mass transfer and so the system may well ultimately become a SNIa.

In the following Chapters, I will describe my two campaigns to search for nova shells around CVs, and report on my findings, including the first ever detection of a nova shell around a novalike. I will also discuss what my results tell us about the evolution of CVs.

Chapter 3

Searching for nova shells around cataclysmic variables

The contents of this chapter have been published in Monthly Notices of the Royal Astronomical Society, in a manuscript entitled ‘*Searching for nova shells around cataclysmic variables*’ by Sahman, Dhillon, Knigge and Marsh (Sahman et al., 2015). The WHT images were taken by Vik Dhillon and Tom Marsh and the images were reduced by Vik Dhillon. The IPHAS images were downloaded from the IPHAS catalogue DR2. The analysis of all the images and the following text are my own work.

3.1 Introduction

As I discussed in Section 1.7, the discovery of nova shells around novalikes would support the nova-induced cycle theory. Hence we embarked on a campaign to search for nova shells using the Auxiliary Port¹ on the WHT. The targets we selected are listed in Section 3.2.1.

The choices of telescope aperture and field of view for this project were dictated by the expected brightness and radii of the nova shells around CVs. Recombination theory tells us that the $H\alpha$ luminosity per unit volume of a nova shell is proportional

¹http://www.ing.iac.es/astronomy/observing/manuals/html_manuals/wht_instr/pfip/prime3_www.html

to density squared, and hence the total luminosity of the shell is inversely proportional to volume. If we assume that the shell expands at a constant velocity, then its volume increases as the cube of time. Therefore, the luminosity is inversely proportional to time cubed, and the surface brightness decreases as time to the fifth power. This expectation has been empirically confirmed by Downes et al. (2001) who found that the H α surface brightness of nova shells diminishes as $t^{-4.8}$, although novae with strong shock interactions between the ejecta and any pre-existing circumstellar material, e.g. GK Per (Shara et al. 2012) and T Pyx (Shara et al. 1989), do not fit this relationship.

To estimate how bright the shells around NLs might be, we used as a guide the archetypal old nova DQ Her (Nova Her 1934) which has a clearly visible shell (Slavin et al., 1995). Its shell had a brightness of ~ 20 mags/arcsec $^{-2}$ and a radius of 8 arcsec in 1994, 60 yr after its nova eruption. Assuming that nova shells fade as $t^{-4.8}$ (Downes et al., 2001) then after 120 yr after outburst it will fade to ~ 24 mags/arcsec $^{-2}$, by which time its radius will have doubled to 16 arcsec, and at 180 yr after outburst it will fade to ~ 26 mags/arcsec $^{-2}$, and its radius will have increased to 24 arcsec. We can use these estimates to determine our observing strategy and to establish the instrumental set-up that is required. NLs have apparent magnitudes of ~ 15 , on average. Novae brighten by ~ 10 mag during eruption, implying that most NLs when in outburst would have been just visible to the naked eye. Given the much increased rate of nova detection in the last 100 yr, it is unlikely that such eruptions would have been missed if they had occurred within the last ~ 100 yr or so. We thus expect to be able to detect shells around NLs which are at least 100 yr old; any which erupted more recently than this would likely have been detected and the systems would now be classified as old novae. Assuming the shell of DQ Her is representative, a 100-yr old shell would be at least 16 arcsec in radius and no brighter than ~ 26 mags/arcsec $^{-2}$. Hence to detect such shells we require deep images with a relatively modest field of view, which led us to choose the Auxiliary Port on the WHT.

To estimate the age of the faintest shell we might detect with this set-up, we simulated the images we would obtain from a spherical nova shell in an 1800 s H α exposure.

We simulated images with brightnesses of 24–26 mags/arcsec⁻². The simulated images are shown in Figure 3.1.

The simulation showed that a shell with luminosity comparable to the shell of DQ Her would become too faint to detect in an image at ~ 180 yr after outburst. For approximately circular shells that are centred on the binary, this detection threshold can be pushed fainter by computing the mean radial profile of the central object and inspecting the wings for evidence of a shell (Gill & O’Brien 1998). The DQ Her shell would be apparent in the radial profile up to 220 yr after outburst. Assuming DQ Her is representative, this means that we would be able to detect shells around NLs from nova eruptions up to a maximum of ~ 220 yr ago and $\sim 1'$ in diameter using our proposed set-up on the WHT.

In support of our WHT observations, we also examined known CVs in the 2.5m Isaac Newton Telescope (INT) Photometric H α Survey of the Northern Galactic Plane (IPHAS) – see Section 3.2.2.

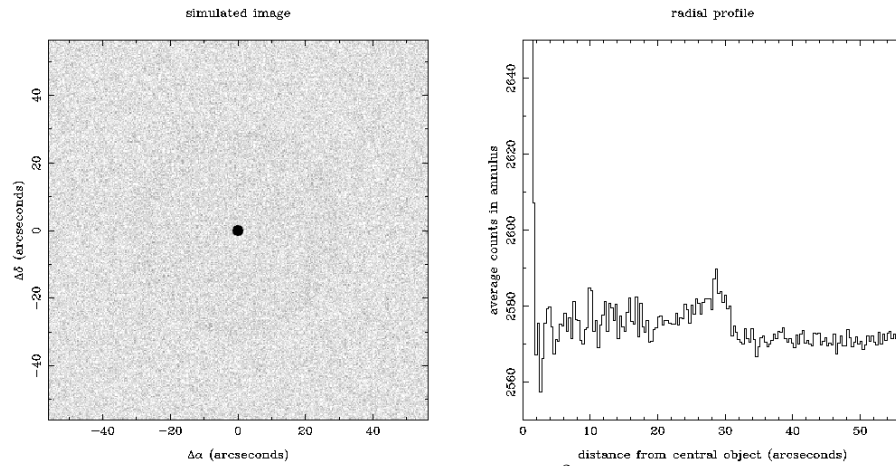
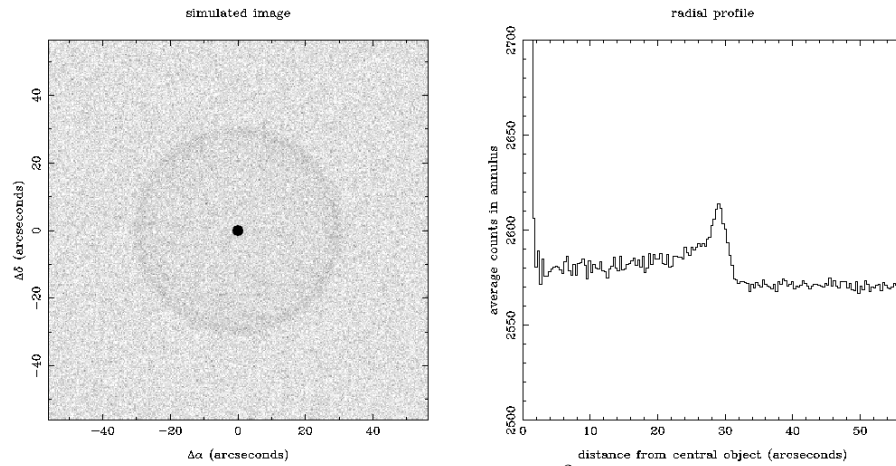
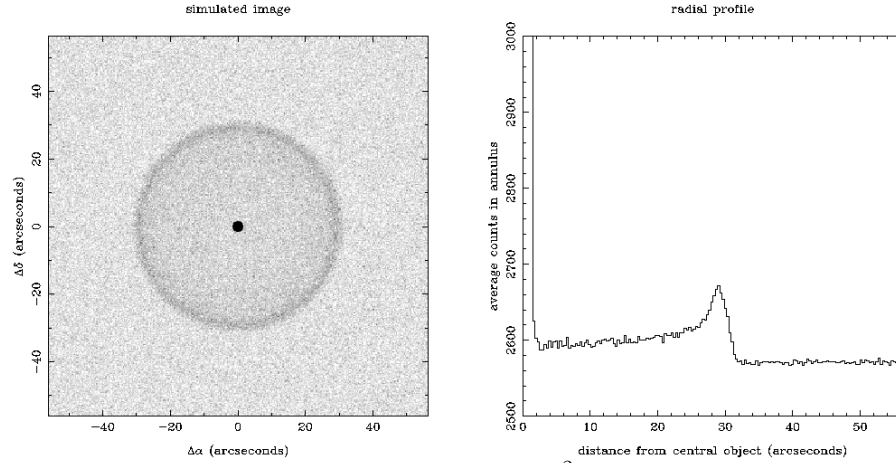


Figure 3.1: Simulated WHT auxiliary-port images. The images are of 1800 seconds each, taken in the light of H α (50 \AA bandpass) in 1'' seeing and grey moon, with a TEK chip binned by 3 in each direction (giving 0.33 arcsec/pixel). In each image, the nova shell is of radius 30'' (and has an intrinsic width of 3'') and the central object has a magnitude of 15. The images have peak shell surface-brightnesses of 24 mags/arcsec² (upper image), 25 mags/arcsec² (central image) and 26 mags/arcsec² (lower image). In all images, pixels plotted in black have at least 3000 counts and pixels in white have less than 2500 counts.

3.2 Observations

3.2.1 WHT Images

The observations were taken on the nights of 1997 October 24–26. We used the 1024×1024 pixels TEK5 CCD chip mounted on the Auxiliary Port at the Cassegrain focus of the WHT to image the fields around our target NLs. This setup gave a platescale of 0.11'' per pixel and hence a field size of 113''× 113''. H α is one of the strongest features in the spectra of nova shells, with typical velocity widths of up to 2000 km s⁻¹ (e.g. Pagnotta & Schaefer 2014). In order to maximise the detection of light from the shell and minimise the contribution of sky, we used a narrow-band (55Å FWHM = 2500 km s⁻¹) interference filter centred on the rest wavelength of H α (ING filter number 61²). Note that this filter also includes a contribution from [NII] 6584Å emission, which may dominate the spectra of nova shells with strong shock interaction of the ejecta with any pre-existing circumstellar medium, e.g. T Pyx (Shara et al., 1989).

As we were planning to compare the radial profiles of the (generally brighter) target stars with field stars (see Section 3.4.1), we had to ensure that we did not saturate the target stars. Hence the CCD chip was used unbinned and in quick readout mode in order to decrease dead-time, at the expense of a negligible decrease in signal-to-noise (thanks to the fact that our observations were always sky-limited). The observing conditions were excellent throughout the run; the sky was always photometric, there was no evidence of dust and the seeing was usually sub-arcsecond, with occasional excursions up to 1.5–2''.

To ensure we only targeted relatively well-studied systems with reliable CV classifications, we made our selection from the RK catalogue. We selected a total of 31 CVs, predominantly NLs, and searched for nova shells around them. To test our setup we included three systems with known nova shells: BT Mon, DQ Her and GK Per.

²<http://catserver.ing.iac.es/filter/>

We also took the opportunity to observe two asynchronous polars, which are CVs with magnetic WDs in which the spin period of the WD is not synchronised with the orbital period (Campbell & Schwobe, 1999). The asynchronicity is believed to be due to a recent nova event, as shown by the polar V1500 Cyg which had a nova eruption in 1975 (Stockman et al., 1988). The ejection of material from the WD carries away angular momentum which slows down the rotation of the WD. The two asynchronous polars we observed with the WHT were V1432 Aql and BY Cam. We also included three other non-NL systems, PQ Gem, which is an intermediate polar, IP Peg which is a DN, and AY Psc which is a Z Cam-type DN, which were favourably positioned during our observing run.

A full list of the 31 objects observed with the WHT and a journal of observations is given in Table 3.2. In summary, the targets comprised 3 old novae with known shells, 1 old nova without a known shell (V Per), 2 asynchronous polars, 1 intermediate polar, 22 NLs, and 2 DNe.

3.2.2 IPHAS images

IPHAS was a 1800 deg² survey of the northern Milky Way spanning the galactic latitude range $-5^\circ < b < +5^\circ$ and galactic longitude range $29^\circ < l < 215^\circ$. Three filters were used, H α , Sloan r' and Sloan i' , reaching down to $r' \approx 20$ (10σ). The survey took place between 2003 and 2008, and used the INT Wide Field Camera (WFC) which offers a pixel scale of 0.33'' per pixel and a field of view of $\sim 34' \times 34'$. Exposure times were initially set at 120 s (H α) and 10 s (r' and i') but evaluation of the early data led to an increase in the r' -band exposure time to 30 s – for full details of the observations and data reduction see Drew et al. (2005) and Barentsen et al. (2014).

We made our target selection as follows. We cross-matched the RK catalogue to the IPHAS footprint. There were 74 matches of CVs with the classification N, NL or DN (indicating nova, nova-like variable and dwarf nova, respectively). Each matching IPHAS field was reviewed visually to determine whether any H α nebulosity

Table 3.1: Journal of WHT observations. The classifications of the CVs are taken from the RK catalogue. All shells detected in our WHT observations are shown in bold. The RK catalogue classifications for novae are N, Na, Nb. *We detected a shell around V1315 Aql with the INT, not the WHT. †This system is a NL.

Object	Classification	Orbital period (hrs)	Date	UTC start	UTC end	Number of exposures	Total exposure time (secs)	Visible shell?
PX And	NL SW NS SH	3.51	25/10/97	00:06	01:11	2	3600	N
UU Aqr	NL UX SW SH	3.93	25/10/97	22:42	23:46	3	3300	N
HL Aqr	NL UX SW	3.25	27/10/97	00:13	00:54	2	2400	N
V794 Aql	NL VY	3.68	26/10/97	21:17	21:58	2	2400	N
V1315 Aql	NL UX SW	3.35	26/10/97	19:32	20:15	4	2400	N*
V1432 Aql	NL AM AS	3.37	25/10/97	19:59	21:01	2	3600	N
WX Ari	NL UX SW	3.34	25/10/97	02:42	03:44	2	3600	N
KR Aur	NL VY NS	3.91	26/10/97	03:50	04:10	1	1200	N
V363 Aur	NL UX SW	7.71	25/10/97	05:09	06:10	2	3600	N
BY Cam	NL AM AS	3.36	25/10/97	04:00	05:01	2	3600	N
AC Cnc	NL UX SW	7.21	27/10/97	03:31	04:12	2	2400	N
V425 Cas	NL VY	3.59	24/10/97	22:29	22:37	2	200	N
V751 Cyg	†VY SW? NS SS	3.47	24/10/97	22:07	22:27	1	1200	N
V1776 Cyg	NL UX SW	3.95	25/10/97	21:31	22:32	2	3600	N
CM Del	NL UX VY?	3.89	26/10/97	20:22	21:05	4	2400	N
PQ Gem	NL IP	5.19	27/10/97	02:41	03:22	2	2400	N
DQ Her	Na DQ	4.65	25/10/97	19:31	19:51	1	1200	Y
BH Lyn	NL SW SH NS	3.74	26/10/97	04:24	05:05	2	2400	N
BP Lyn	NL UX SW	3.67	27/10/97	04:21	05:02	2	2400	N
BT Mon	Na SW	8.01	26/10/97	06:12	06:43	2	1800	Y
BT Mon	Na SW	8.01	27/10/97	06:02	06:32	1	1800	Y

Continued on next page

Table 3.2 (Continued): Continued from previous page. Journal of WHT observations. The classifications of the CVs are taken from the RK catalogue. All shells detected in our WHT observations are shown in bold and discussed in Chapter 4. The RK catalogue classifications for novae are N, Na, Nb.

Object	Classification	Orbital period (hrs)	Date	UTC start	UTC end	Number of exposures	Total exposure time (secs)	Visible shell?
V1193 Ori	NL UX SW?	3.96	26/10/97	01:05	02:38	3	5400	N
IP Peg	DN UG	3.80	25/10/97	21:08	21:19	1	621	N
LQ Peg	NL VY SH NS	3.22	26/10/97	22:37	23:18	2	2400	N
V Per	Na NL SW?	2.57	27/10/97	01:06	01:48	2	2400	N
GK Per	Na DN IP	47.92	25/10/97	06:14	06:34	1	1200	Y
AY Psc	DN ZC NS	5.21	25/10/97	23:51	00:53	2	3600	N
VY Scl	NL VY	3.98	24/10/97	23:22	00:03	2	2400	N
VZ Scl	NL VY SW	3.47	24/10/97	22:47	23:39	2	3000	N
SW Sex	NL UX SW	3.24	26/10/97	05:15	05:56	2	2400	N
RW Tri	NL UX SW	5.57	25/10/97	01:29	02:30	2	3600	N
DW UMa	NL SW SH NS	3.28	27/10/97	05:09	05:50	2	2400	N

was apparent around the target CVs. Due to the significant H α nebulosity in the Galactic plane, we did not attempt to compute radial profiles for the IPHAS targets (see Section 3.4.1). The 74 systems we examined in IPHAS are listed in Table 3.4. The targets comprised 2 asynchronous polars, 10 polars and intermediate polars, 5 NLs, 34 DNe, 3 old novae with known shells and 20 old novae without known shells. Three of the NLs, V1315 Aql, V363 Aur and V751 Cyg, were also part of our WHT sample (see Table 3.2), as was BT Mon, an old nova with a known shell.

Table 3.4: List of CVs examined in the IPHAS database. The classifications of the CVs have been taken from the RK catalogue. Note that the RK catalogue classifications for novae are N, Na, Nb. All shells detected in IPHAS are shown in bold and are discussed in Sect. 3.2. *We confirmed the detection of a shell around V1315 Aql with additional INT observations – see Section 3.4.2. †This system is a NL (Patterson et al. 2001). ‡Whilst these objects are shown as possible Z Cam systems in the RK catalogue, Simonsen et al. (2014) found that they do not exhibit the standstills necessary for this classification and that they are actually normal DNe.

Object	Classification	Orbital period (hrs)	Visible shell?	Object	Classification	Orbital period (hrs)	Visible shell?
CI Aql	Nr	14.83	N	V2468 Cyg	Na	3.49	N
KX Aql	DN SU	1.45	N	V2491 Cyg	Na	2.56	N
V368 Aql	Na	16.57	N	V446 Her	Na DN	4.97	N
V603 Aql	Na SH NS	3.32	N	CP Lac	Na SW?	3.48	N
V1315 Aql	NL UX SW	3.35	Y*	DI Lac	Na	13.05	N
V1425 Aql	Na NL? IP?	6.14	N	BT Mon	Na SW	8.01	Y
V1493 Aql	Na	3.74	N	CW Mon	DN UP IP?	4.24	N
V1494 Aql	Na	3.23	N	V902 Mon	NL IP	8.16	N
FS Aur	DN UG IP PW?	1.43	N	V959 Mon	N	7.10	N
HV Aur	DN SU	1.98	N	CZ Ori	DN UG	5.25	N
T Aur	Nb	4.91	Y	V344 Ori	DN ZC [†]	5.62	N
QZ Aur	Na	8.58	N	FO Per	DN UG? ZC? [†]	4.13	N
V363 Aur	NL UX SW	7.71	N	FY Per	NL VY	6.20	N
AF Cam	DN UG	7.78	N	TZ Per	DN ZC	6.31	N
FT Cam	DN SU?	1.80	N	UV Per	DN SU	1.56	N
V705 Cas	Na	5.47	N	V Per	N NL SW?	2.57	N
V709 Cas	NL IP	5.33	N	WY Sge	N DN? SW?	3.69	N
V1033 Cas	NL IP	4.03	N	DO Vul	DN SU	1.38	N
HT Cas	DN SU	1.77	N	QQ Vul	NL AM	3.71	N
KP Cas	DN SU	1.95	N	V405 Vul	DN SU	2.71	N
EM Cyg	DN ZC	6.98	N	V458 Vul	Na	1.64	Y
EY Cyg	DN UG SH?	1.10	N	V498 Vul	DN SU WZ	1.41	N
V337 Cyg	DN SU	1.64	N	GD 552	DN? WZ?	1.71	N

Continued on next page

Table 3.5 (Continued): Continued from previous page. List of CVs examined in the IPHAS database. The classifications of the CVs have been taken from the RK catalogue. Note that the RK catalogue classifications for novae are N, Na, Nb. All shells detected in IPHAS are shown in bold and are discussed in Sect. 3.2. *We confirmed the detection of a shell around V1315 Aql with additional INT observations – see Section 3.4.2. †This system is a NL (Patterson et al. 2001). ‡Whilst these objects are shown as possible Z Cam systems in the RK catalogue, Simonsen et al. (2014) found that they do not exhibit the standstills necessary for this classification and that they are actually normal DNe.

Object	Classification	Orbital period (hrs)	Visible shell?	Object	Classification	Orbital period (hrs)	Visible shell?
V503 Cyg	DN SU NS	1.87	N	Lanning 420	DN SU	1.45	N
V516 Cyg	DN UG	4.11	N	J0130+6221	DN?	3.12	N
V550 Cyg	DN SU	1.62	N	J0345+5335	CV DN?	7.53	N
V751 Cyg	†VY SW? NS SS	3.47	N	J0506+3547	DN SU	1.62	N
V1251 Cyg	DN SU WZ	1.77	N	J0518+2941	NL?	5.72	N
V1316 Cyg	DN SU	1.78	N	J0524+4244	NL AM AS	2.62	N
V1363 Cyg	DN ZC?†	2.42	Y?	J0619+1926	DN SU WZ	1.34	N
V1454 Cyg	DN SU	1.36	N	J1853-0128	NL IP	n/a	N
V1500 Cyg	Na NL AM AS	3.35	Y	J1915+0719	DN SU WZ	1.37	N
V2274 Cyg	Na	7.20	N	J1926+1322	NL IP	4.58	N
V2275 Cyg	Na IP?	7.55	Y?	J1953+1859	DN SU?	1.44	N
V2306 Cyg	NL IP	4.35	N	J2133+5107	NL IP	7.14	N
V2362 Cyg	Na	1.58	N	J2138+5544	NL IP	n/a	N
V2467 Cyg	Na NL IP?	3.83	N	J2250+5731	NL AM	2.90	N

3.3 Data reduction

3.3.1 WHT images

The images were debiased using the median level of the overscan strip and flat-fielded using normalised twilight sky flats. Where multiple images of targets had been taken, these were added to improve the signal-to-noise ratio. Sky subtraction was performed by subtracting the median level determined from two blank sky areas of size 100 x 100 pixels. Each frame suffered from significant vignetting in the corners due to the circular filter holder, which was not fully corrected by the flat field. The corners of each image were hence removed by setting a series of 50 x 50 pixel blocks to a fixed value, so that they appear white in the final images. Pixels affected by cosmic rays were set to the average value of surrounding pixels. All processing was performed using the KAPPA and FIGARO packages in the STARLINK³ suite of programs.

3.3.2 INT IPHAS images

For a full description of the IPHAS data reduction pipeline see Drew et al. (2005) and Barentsen et al. (2014). The frames for our 74 targets were downloaded from the IPHAS catalogue (Data release 2.0). The images were examined visually for the presence of shells using SAOImage DS9. The contrast scale parameters were adjusted to levels just a few percent above the background noise, in order to highlight any faint shells that might be present.

³<http://starlink.jach.hawaii.edu/starlink>

3.4 Results

3.4.1 WHT images and radial profiles

In order to detect shells in the WHT images, I adopted two strategies. First, I visually examined each image to determine if a shell is visible. This technique would reveal wide shells with diameters of more than a few arcseconds. Second, I calculated the radial profile of each CV and compared it to a number of field stars in the same image. Any nebulosity around the CV due to a nova shell would cause the radial profile of the CV to lie above the average profile of the field stars (for example, see the radial profile of BT Mon in Figure 3.3). This technique can reveal shells with diameters of less than a few arcseconds, and was successfully used by Gill & O'Brien (1998) to discover four new nova shells. A key assumption in this technique is that the Point Spread Function (PSF) is uniform across the WHT chip. Figure 3.2 shows the PSFs for five field stars (arrowed) in the image of V Per. The PSFs show identical radial profiles irrespective of field position, giving confidence that the PSFs are uniform across the small Auxiliary Port field of view of the CCD, as expected.

The centroids of the stars were first measured by fitting a two-dimensional Gaussian. The radial profiles were then generated by calculating the radial distance of each pixel from the centroid, and then averaging the fluxes of the pixels falling into bins of increasing radial distance from the centroid. The radial profiles were then normalised to unity, and plotted from the centre of the star until the flux reached 1σ above the mean background flux.

In Appendix A I show the images and radial profiles for all of the objects that were observed with the WHT. As expected, the images for the three old novae with previously known shells (BT Mon, DQ Her, GK Per) clearly show a shell and each is discussed briefly below. There are no visible shells in the images of the remaining objects, nor do any of the radial profiles of the targets show any obvious differences from those of the field stars.

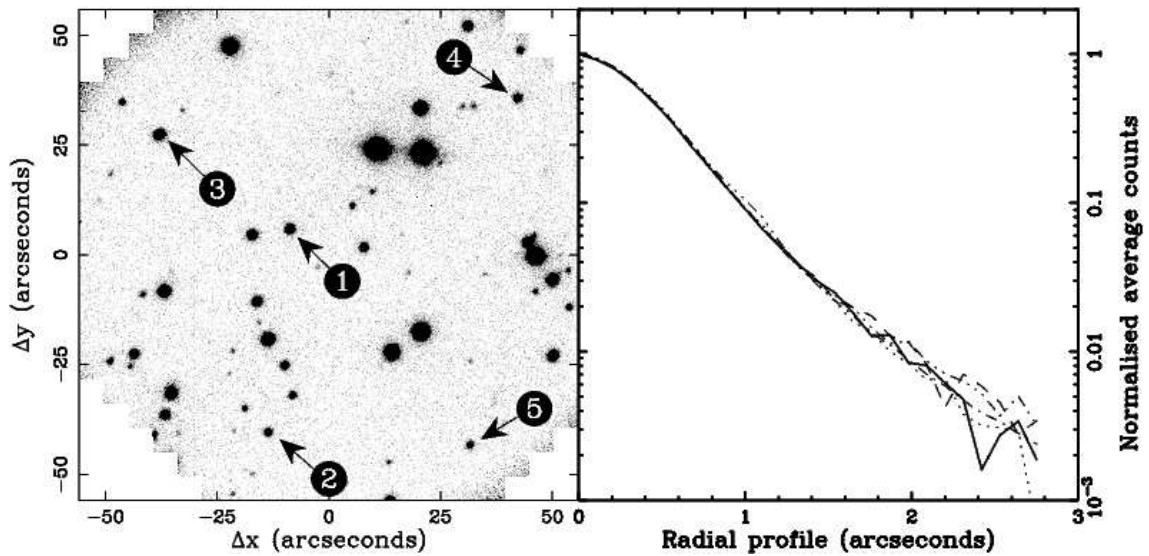


Figure 3.2: Left: WHT image of V Per (Star number 1). Right: PSFs for the five arrowed stars showing the uniformity across the WHT chip. Each numbered star has been plotted as follows 1 - solid line, 2 - dashed, 3 - dot-dashed-dot-dashed, 4 - dotted, 5 - dashed-dot-dot-dot-dashed. The orientation of the image is the same as that shown in Figure 3.3.

In the next paragraphs I will discuss the systems with known nova shells, and some possible detections of new shells.

BT Mon

The shell around BT Mon (Nova Mon 1939) was discovered spectroscopically by Marsh et al. (1983). BT Mon is a high-inclination system and the system parameters were derived by Smith et al. (1998). The first image of the shell was reported by Duerbeck (1987), who found it to be an incomplete clumpy, slightly elliptical ring with approximate dimensions of $11'' \times 9''$ and the major axis pointing in the NW–SE direction.

My image and radial profile of BT Mon is shown in Figure A.3. The lower right quadrant was not used to calculate the radial profile in order to remove the flux from the nearby star. The radial profile of BT Mon clearly deviates from the profile of the field stars, from approximately $4''$ outwards. This is due to the presence of the shell and gives assurance that this technique for identifying shells is valid.

In Figure 3.3 I show an enlarged version of our image of the BT Mon shell. I

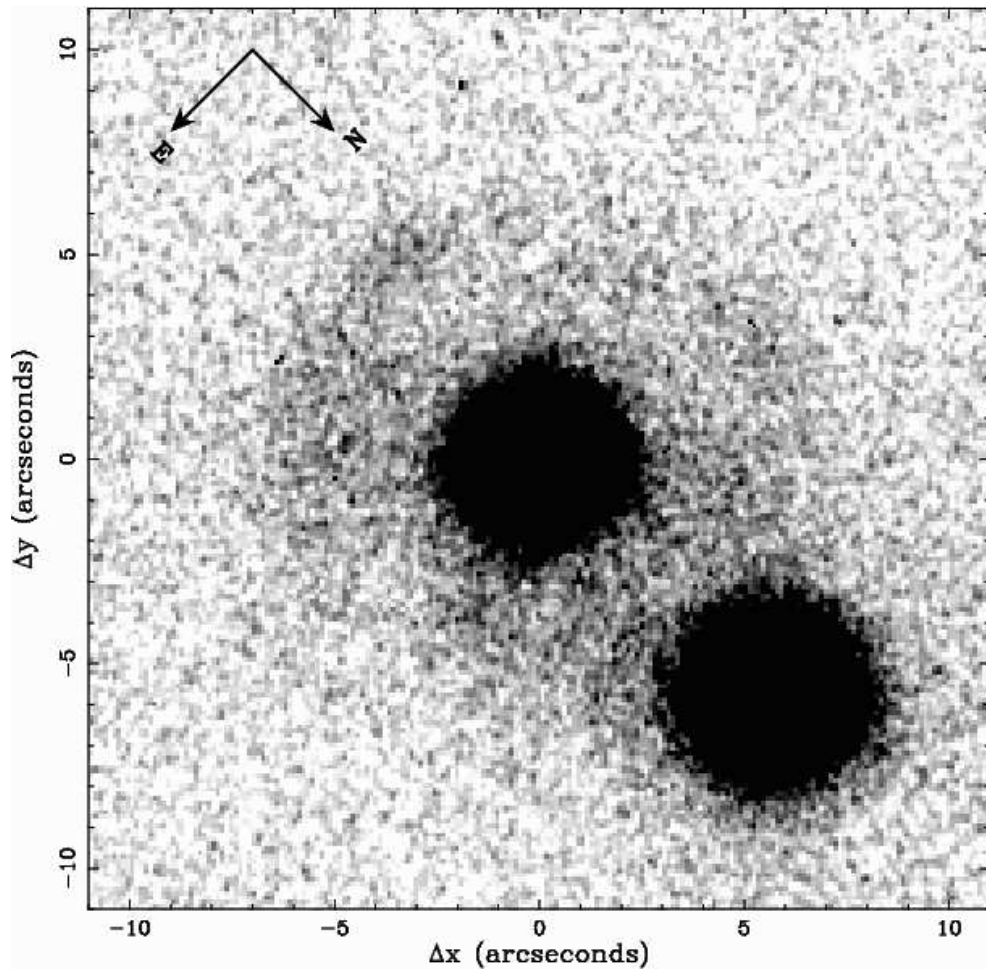


Figure 3.3: Enlarged image of the BT Mon nova shell. Note that the second star to the lower right is an unassociated foreground/background star.

estimate the shell diameter to be $13'' \pm 1''$. Assuming a constant shell expansion velocity of $1800 \pm 300 \text{ km s}^{-1}$ and a distance of $1.8 \pm 0.1 \text{ kpc}$ as derived by Marsh et al. (1983), together with the date of the nova as 1939.7, gives an expected diameter of $12 \pm 3''$ at the time of our observations, in agreement with my measured value.

DQ Her

DQ Her (Nova 1934) is an intermediate polar with system parameters derived by Horne et al. (1993). The nova shell (see Figure A.3) is a prolate ellipsoid with a slightly pinched central ring. Vaytet et al. (2007) used our WHT image of DQ Her to estimate the angular size and hence distance of the system. They measured the angular size of the major and minor axes to be $a = 25.31 \pm 0.44''$ and $b = 18.70 \pm 0.44''$. Assuming a

constant expansion velocity of $370 \pm 14 \text{ km s}^{-1}$, they derived a distance of $d = 525 \pm 28$ pc. This compares favourably with the Gaia DR2 distance of 501 pc.

GK Per

The nova GK Per (1901) is the archetypal nova remnant and has been extensively studied (see Shara et al. 2012 for a review). The shell is boxy in shape, of size approximately $100'' \times 90''$ and exhibits clumpy knots. Recently, Liimets et al. (2012) derived a three dimensional model of the nova shell in GK Per, and determined the proper motion and radial velocities of more than 200 knots in the ejecta. The knots have a wide range of velocities (600–1000 km s^{-1}) and have suffered only modest deceleration. Shara et al. (2012) used HST images from 1995 and 1997 to resolve over 1000 filamentary structures in the ejecta. They also investigated a jet-like feature, first discovered by Anupama & Prabhu (1993), which they suggest could be the shock interaction of a collimated flow with the ISM, probably originating from the accretion disc. The jet extends some $2.7'$ to the NW, which is larger than the field of view of our image. I examined our image of GK Per (see Figure A.3) but could not find any evidence of the jet-like feature on smaller spatial scales, most probably due to the lower signal-to-noise ratio of our image.

3.4.2 IPHAS images

I visually examined the IPHAS images for evidence of nova shells. Table 3.4 lists all the objects we examined, and indicates whether a shell is visible. The short exposure times of the $\text{H}\alpha$ images (120 s) means that only bright, nearby shells are likely to be visible. I found three old novae with shells that are visible in the IPHAS footprint: T Aur (Nova Aurigae 1891), V458 Vul (Nova Vul 2007 No. 1) and V1500 Cyg (Nova Cygni 1975), all of which are well studied systems. I briefly review these objects below. I found no definite detections of shells around any other IPHAS targets with the exception of two systems, V1363 Cyg and V1315 Aql, as discussed below. I did

discover a nebula around V2275 Cyg, which is too large to be associated with its nova event in 2001. This nebula may be a light echo due either to scattering off, or flash ionisation of, a pre-existing nebula. I also discuss this object further below.

T Aur

The IPHAS H α image of T Aur is shown in Figure 3.4a. The shell is clearly discernible in the image, giving us confidence that it is possible to see nova shells in the IPHAS images. The shell structure has been likened to that of DQ Her, although T Aur is some 43 years older (Slavin et al. 1995). The shell is elliptical in shape, with major and minor axes of length $\sim 30'' \times 20''$ respectively.

V458 Vul

The H α image of V458 Vul is shown in Figure 3.4b. The shell has major and minor axes of $\approx 30'' \times 20''$. The image was taken in June 2007, two months before the system underwent a nova explosion in August 2007. The shell is actually a pre-existing planetary nebula ejected some 14,000 years ago (Wesson et al., 2008). The central binary is most likely a post-double common-envelope binary comprised of a WD of mass $\sim 1.0 M_{\odot}$ and a post-AGB secondary of mass $\sim 0.6 M_{\odot}$ (Rodríguez-Gil et al., 2010).

V1500 Cyg

V1500 Cyg (Nova Cygni 1975) is a well-studied nova and is the archetypal asynchronous polar (Wade et al., 1991). The nova shell was first imaged four years after outburst by Becker & Duerbeck (1980), who measured the radius at $\sim 1.0''$. Subsequently, Wade et al. (1991) presented an image taken in 1987 by which time the shell had expanded to $\sim 1.9''$, giving an expansion rate of $0.16''$ per annum, and Slavin et al. (1995) presented an image taken in 1993 showing a nebular radius of $\sim 3''$. The IPHAS H α image taken in 2004 is shown in Figure 3.4c. The nova shell is extremely faint and

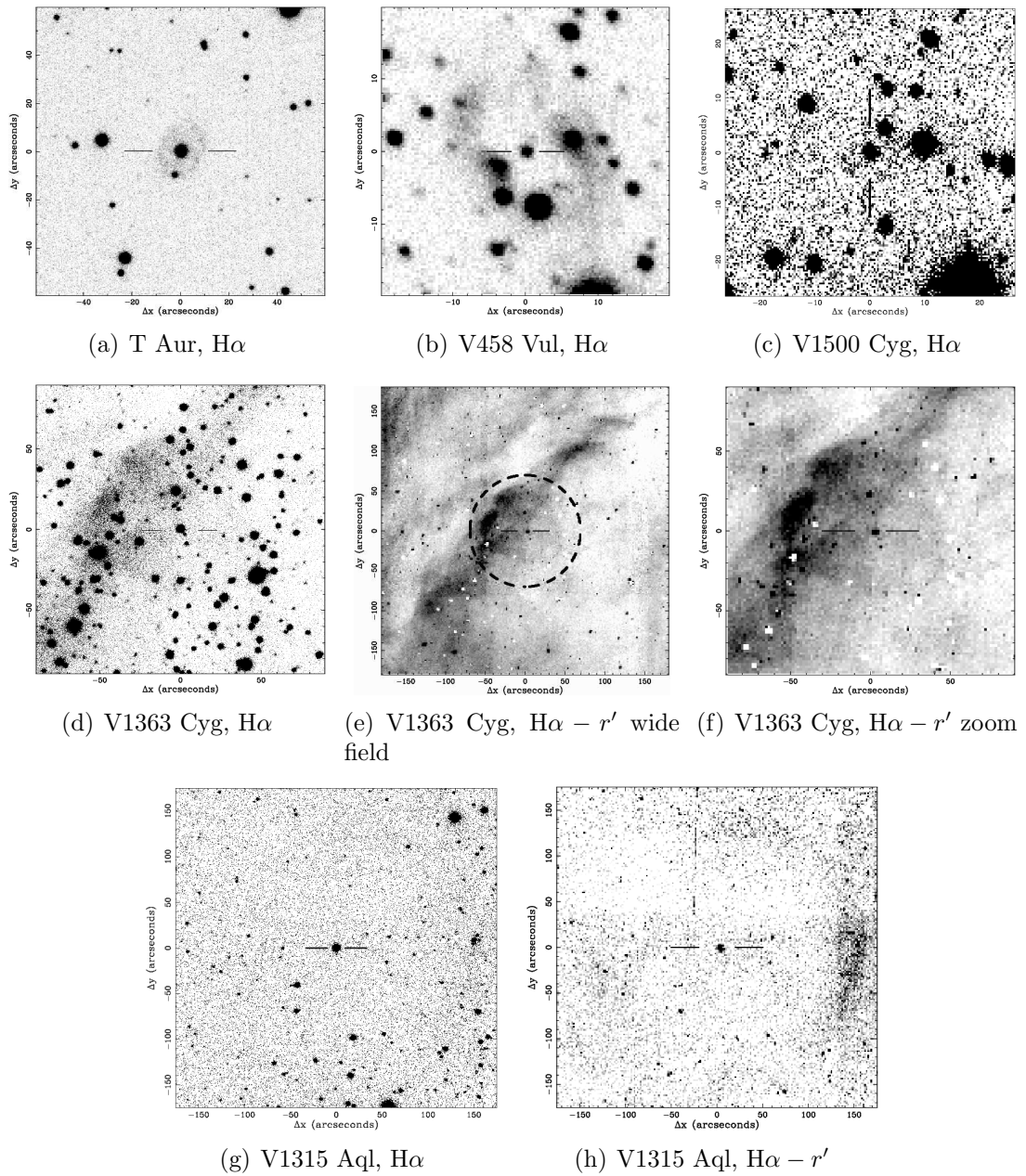


Figure 3.4: IPHAS $H\alpha$ and $H\alpha - r'$ images. In all images, North is up, East is left.

has a radius of $\sim 5''$, still consistent with the nebular expansion rate of $\sim 0.16''$ per annum given by Wade et al. (1991).

V1363 Cyg

In Figure 3.4d I show the IPHAS $H\alpha$ image of the field around the dwarf nova V1363 Cyg. The $H\alpha$ image is heavily populated with field stars making the surrounding nebula difficult to discern. Hence I show the $H\alpha - r'$ image in Figure 3.4e, which effectively removes most of the flux from the field stars. The field is extremely crowded and the object lies close to a ribbon of gas, making the unambiguous detection of a nova shell extremely difficult. However, there is a faint egg-shaped shell of emission of $\approx 2'$ diameter, approximately centred on the CV.

V1315 Aql

Figures 3.4f & 3.4g show the IPHAS $H\alpha$ and $H\alpha - r'$ images of V1315 Aql. There is a faint shell of $\approx 2.5'$ radius approximately centred on the CV, with more pronounced emission towards the West. We also imaged this object with the WHT. However, the small field of view of the WHT image (see Figure A.1) is not large enough to confirm the possible detection of this shell. This object is the subject of Chapter 5 where I describe in detail the imagery and spectra that I obtained and analysed.

V2275 Cyg

The nova eruption of V2275 Cyg (Nova Cygni 2001 No. 2) occurred on 2001 August 19 (Nakamura et al., 2001). The field around V2275 Cyg was observed on five epochs during the IPHAS survey. The five images are shown in Figure 3.5.

In the first three images, taken between November 2003 and November 2006, a nebula of $\approx 2.7'$ diameter is clearly apparent, but it has disappeared in the fourth and fifth images taken in December 2008 and August 2009. Using the expansion velocity and minimum distance derived by Kiss et al. (2002) of approximately 2000 km s^{-1} and 3 kpc respectively, the shell from the 2001 nova event should have been no larger than $0.2'$

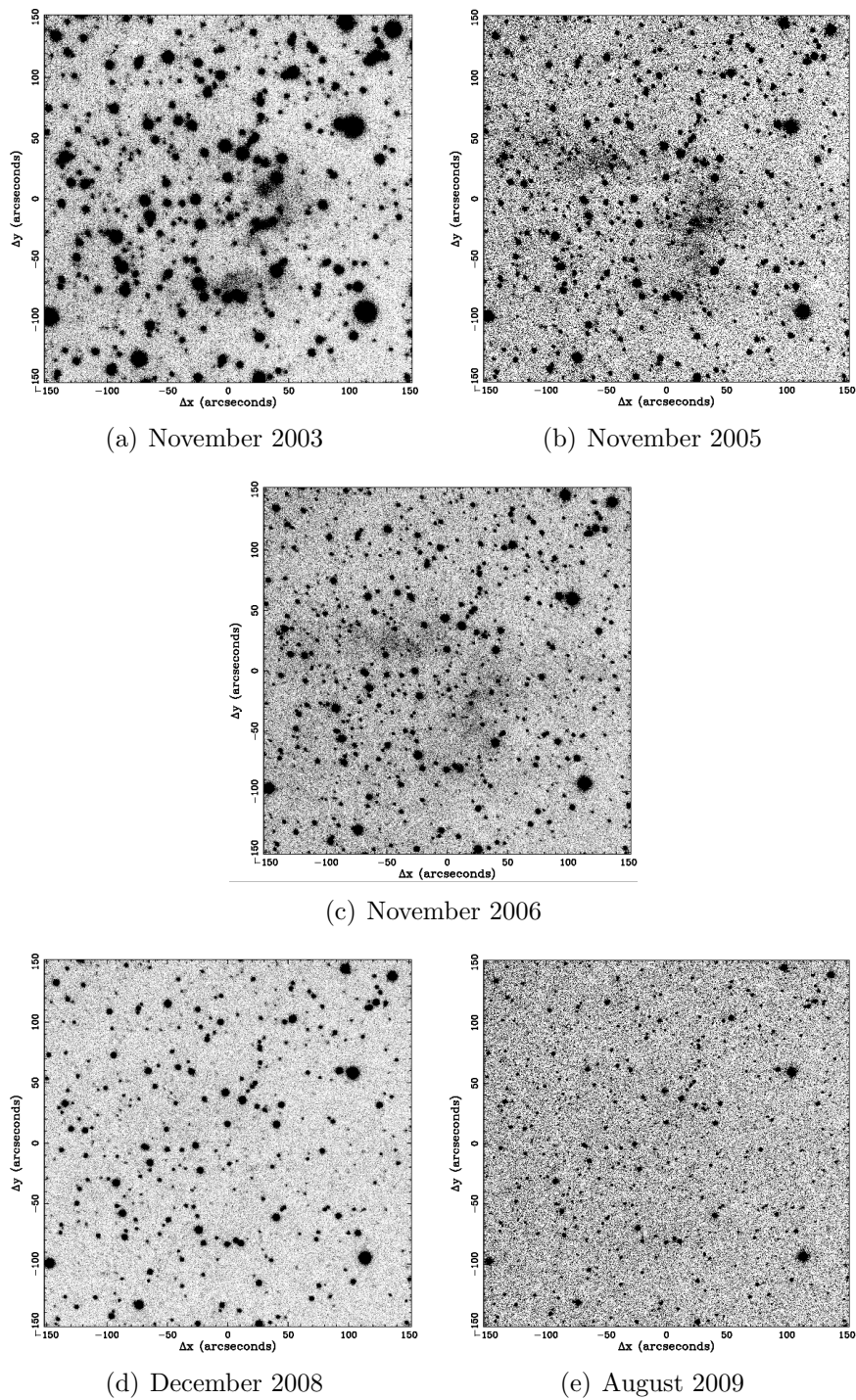


Figure 3.5: H α images of V2275 Cyg from IPHAS. A faint nebula is apparent in images (a)–(c) but is not present in images (d) and (e). In all images, North is up, East is left.

by November 2006, which is the date of the last IPHAS image the nebula was visible in. Hence the nebula in the image can not be from the 2001 nova event. The most obvious explanation is that it is a light echo from material ejected from the system by a previous event, such as a nova shell or a planetary nebula. The angular diameter of the shell on the November 2006 image is $2.7' \pm 0.5'$. Adopting the distance of 4.6 kpc from the Gaia DR2, the radius of the shell is 5.1×10^{16} m. The time from the nova in 2001 to the date of the 2006 IPHAS image is 1901 days giving a light radius of 4.9×10^{16} m. These two radii are broadly comparable, as expected for a light echo. Assuming a typical nova shell expansion velocity of 2000 km s^{-1} , the age of the shell can be estimated to be ~ 300 years. I have reviewed the literature and can find no earlier discussion of a nebula around V2275 Cyg. Harvey (2017) obtained $\text{H}\alpha$ images of the shell using the Aristarchos telescope (the Aristarchos telescope is operated on Helmos Observatory by the Institute for Astronomy, Astrophysics, Space Applications and Remote Sensing of the National Observatory of Athens) and in WISE (Wright et al., 2010) Band 3 and 4 infrared images. He found evidence of a number of concentric cylindrical shells, which implies repeated nova eruptions.

The presence of light echoes around novae are relatively rare, and only GK Per, V732 Sgr, V458 Vul and T Pyx have recorded echoes (Kapteyn 1901, Swope 1940, Wesson et al. 2008, Sokoloski et al. 2013, respectively).

There are three principal blobs of material that are apparent in the images, as highlighted in Figures 3.6 a–c. Blob A does not appear in Figure 3.6(a) but appears in Figures 3.6(b) & 3.6(c). It appears to move southwards (towards the right in the images) by approximately $20''$. At a distance of 4.6 kpc, with an interval of approximately one year between the two images, this equates to a transverse speed of $1.4 \times 10^8 \text{ ms}^{-1}$. Clearly this cannot be bulk motion of material. It is better explained as the passage of a light pulse through a pre-existing bi-polar nebula, with the axis of symmetry of the nebula pointing obliquely to the plane of the sky. This orientation is supported by the lack of eclipses in the light curve of V2275 Cyg (Balman et al. 2005). Blob B appears in all three images and whilst different parts change in brightness, there is no consistent

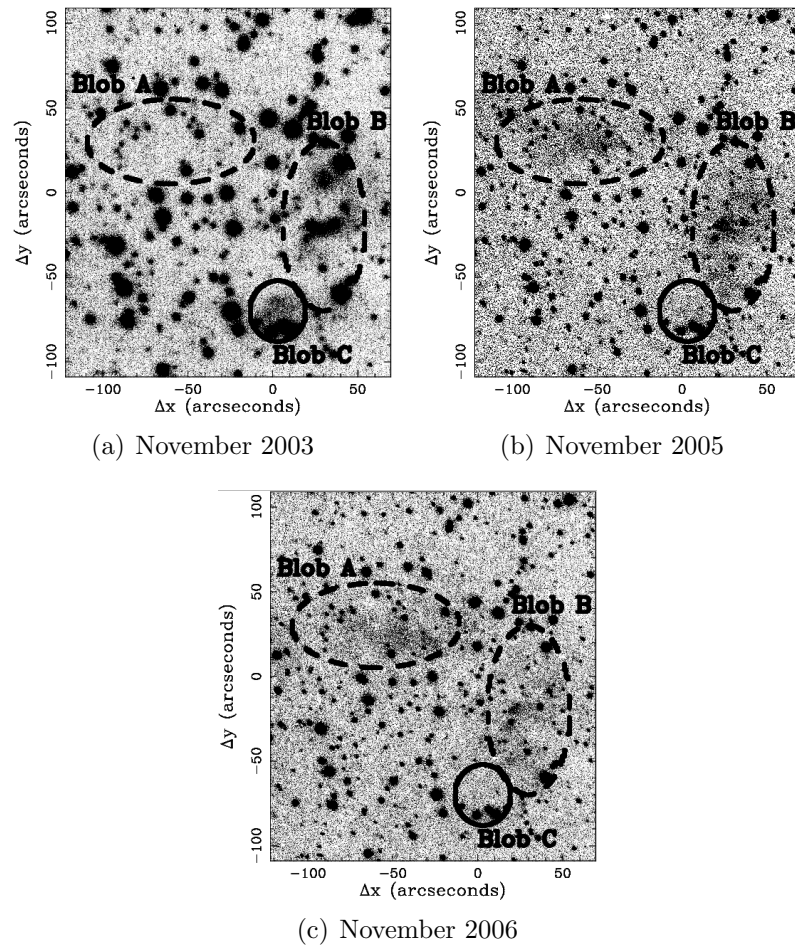


Figure 3.6: $H\alpha$ images of V2275 Cyg from IPHAS. See text for a discussion about the three blobs of material. In all images, North is up, East is left.

motion shown. This blob of material is diagonally opposite blob A and could be the opposite pole of a bi-polar nebula. Blob C only appears in Figure 3.6(a).

If the shell is due to a previous nova event this would mean that V2275 Cyg should be reclassified as a recurrent nova (RN), in agreement with Pagnotta & Schaefer (2014) who identified V2275 Cyg as a likely RN on the basis of its outburst light curve and spectrum.

3.5 Discussion

Our goal was to search for previously undetected nova shells around CVs, primarily novalike variables. The results of our search are shown in Table 3.6.

Table 3.6: Summary of our first search for nova shells.

	Nova-like Variables	Polars & Intermediate Polars	Asynchronous Polars	Dwarf Novae	Old Novae	Total
WHT Targets	22	1	2	2	4	31
IPHAS Targets	5	10	2	34	23	74
less: Duplicated objects	-3	0	0	0	-1	-4
Grand total of systems	24	11	4	36	26	101

3.5.1 Nova-like variables

We examined 22 NLs with the WHT and 5 NLs with IPHAS (three NLs were common to both giving a total of 24 unique NLs), and found no shells with the WHT and evidence for only one shell in IPHAS, V1315 Aql, which we subsequently confirmed with additional INT observations (see Chapter 5). I will discuss the broad conclusions that can be drawn from this nova shell discovery rate in Chapter 4.

3.5.2 Asynchronous polars

The WHT survey included two asynchronous polars, V1432 Aql and BY Cam. The images and radial profiles of these two systems are shown in Appendix A. There are no traces of nebulosity in either the images or the radial profiles of these systems. There are two other asynchronous polars in the IPHAS survey, J0524+4244 and V1500 Cyg, the archetypal asynchronous polar. There is no evidence of a shell around J0524+4244. I did recover the previously known shell around V1500 Cyg, originating from its nova eruption in 1975 (see Section 3.4.2).

These results imply that I am unable to confirm that a recent nova eruption is the cause of the asynchronicity in the white dwarf spin of these systems. However, it is perhaps not surprising that I did not find any new shells given our survey limits and the synchronisation timescale. BY Cam, for example, is estimated to synchronise within ~ 1100 yrs (Campbell & Schwope 1999), an order of magnitude longer than our ~ 100 yr detection window (see Section 3.1).

Subsequent to our campaign, Pagnotta & Zurek (2016) published the results of their search for nova shells around four asynchronous polars and one intermediate polar. Their targets included the two we had observed, but their observations were deeper than ours, taken on the 10m South African Large Telescope. They found no evidence of shells in any of their images.

3.5.3 Future surveys

In hindsight, our decision to use the old nova DQ Her as a guide for our WHT search strategy (see Section 3.2.1) led us to underestimate the optimal field of view for hunting for nova shells. This is because DQ Her has relatively slow ejecta (350 km s^{-1} ; Warner 1995). The angular size of the shell is determined by the time since the nova eruption, the distance to the CV, and the speed of the ejecta, and is given by the following scaling relation:

$$R \sim 20'' \frac{t/100 \text{ yr} \times v/1000 \text{ km s}^{-1}}{d/\text{kpc}}, \quad (3.1)$$

where R is the angular radius of the shell in arcseconds, t is the time elapsed since the nova eruption, v is the shell expansion velocity, and d is the distance to the CV. Hence a recent, distant nova with slow-moving ejecta ($t = 100 \text{ yr}$, $v = 500 \text{ km s}^{-1}$, $d = 2 \text{ kpc}$) would have a small shell of radius $\sim 5''$, whereas an older, nearby nova with fast moving ejecta ($t = 200 \text{ yr}$, $v = 2000 \text{ km s}^{-1}$, $d = 0.5 \text{ kpc}$) would have expanded to a radius of $\sim 2.7'$. Hence the field of view of the Auxiliary port on the WHT ($\sim 1'$ radius) was too small to detect such large shells. This is borne out by the size of the one shell that I did discover around V1315 Aql, which is $\sim 2.5'$ in radius, and the three shells discovered by Shara et al. (2007; 2012; 2017b) of radii $1.5'$ (AT Cnc), $15'$ (Z Cam) and $1.7'$ (Nova Sco 1437). Another problem with having such a small field of view is the paucity of field stars for the radial-profile technique (Section 3.4.1).

The IPHAS survey, on the other hand, had more than enough field of view ($\sim 17'$ radius per pointing) to discover nova shells but suffered from very short exposure times

(120 s), which we had no control over, and from being constrained to the Galactic plane, making it difficult to pick out nova shells from the galactic H α nebulosity. A more optimal survey for nova shells would have approximately the same field of view as an IPHAS pointing, avoid the Galactic plane and be of similar depth to our WHT survey.

Having recognised these shortcomings in our search strategy, we embarked upon a second optimised search campaign, which is described in the following Chapter.

Chapter 4

Searching for nova shells around cataclysmic variables II

I intend to submit the contents of this chapter for publication in the Monthly Notices of the Royal Astronomical Society. The INT images presented in this chapter were taken by Vik Dhillon and myself during the two scheduled observing runs. We were also awarded additional time as part of the INT service observing programme, and the support astronomers present during the service nights took the images. They were Charlotte Carlisle, Ronny Errmann, Fatima Lopez, Manuel Diaz Alfaro, Ovidiu Vaduvescu, Paulina Sowicka, Nik Humphries, Luis Peralta de Arriba and Heloise Stevance. I reduced all of the INT images. The analysis of the images and the following text are my own work.

4.1 Introduction

In the previous chapter, I presented the results of our initial search for nova shells around CVs. We reported a number of tentative discoveries, and this spurred us on to examine a wider sample of CVs. Our scientific goal was to examine the theory of nova-induced cycles to explain why different types of CV can co-exist at the same orbital period (see Section 1.7).

Our first campaign suffered from some drawbacks which I described in Section 3.5.3, namely the WHT Auxiliary Port field of view was too narrow and the IPHAS survey exposure times were too short. We therefore applied for time on the WFC on the INT and we were allocated three nights in August 2014 and three nights in January 2015. We were also allocated time on the service observing programme which resulted in an additional 10 targets being observed. We observed 47 targets in total, primarily NLs, including 16 systems that we had previously examined in our first campaign using the WHT (see Table 3.2.1). All targets were outside the central galactic plane, with a galactic latitude of, $b > \pm 5^\circ$, i.e. outside the IPHAS footprint.

4.2 Observations

The observations were taken on several nights during 2014 and 2015, and a journal of observations is given in Table 4.1. We used the WFC mounted at the prime focus of the INT¹. The WFC consists of 4 thinned EEV 2kx4k CCDs, which are configured as shown in Figure 4.1. The WFC has a platescale of 0.33'' per pixel, with a field of view of $\sim 34' \times 34'$. We used the H α filter no. 197, which is centred on H α and has a bandpass of 95Å. We chose this filter because most nova shells are brightest in H α and this filter also includes a contribution from N[II] 6584Å emission, which may dominate the spectra of nova shells with strong shock interaction of the ejecta with any pre-existing circumstellar medium, e.g. T Pyx (Shara et al., 1989). We also used the Sloan r' band filter no. 214 (centred on 6240Å with FWHM 1347Å) to allow for the subtraction of field stars.

The observing conditions were good for most observations; the sky was always photometric, there was no evidence of dust and the seeing ranged from 1.0'' – 2.0'', although the seeing on 2015 February 23 flared to 4''.

We intended to obtain a total of 3600s exposure time for each target but this was not the case for all targets because of a misunderstanding by the support astronomer.

¹<http://www.ing.iac.es/Astronomy/instruments/wfc/>

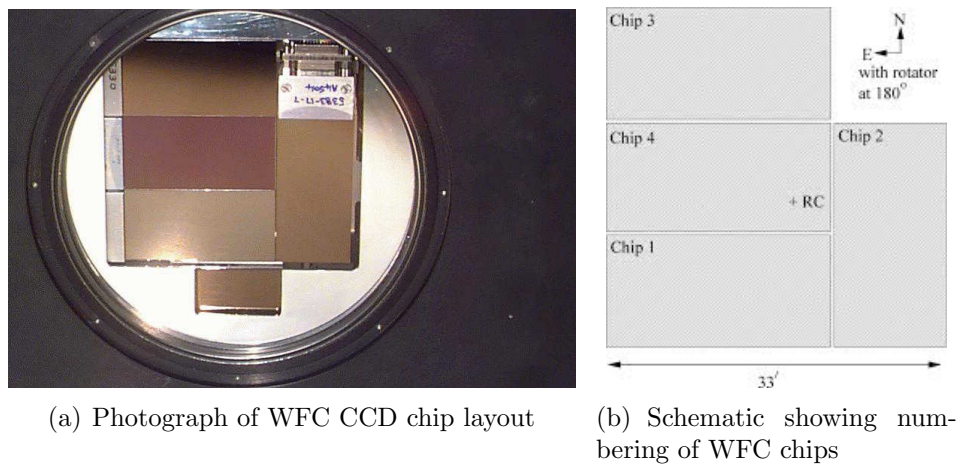


Figure 4.1: INT WFC chip

In order to eliminate the gaps between the chips in the camera, we used four exposures of 900s, and dithered by $20''$ in both RA and Dec. In hindsight, this dither pattern was too small to provide adequate removal of the chip gaps. The images we obtained are presented in Appendix B.

Table 4.1: Journal of INT observations (in alphabetical order of constellation). The classifications of the CVs have been taken from the RK catalogue. The date refers to the start time of the first exposure. Note that the RK catalogue classifications for novae are N, Na, Nb.

Object	Classification	Orbital period (hrs)	Date	UTC start	UTC end	No. of exps	Total exp time (secs)	Visible shell?
PX And	NL SW NS SH	3.51	01/08/14	04:43	05:16	2	1800	N
PX And	NL SW NS SH	3.51	04/08/14	03:18	03:42	4	1080	N
V794 Aql	NL VY	3.68	03/08/14	22:39	23:37	6	2880	N
V1315 Aql	NL UX SW	3.35	01/08/14	22:45	01:55	13	8700	Y
V1432 Aql	NL AM AS	3.37	02/08/14	21:43	23:16	32	3840	N
HL Aqr	NL UX SW	3.25	04/08/14	00:27	02:10	8	3840	N
UU Aqr	NL UX SW SH	3.93	01/08/14	03:16	04:36	7	3780	N
WX Ari	NL UX SW	3.34	15/01/15	20:37	22:01	8	3840	N
KR Aur	NL VY NS	3.91	18/01/15	01:26	02:45	8	3840	N
BY Cam	NL AM AS	3.35	15/01/15	23:48	01:26	8	3840	N

Continued on Next Page...

Table 4.1 – Continued

Object	Classification	Orbital period (hrs)	Date	UTC start	UTC end	No. of exps	Total exp time (secs)	Visible shell?
BZ Cam	NL VY SH	3.69	16/12/14	05:19	05:34	1	900	N
BZ Cam	NL VY SH	3.69	17/01/15	00:20	01:40	8	3840	N
V482 Cam	NL SW	3.21	18/01/15	02:49	04:06	8	3840	N
V425 Cas	NL VY	3.59	04/08/14	02:15	03:14	6	2880	N
V425 Cas	NL VY	3.59	27/10/15	22:43	23:29	3	2700	N
CH Crb	NL UX SW	3.49	23/02/15	06:09	06:24	1	900	N
V1500 Cyg	NL AM AS	3.35	01/08/14	02:23	02:57	3	2100	N
V2275 Cyg	Na IP	7.55	02/08/14	03:28	04:07	2	1800	N
V2275 Cyg	Na IP	7.55	03/08/14	23:43	00:22	4	1920	N
CM Del	NL UX VY	3.89	02/08/14	01:12	02:37	8	3840	N
MN Dra	DN SU ER	2.40	02/08/14	23:20	01:03	8	3840	N
OZ Dra	NL UX SW	3.28	18/01/15	05:16	06:17	6	2880	N
OZ Dra	NL UX SW	3.28	02/03/15	02:25	03:27	4	3600	N
V1084 Her	NL SW NS	2.89	02/03/15	03:31	04:34	4	3600	N
BH Lyn	NL SW SH NS	3.74	16/01/15	01:11	02:39	8	3840	N
BH Lyn	NL SW SH NS	3.74	29/01/15	01:27	01:42	1	900	N
BP Lyn	NL UX SW	3.67	17/01/15	02:20	03:39	8	3840	N
BP Lyn	NL UX SW	3.67	29/01/15	01:45	02:00	8	3840	N
HQ Mon	NL UX	7.58	16/12/14	04:15	04:30	1	900	N
V380 Oph	NL VY SW NS	3.7	28/05/15	23:58	01:00	4	3600	N
V1193 Ori	NL UX SW NS	3.96	17/01/15	21:32	23:10	8	3840	N
LQ Peg	NL VY SH NS	2.99	02/08/14	02:44	03:22	4	1920	N
FY Per	NL VY	6.20	15/01/15	22:05	23:36	8	3840	N
LX Ser	NL VY SW	3.80	03/08/14	21:12	22:33	8	3840	N
LX Ser	NL VY SW	3.80	17/01/15	06:03	06:55	3	2700	N
LX Ser	NL VY SW	3.80	18/01/15	06:19	06:24	3	180	N
LX Ser	NL VY SW	3.80	02/03/15	04:38	05:40	4	3600	N
RW Sex	NL UX	5.88	17/01/15	03:44	05:05	8	3840	N
RW Sex	NL UX	5.88	29/01/15	03:18	03:33	8	3840	N
SW Sex	NL UX SW	3.24	16/01/15	04:50	06:10	8	3840	N

Continued on Next Page...

Table 4.1 – Continued

Object	Classification	Orbital period (hrs)	Date	UTC start	UTC end	No. of exps	Total exp time (secs)	Visible shell?
V1294 Tau	NL VY SW	3.59	16/01/15	21:26	22:51	8	3840	N
V1294 Tau	NL VY SW	3.59	13/10/15	02:07	02:58	3	2700	N
RW Tri	NL UX SW	5.57	04/08/14	03:46	04:46	6	2880	N
DW UMa	NL SW SH NS	3.28	16/01/15	03:28	04:46	8	3840	N
DW UMa	NL SW SH NS	3.28	29/01/15	03:37	03:52	1	900	N
DW Uma	NL SW SH NS	3.28	23/02/15	04:12	04:59	3	2700	N
LN UMa	NL VY SW	3.47	18/01/15	04:11	05:08	6	2880	N
UX UMa	NL UX	4.72	16/01/15	06:15	06:59	6	2880	N
UX UMa	NL UX	4.72	17/01/15	05:09	05:57	6	2880	N
UX UMa	NL UX	4.72	01/03/15	03:15	04:16	6	3600	N
SS UMi	DN SU ER	1.63	01/08/14	21:32	22:35	4	3600	N
SS Umi	DN SU ER	1.63	02/08/14	21:16	21:29	4	240	N
HS0220+0603	NL UX SW	3.58	17/01/15	19:55	21:19	8	3840	N
HS0229+8016	NL UX VY	3.88	16/01/15	19:59	21:22	8	3840	N
HS0455+8315	NL VY SW	3.57	18/01/15	00:03	01:23	8	3840	N
HS1813+6122	NL UX SW NS	3.55	13/10/15	21:37	22:24	3	2700	N
HS1813+6122	NL UX SW NS	3.55	27/10/15	21:14	21:29	1	900	N
J0506+7725	DN SU	1.62	28/10/15	03:11	04:13	4	3600	N
J0809+3814	NL SW	3.21	29/01/15	01:07	01:22	1	900	N
J0928+5004	NL UX	10.04	29/01/15	02:04	02:19	1	900	N
J1429+4145	NL	1.64	23/02/15	05:03	06:05	4	3600	N
J1924+4459	NL SW SH NS	2.75	27/10/15	21:36	22:38	4	3600	N
Leo5	DN ZC	3.51	28/05/15	22:44	23:46	4	3600	N
LSIV-083	NL UX	4.69	29/05/15	01:11	02:13	4	3600	N
M57			01/08/14	02:00	02:13	6	360	N
RXJ0524+4244	NL AM AS	2.62	16/01/15	23:17	00:17	8	3840	N

4.3 Data reduction

The images were processed using the data reduction pipeline THELI (Schirmer, 2013). Bias correction was carried out using bias frames taken before and after the target exposures. Flat-fielding was performed using twilight flats. The astrometry was performed using standard astrometric catalogues (e.g. PPMXL, USNO, 2MASS) on each dithered exposure. The images were then co-added.

4.4 INT images and radial profiles

In order to detect shells in the images, I adopted the same two strategies as I did for the WHT images presented in Chapter 3. First, I visually examined each image using DS9 with high contrast. Second, I computed radial profiles for the target and comparison stars to detect any close-in shells. A key assumption in this technique is that the PSF is uniform across the WFC chip. Figure 4.2 shows the radial profiles for various field stars (circled) in the image of V1432 Aql on Chip 1 of the WFC. The PSFs show identical radial profiles irrespective of field position, giving confidence that the PSFs are uniform across the field of view of the CCD, as expected. I checked the other three CCDs of the WFC and the radial profiles were also identical across each chip though they were slightly different from each other.

The full set of INT images are shown in Appendix B. I detected no shells visually in any of the images, apart from the confirmation of the shell around V1315 Aql (see Chapter 5). None of the radial profiles of our targets showed any significant deviation from the field star radial profiles.

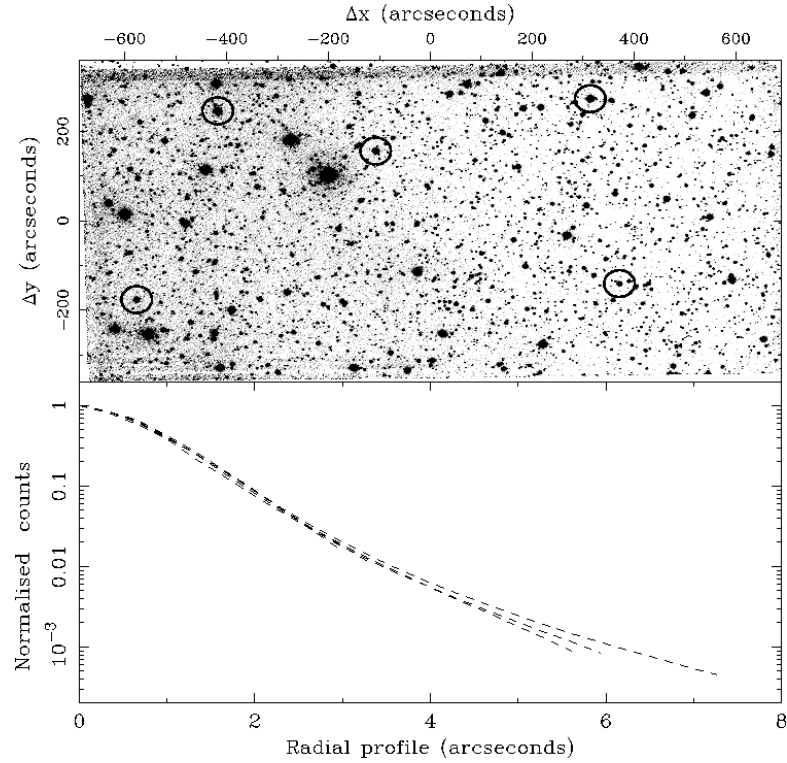


Figure 4.2: PSF test for Chip 1 of the INT WFC. The radial profiles of the circled stars in the upper frame are plotted in the lower frame. The ordinate axis on the lower frame shows the average counts in each pixel-wide annulus, centred on the star.

4.5 Combined results of our two campaigns and other recent work

In Table 4.2 I summarise the combined results from our first search, as described in Chapter 3, and from our second campaign, as described in this Chapter. I also include the results from two other similar campaigns by Schmidtbreick et al. (2015) and Pagnotta & Zurek (2016), neither of whom found shells around the CVs they examined.

Table 4.2: Summary of searches for nova shells, presented in Chapters 3 and 4, and by Schmidtbreick et al. (2015) and Pagnotta & Zurek (2016).

	Nova-like Variables	Polars & Inter- mediate Polars	Asynch Polars	Dwarf Novae	Old Novae	Total
1st Campaign (S15)						
WHT Targets	22	1	2	2	4	31
IPHAS Targets	5	10	2	34	23	74
less: Duplicated objects	-3				-1	-4
Total	24	11	4	36	26	101
2nd Campaign						
less: Duplicated objects	-16			3	1	-16
Total	51	11	4	39	27	132
Schmidtbreick et al. (2015)	5			10		15
Pagnotta & Zurek (2016)		1	4		1	6
less: Duplicated objects			-3			-3
Grand total	56	12	5	49	28	150

4.6 Discussion

Given the much increased rate of nova detection in modern times, it is very unlikely that nova eruptions would have been missed if they had occurred within the last 100 years or so. Shafter (2017) reviewed the current nova discovery rate and found that it was almost complete, although Schaefer (2014) suggests it could be as low as $\sim 50\%$. Let us assume for the time being that the nova discovery rate for the last century has been complete so that we expect to have to detect shells around NLs that are over 100 years old. To assess the chances of successfully identifying old shells, I need to estimate the brightness and size of the shells. I can calculate the luminosity of a nova shell from its age using the empirical relationship $\log_{10}(L_{\text{ergs s}^{-1}}^{H\alpha}) = 36.33 - 2.8 \times \log_{10}(t_{\text{years}})$ (Downes et al., 2001). The apparent size of a nova shell is determined by its distance, expansion velocity, and the time since eruption. Based on the distances of two recently discovered shells around dwarf novae (Shara et al. 2007, 2012), I adopt an average distance of 200 pc for my modelling. I can also take a typical value for the expansion velocity of a nova shell of 1500 km s^{-1} (Warner, 1995). Using these parameters, and

assuming a spherical shell geometry, a nova event 100 years ago in a novalike system 200 pc away, expanding at 1500 km s^{-1} would have a shell radius of $155''$, and a flux of $1.5 \times 10^{-19} \text{ ergs s}^{-1} \text{ cm}^{-2} \text{ arcsec}^{-2}$.

What does this mean for our chances of detecting shells? I simulated the visibility of nova shells to help assess the likelihood of detection. The simulations are shown in Figure 4.3. Note that these are realistic simulations which calculate the actual count rates that would be obtained with our instrumental setup, as output by the ING program `SIGNAL` for the INT WFC. The images are of 3600 s total exposure time, taken through an $\text{H}\alpha$ filter of bandpass 95\AA , with no binning. The three images show a simulation of a shell of age 100, 140 and 180 years. The central object has an apparent magnitude of $R = 16$. The shells in the images have fluxes of 1.5×10^{-19} , 3×10^{-20} and $9 \times 10^{-21} \text{ ergs s}^{-1} \text{ cm}^{-2} \text{ arcsec}^{-2}$, respectively. The shell in the 180 yr image is only just discernible. Hence, the faintest shells we expect to be able to detect in the images would be from eruptions that occurred 180 years ago. This estimate was calculated in dark time, reducing to 150 years in grey time, and to 130 years in bright time. The WHT images were all taken in dark time, as were most of the INT images. I also examined the radial profiles of my simulations and found that the shells were discernible up to 200 years, as shown in Figure 4.4.

The results shown in Table 4.2 bring the total number of NLs that have been observed to 56; 27 with the INT, 22 with the WHT, 5 by Schmidtobreick et al. (2015) and 2 in IPHAS. As discussed above, I expected to be able to detect shells up to 200 yr old with the INT and WHT (see Section 3.1). The images taken by Schmidtobreick et al. (2015) were 5389 s each, on the Max Planck Gesellschaft (MPG) 2.2m telescope on La Silla, so would have had at least as good a look-back time as our INT and WHT images.

What can we deduce from my discovery of a shell around one out of the 56 NLs that have been observed? Initially let us assume that the majority of novae that occurred in the last ~ 100 years would have been observed. These are classified as old novae in the RK catalogue and hence would not appear in our sample of NLs. We also know

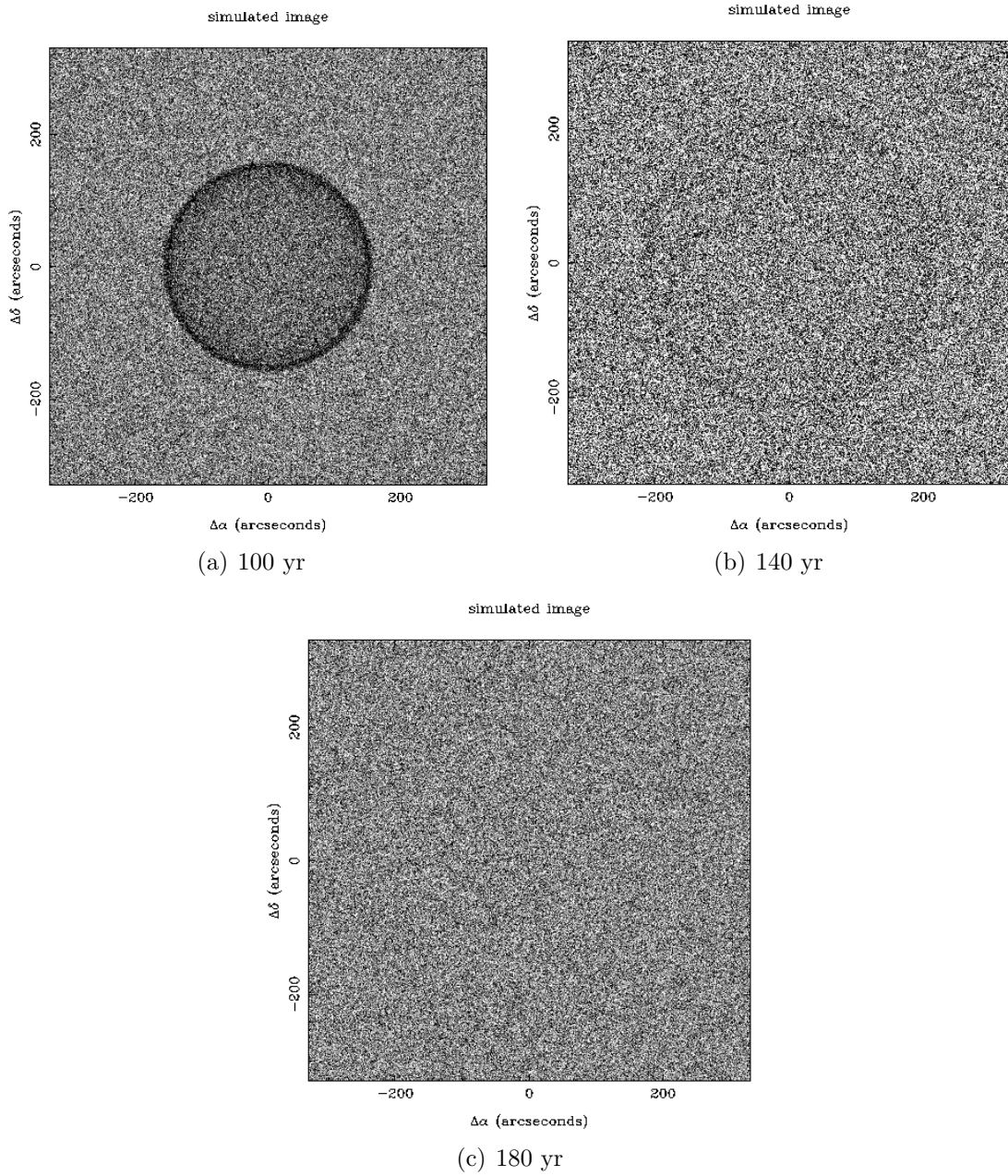


Figure 4.3: Simulated INT nova shell images with an expansion velocity of 1500 km s^{-1} and a distance of 200 pc. The simulations assume 3600 s total exposure time with the INT WFC in dark time.

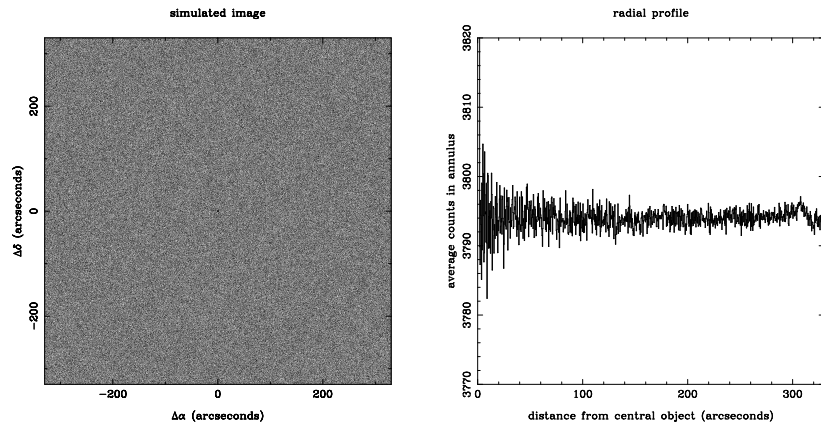


Figure 4.4: Simulated INT image and radial profile of a nova shell with an expansion velocity of 1500 km s^{-1} , with an age of 200 yr and a distance of 200 pc. The simulation assumes 3600 s total exposure time with the INT WFC in dark time. The shell is not visible in the image but is just discernible in the radial profile around $300''$.

from my simulations that my observations are probably not sensitive to shells older than ~ 200 yrs. Hence my search for nova shells around NLs is only likely to find shells between 100 and 200 years old. I found one shell in this 100-year window, out of 56 NLs surveyed, indicating that the lifetime of the NL phase lasts approximately ~ 5600 yrs. This is consistent with the order-of-magnitude estimate of 2000 years derived by Patterson et al. (2013) based on the transition of BK Lyn to a dwarf nova in the year 2011. However, the AAVSO light curve of BK Lyn² suggests that it has now reverted back to a nova-like state, indicating that the object is a Z Cam-type dwarf nova that has likely been transitioning from the nova-like to dwarf nova state for much less than the ~ 2000 -yr estimate of Patterson et al. (2013). Shara et al. (2017) found that the transition time for AT Cnc was much shorter at 330_{-90}^{+135} yrs. Hence our results lend some support to the nova-induced cycle theory, although we are dealing with a limited sample size; our survey of 56 NLs represents 65% of the 78 NLs in the

²<https://www.aavso.org/>

RK catalogue.

These results do not take account of other complicating factors. Duerbeck & Seitter (1987) found that nova shells decelerate as they collide with pre-existing CSM, with an average half-life of 75 yr. However this was based on only four nova shells, with an age range of 65 – 117 yr. One of the four shells (GK Per) has since been studied in greater detail by Liimets et al. (2012), Shara et al. (2012) and Harvey et al. (2016), all of whom found significantly less expansion than that measured by Duerbeck & Seitter (1987). Eammon Harvey (private communication) noted that Duerbeck's estimate was based on the observed size of the shells over time. However, the outer edge of the shell will cool and dim more quickly than the inner parts, so that the expansion of the shell will appear slower than if the outer layers continued to be visible. Other recent results using the velocities of individual fragments and knots of individual nova shells, suggest that the half-lives for nova shell deceleration are much longer (58 – 200 yr, Shara et al. 2012; and 100 – 6 000 yr, Liimets et al. 2012). Harvey et al. (2016) found no clear evidence for any deceleration of the knots in the GK Per shell. The relevance to my modelling of the visibility of nova shells is that any deceleration would render the shells smaller than in my simulations, which assumed a constant expansion velocity.

Another complication is that not all nova eruptions form visible shells. Downes & Duerbeck (2000) examined 30 novae and found only 14 visible shells, giving a success rate of 47%. There are likely to be many factors that result in a nova not producing a visible shell. Low mass, high speed ejecta will fade quickly and may never be visually resolvable. High speed shells may quickly become so large and faint that they too are beyond observational limits.

The situation is further complicated by my assumption of a homogeneous thin shell expansion. Images of nova shells (see Figure 1.10) show many shells with clumpy or filamentary structures, which are obviously far more complex to model than a simple spherical shell. Williams (2013) proposed that the nova eruption should invariably form clumpy ejecta due to the inhomogeneous nature of the thermonuclear runaway explosion and from Rayleigh-Taylor instabilities. These adiabatically expanding glob-

ules will have different sizes and interior conditions of temperature and pressure. Such structures would explain the range of ionisation species observed in nova shells, and their evolution over time. It would also help to explain the production of hard X-rays when globules collide in the early stages of the eruption. Williams (2013) goes on to suggest that the discrete globule model can also explain the appearance of the two main classifications of nova spectra, the ‘He/N’ and ‘Fe II’ classes (Williams, 1992). This shows that the determination of the age of a nova shell is complex, due to the inhomogeneous nature of the ejecta and our lack of knowledge about how the shell evolves.

Schmidtobreick et al. (2015) found no shells around the 15 CVs they examined. They calculated that their observations were sensitive to shells ranging from 3'' to 30'. For shells within 200 pc to 1 kpc, this means that they would have observed shells with diameters of 0.02–2 pc. They assumed constant expansion velocities of 300–500 km s⁻¹, which converts to ages of 50–2 000 yr. They argued that, as Shara et al. (2007) had discovered a 2 000 yr old shell around Z Cam, then all shells should remain visible for 2 000 yr. Finally, combining this with the fact that Downes & Duerbeck (2000) found that only 47% of novae form visible shells, then their results imply a nova recurrence time of 13 000 yr, with a 1-sigma confidence level.

I believe that the assumptions by Schmidtobreick et al. (2015) can be challenged. First, the luminosity of nova shells decreases as $\sim t^{-4} - t^{-5}$ (Downes et al., 2001) so most shells are undetectable after a few hundred years. As Shara et al. (2007) pointed out, the 2 000 yr old shell around Z Cam is most likely shock-ionised due to collision with circumstellar material (CSM), which may not be present around all novae. Second, the expansion velocities of nova shells range from 300 – 3 000 km s⁻¹ (Warner, 1995) so a better average velocity is 1 500 km s⁻¹. Hence I feel their estimate of the recurrence time is possibly overstated.

I note that a second new shell around a NL was very recently discovered by Guerrero et al. (2018). The shell had originally been classified as a planetary nebula but high-resolution, narrow-band O[III] and N[II] images and optical spectra have revealed that

it is a nova shell. The star at the centre of the shell, IPHASXJ210205+471015, has an optical spectrum very similar to RW Sex, a NL system, and shows photometric modulation with a period of 4.26 hr. Therefore there have been three shells discovered around DNe and two around NLs. These discoveries give support to the nova-induced cycle theory.

In the next Chapter I will describe my detailed investigations into the nova shell I discovered around the novalike V1315 Aql.

Chapter 5

Discovery of an old nova shell surrounding the cataclysmic variable V1315 Aql

The contents of this chapter have been accepted for publication in the Monthly Notices of the Royal Astronomical Society in a manuscript entitled '*Discovery of an old nova shell around the cataclysmic variable V1315 Aql*' by Sahman, Dhillon, Littlefair and Hallinan (Sahman et al., 2018). The images were taken by Vik Dhillon and myself using the INT on La Palma. The spectra were taken by Stuart Littlefair and Gregg Hallinan using the DEep Imaging Multi-Object Spectrograph (DEIMOS) on the 10m Keck II telescope on Hawaii. All subsequent data reduction and analysis, and the following text are my own work.

5.1 Introduction

Following my discovery of a faint shell around V1315 Aql in the IPHAS image, as described in Section 3.4.2, we included it in the list of targets for our second campaign using the INT. The second, deeper INT image clearly showed a bright H α shell centred on the CV, as shown in Figure 5.1. We subsequently obtained high resolution Keck

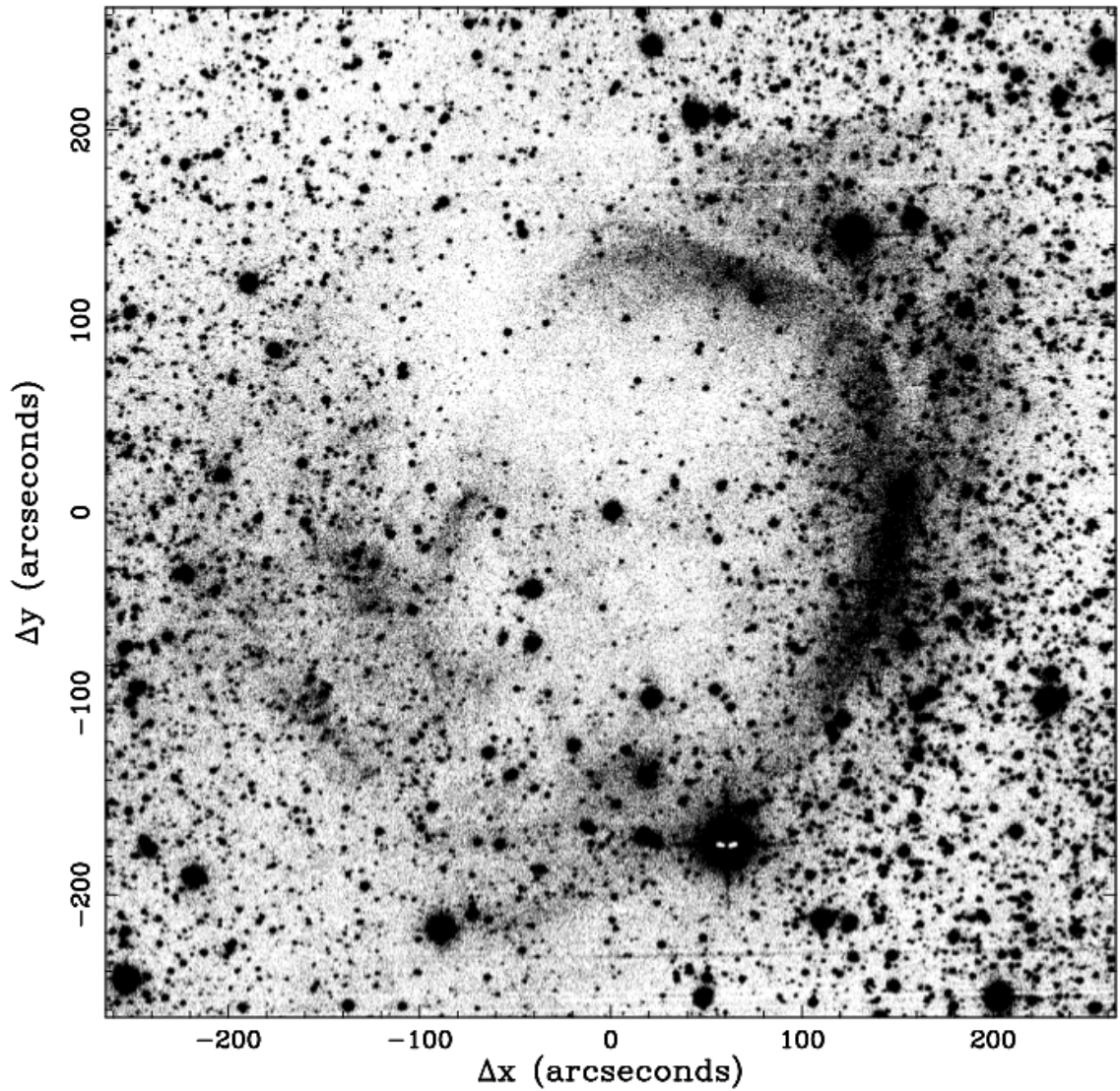


Figure 5.1: INT WFC $H\alpha$ image of the nova shell around V1315 Aql. The binary is located at the centre of the image. North is up and East is left.

spectra of the shell to determine its mass, age, composition and origin.

5.2 Observations

5.2.1 Keck DEIMOS spectra

We used the DEIMOS (Faber et al., 2003) multi-slit spectrograph on the 10m Keck II telescope on Hawaii. On the night of 2015 June 13, we obtained 39 spectra of 300s duration each, using the 1200G grating centred on 6000\AA and the GG455

Table 5.1: V1315 Aql DEIMOS slit positions, sizes and spectral range coverage. The RA and Dec positions are the centres of the slits.

Slit name	RA	Dec	Length (arcsecs)	Position angle (degs)	Width (arcsecs)	Wavelength (\AA)	
	(degs)	(degs)				Start	End
Blank Sky 1	288.5230602	12.2217710	58.9	154.4	0.7	4780	7432
Blank Sky 2	288.4896981	12.3217610	49.4	154.4	0.7	4867	7514
Shell 1	288.4995975	12.3003892	32.9	154.4	1.0	4868	7521
Shell 2	288.5116182	12.2922447	46.9	150.0	1.0	4915	7576
Shell 3	288.4560525	12.3369014	74.2	170.0	1.0	4686	7342
Shell 4	288.4507472	12.3566674	65.4	170.0	1.0	4699	7343
Shell 5	288.5171327	12.2647206	59.6	154.4	1.0	4877	7529
Shell 6	288.4757487	12.2611586	43.4	150.0	1.0	4614	7272
Shell 7	288.4367229	12.3103574	43.4	130.0	1.0	4487	7170
V1315 Aql	288.4769928	12.3013719	42.2	154.4	1.0	4735	7382
Star 1	288.5492156	12.2172214	49.2	154.4	1.0	5058	7565
Star 2	288.5403078	12.2461305	45.6	154.4	1.0	5047	7592
Star 3	288.5135945	12.2472213	42.0	154.4	1.0	4898	7455
Star 4	288.5604882	12.2053443	61.2	154.4	1.0	5038	7586

order-blocking filter. This gave a wavelength coverage of 4550–7500 \AA , with a FWHM resolution of 1.6 \AA . The seeing was 0.7'', and there was some thin cloud present.

The slit mask design requires that the slits cannot overlap in the spatial direction, so we placed seven slits around the edges of the roughly circular shell. We also placed a slit on V1315 Aql itself and chose four nearby stars for flux calibration. We identified two areas of blank sky for sky subtraction. The positions of each slit on the sky are shown in Figure 5.2, and full details of the position, orientation and wavelength coverage of each slit are given in Table 5.1.

5.2.2 *pt5m* – La Palma

Our Keck spectra included four stars for flux calibration but unfortunately they did not appear in any photometric catalogues. In order to allow us to perform flux calibration, we therefore obtained additional images of the four stars together with two catalogue stars (TYC 1049-408-1 and IPHAS J1911411.93+121357.7) using the 0.5m robotic telescope *pt5m* on La Palma (Hardy et al., 2015). The observations were taken

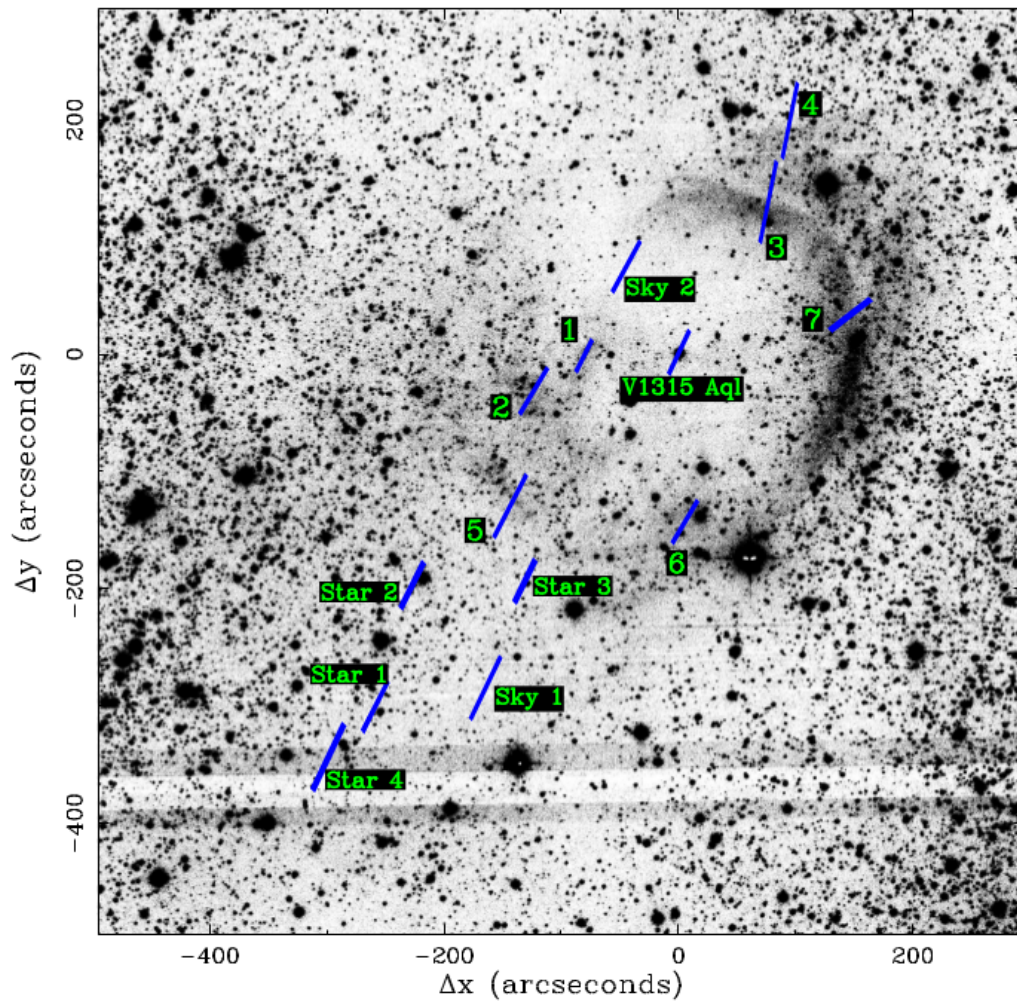


Figure 5.2: Overlay of the slit positions of the DEIMOS spectra on our INT H α image of V1315 Aql. The seven shell slits are numbered, and the two blank sky slits are also shown. North is up and East is left.

on 2016 October 7, when we took four images in each of the B , V , R , I filters with an exposure time of 1 minute each, and on 2016 Nov 18, when we took four 40 sec R -band images and four 360 sec B -band images.

5.3 Data Reduction

5.3.1 INT images

The INT images were debiased using the median level of the overscan strip and flat-fielded using normalised twilight sky flats. All image processing was carried out using THELI¹. Figure 5.1 shows the final stacked image of the shell.

5.3.2 Keck DEIMOS spectra

I used IRAF to reduce the DEIMOS spectra. The spectra were bias corrected using the overscan strip on the chips, and were flat-fielded using quartz lamp flats. I had difficulty in performing the background sky subtraction because the two blank sky slits we had chosen both contain small residual $H\alpha$ emission lines, possibly from the nova shell.

I then tried using the sky portion of our four flux calibration stars, but I found that the spectra of the three closest to the shell (Stars 1–3) also contained low levels of residual $H\alpha$ emission. (See Figure 5.5). The best results were obtained with sky from Star 4, which is furthest from the shell and showed negligible $H\alpha$ emission – this was used for all subsequent background sky subtraction.

5.3.3 *pt5m* images

The images were bias and flat field corrected using standard IRAF procedures. This allowed me to derive magnitudes for the four flux calibration stars, as shown in Table 5.2. I also found 2MASS infrared magnitudes (Skrutskie et al., 2006) for Star 2. Hence,

¹<http://www.ing.iac.es/astronomy/instruments/wfc/WFC-THELI-reduction.html>

Table 5.2: Magnitudes of the four flux-calibration stars observed with Keck DEIMOS. The errors on the B , V , R , I magnitudes are ± 0.3 magnitudes. See Table 5.1 for the positions of the stars on the sky.

Band	Star 1	Star 2	Star 3	Star 4
B	18.8	16.5	–	–
V	17.6	15.3	19.5	18.3
R	16.9	14.5	18.4	16.5
I	15.1	13.7	17.2	14.6
2MASS J	–	12.508	–	–
2MASS H	–	11.798	–	–
2MASS K	–	11.646	–	–

the star with the most complete set of magnitudes was Star 2. I input these values into the Virtual Observatory SED Analyser (VOSA – see Bayo et al. 2008) to determine the spectral type of Star 2, obtaining M4V (± 2). I then used VOSA to generate a template spectrum of an M4V star, which I used to flux calibrate the Keck spectra in IRAF.

5.3.4 Review of satellite imagery

I searched the GALEX UV satellite footprint using the GalexView interface (Bianchi 2014), but no observations were taken of the field around V1315 Aql. I also examined the WISE $22\mu\text{m}$ data (Wright et al. 2010), and there was no emission in the vicinity of V1315 Aql.

5.4 Results

5.4.1 INT image

The $H\alpha$ image of the shell surrounding V1315 Aql was reduced as described in Section 4.3 and is shown in Figure 5.1. The images clearly show one, possibly two roughly spherical shells centred on V1315 Aql. The lobe towards the West has the most prominent emission. There was no evidence of nebulosity on wider scales than

shown in Figure 5.1.

There is a possibility that the shell is unrelated to V1315 Aql, and it may just be a line-of-sight alignment of a foreground or background cloud of gas in the Milky Way. To determine that the shell does indeed originate from V1315 Aql, I need to determine if it has the same systemic velocity as the binary, and that its composition is comparable to other nova shells, and to rule out other types of nebulosity e.g. planetary nebulae, supernovae remnants, etc.

5.4.2 Geometry of the shell

In Figure 5.3 I show the image of the shell with circles, centred on V1315 Aql, overlaid. The radii of the circles are $100''$, $180''$ and $240''$. The inner annulus between $100''$ and $180''$ contains the most prominent areas of emission (from the North around to the West), and appears to be centred on V1315 Aql. The outer annulus also contains a fainter arc of emission to the North-West, and some fainter areas of emission to the South-East, which also appear to be centred on V1315 Aql.

5.4.3 Keck DEIMOS spectra

In Figure 5.4 I show the spectrum of V1315 Aql. The spectrum shows strong, broad (FWHM of $H\alpha$ is 900 km s^{-1}) Balmer and HeI emission lines from the accretion disc. The spectrum is very similar to that shown in Dhillon & Rutten (1995).

5.4.4 Emission lines

The spectra of the seven shell slits and the blank sky slits in the range $6540\text{--}6600 \text{ \AA}$ are shown in Figure 5.5. Note that the blank sky 2 slit spanned two CCDs in the spectrograph and each part is shown separately. The shell spectra show single-peaked emission lines of $H\alpha$, and a pair of N[II] lines at 6548 and 6583 \AA . These lines are characteristic of old nova shells (Downes et al., 2001).

I also detected $H\beta$ in those shell spectra that covered 4861 \AA . Unfortunately, none

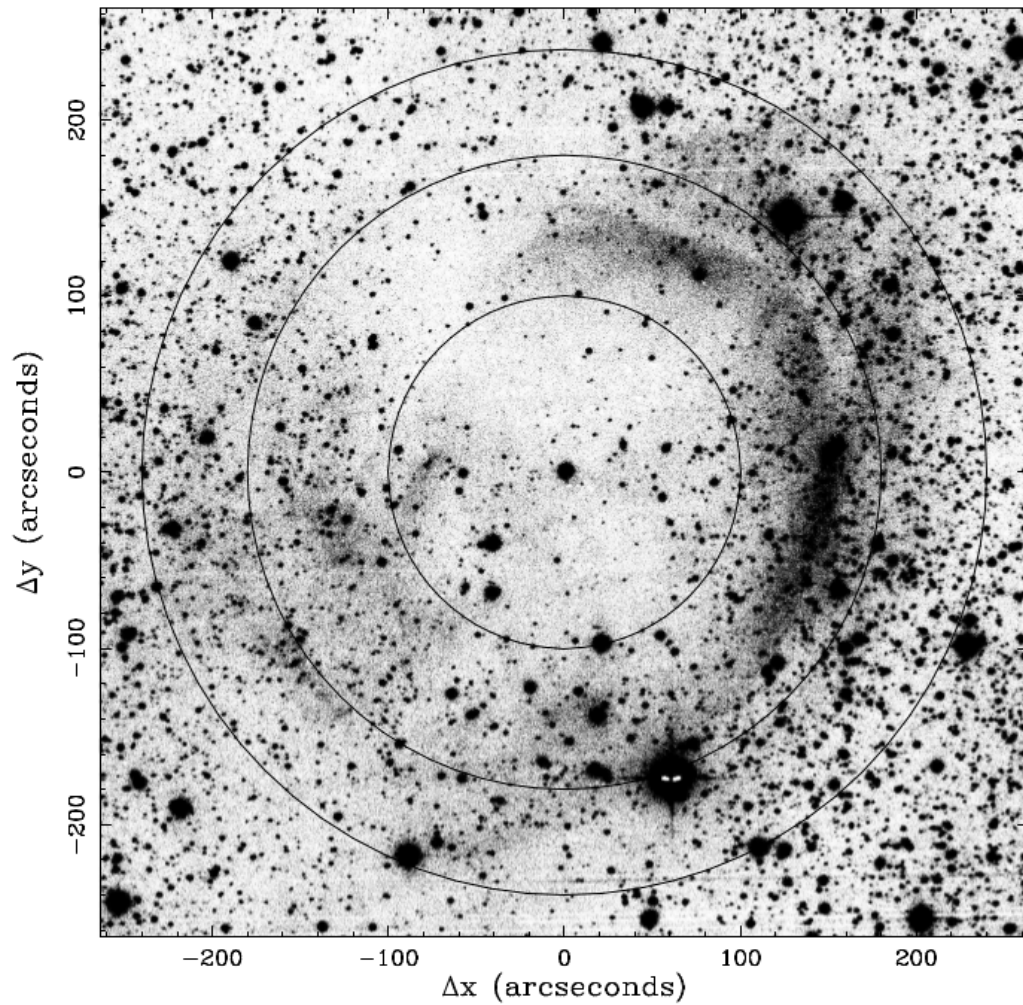


Figure 5.3: INT H α image of the shell with overlaid circles centred on V1315 Aql of radii 100'', 180'' and 240''. North is up and East is left.

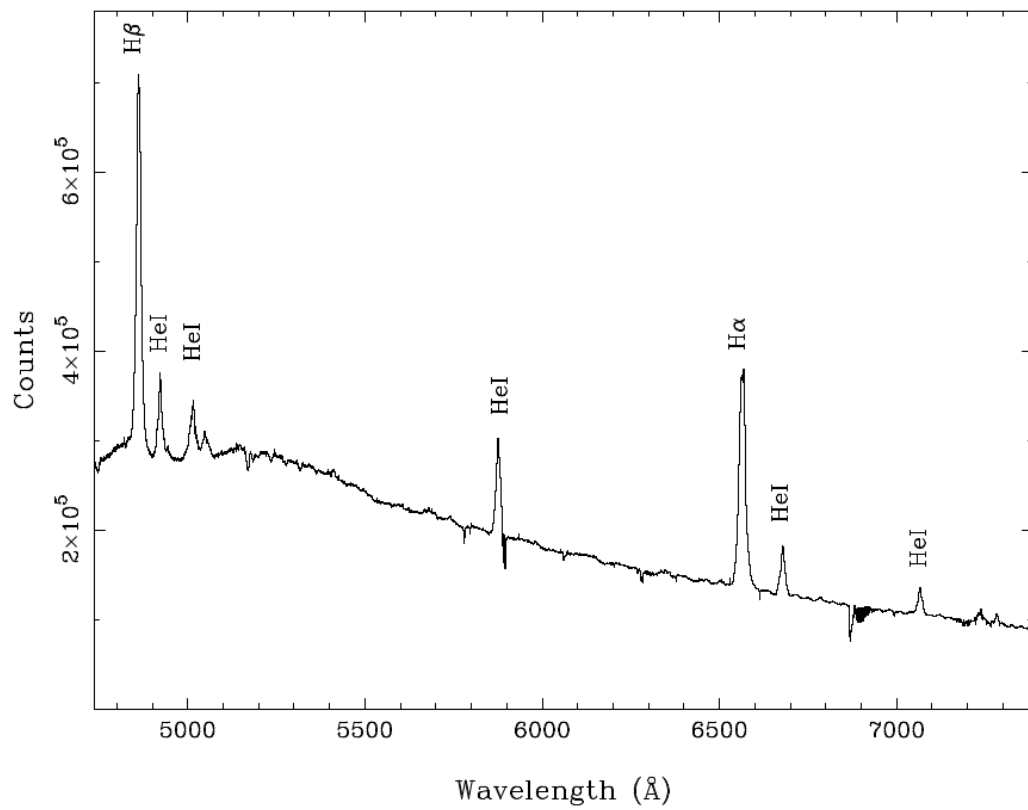


Figure 5.4: Keck DEIMOS spectrum of V1315 Aql. Note that we did not flux calibrate this spectrum because the flux calibration stars do not cover its whole wavelength range.

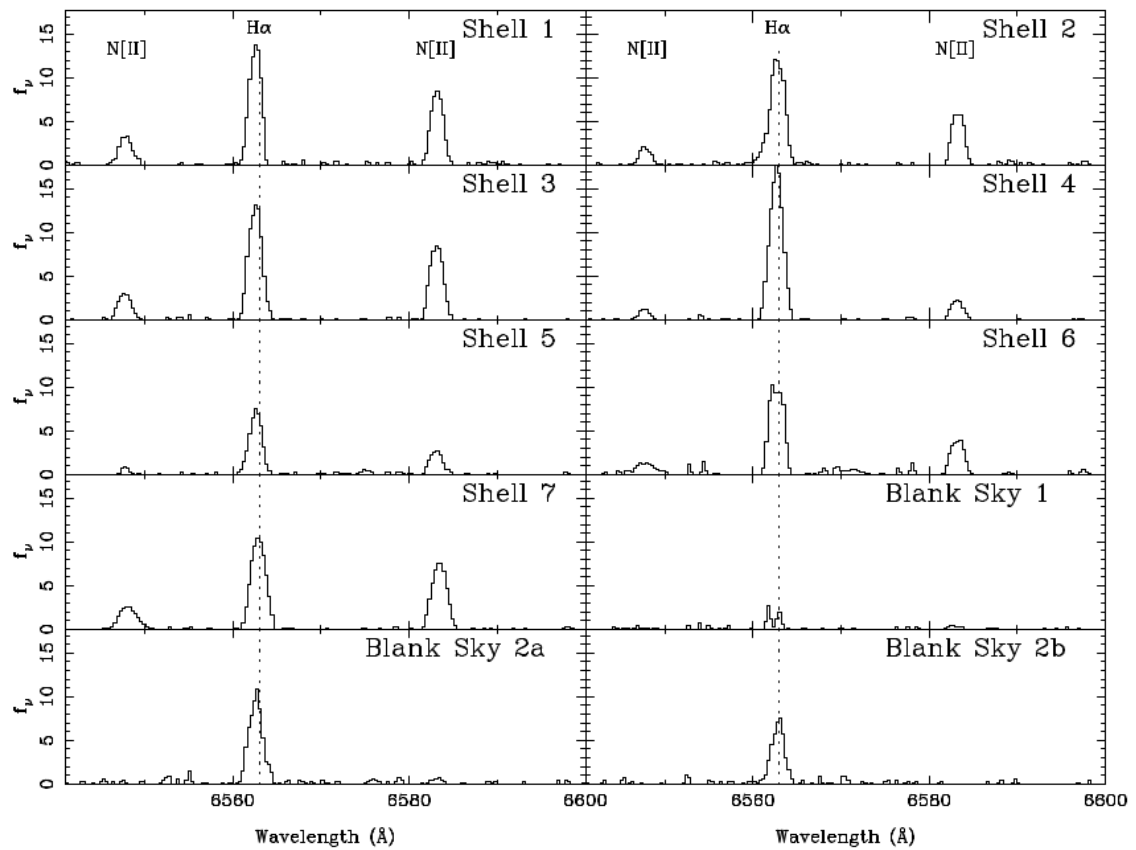


Figure 5.5: Spectra of the seven shell slits (see Figure 5.2), and the blank sky slits from 6540–6600Å. Flux is in units of $\mu\text{Jy arcsec}^{-2}$. The shell spectra all show the presence of H α and N[II] 6548Å and N[II] 6583Å. H α is also present in the blank sky slits. The Blank Sky 2 slit fell across two CCDs on the detector and so we show each spectrum separately, as 2a and 2b.

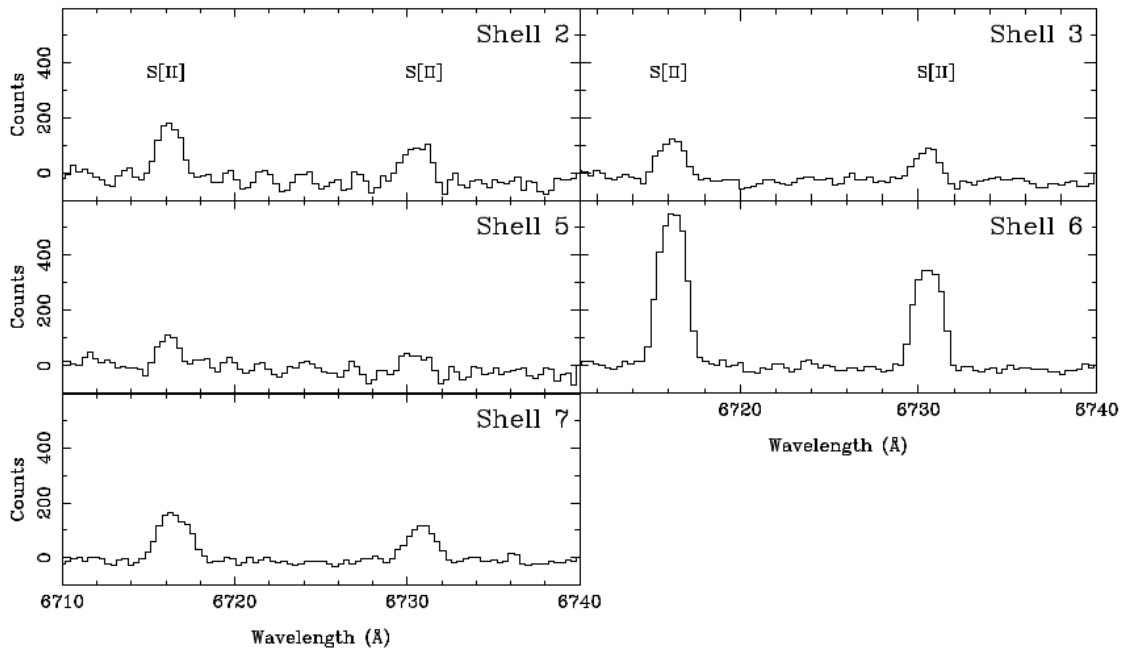


Figure 5.6: Spectra of the five shell slits from 6710–6740Å, showing the S[II] emission lines at 6716 and 6731Å.

of the spectra of the four flux-calibration stars covered this wavelength, and hence I was unable to flux calibrate the $H\beta$ lines. I also found the S[II] 6716 & 6731Å lines in shell slits 2, 3, 5, 6 and 7, as shown in Figure 5.6. The average ratio of the two S[II] lines was 1:1.4.

I searched for the emission lines N[II] 5755Å, O[I] 6300, 6300, 6364Å and O[III] 4363, 4959, 5007Å often seen in nova shell spectra but none were detected. There are faint lines at 5679, 5740 & 5742 Å, presumably from NI and NII, in shell slits 3 and 4, but these are not present in any other slits.

There is also $H\alpha$ emission present in both the sky portions of the slit centred on V1315 Aql, though any N[II] lines present are lost in the noise. We show the $H\alpha$ line profile from the sky on the South-East side of the V1315 Aql slit in Figure 5.7.

The FWHM of the $H\alpha$ and N[II] lines of all the shell slits are listed in Table 5.3.

5.4.5 Systemic radial velocity of V1315 Aql

Historically the systemic velocity of V1315 Aql, γ , has been difficult to determine because of the complex behaviour of its disc emission lines and lack of absorption lines

from the primary and secondary stars. Downes et al. (1986) presented radial velocity data for H β , H γ and HeII 4686Å emission lines. They derived values for γ consistent with zero from the H β and HeII 4686Å lines, but the H γ line gave a value of 100 km s⁻¹. Dhillon et al. (1991) also used the H β , H γ and HeII 4686Å emission lines and the HeI 4471Å line and derived a γ range of -4 to +93 km s⁻¹. Given the unreliability of the broad emission lines from the accretion disc to determine γ , in the following subsection I will use my own measurements of the radial velocity of the shell to determine if they are consistent.

5.4.6 Radial velocities of shell emission lines

To measure the radial velocities of the emission lines, I fitted Gaussians to the H α lines of the shell and measured the wavelengths at the centre of the Gaussians. The resulting radial velocities are shown in Table 5.3.

The spectrum of the sky on the south-east side of the slit centred on V1315 Aql is shown in Figure 5.7. The plot shows tentative evidence of a double peaked structure. I measured the radial velocities of each peak to be -33 & 14 km s⁻¹. If I assume that the two peaks represent emission from the front and back edges of a spherically expanding shell, then the average of the two gives a systemic velocity of $\gamma \approx -10$ km s⁻¹, and an expansion velocity of ~ 25 km s⁻¹. I analysed the sky on the north-east side of V1315 Aql and it too showed a double peak structure, although it is less pronounced.

The seven shell slits were placed at the edges of the shell. The expansion velocity of the edge of the shell will be tangential to the line of sight and will not affect the radial velocities, which should be similar to the overall systemic velocity. The measured shell radial velocities are shown in Table 5.3 and are broadly comparable with the systemic velocity of -10 km s⁻¹ derived above, apart from shells 6 & 7 which differ by 14 & 16 km s⁻¹ respectively.

The Galactic velocity of V1315 Aql relative to the sun can be derived from its Galactic coordinates, $l = 46.4^\circ$, $b = 0^\circ$, which give a radial velocity of 7 km s⁻¹. This

Table 5.4: H α and N[II] flux (ergs/s/cm²/arcsec² $\times 10^{-18}$) from the seven shell slits. The errors on the flux values are $\pm 25\%$.

Shell slit No.	H α	N[II] 6548Å	N[II] 6583Å
1	17.2	4.22	10.8
2	18.1	2.10	7.64
3	18.3	4.16	11.8
4	24.2	1.47	3.03
5	9.58	0.73	3.62
6	15.4	2.64	5.61
7	16.2	4.80	11.9

is broadly consistent with the systemic velocity derived above.

5.4.7 Line fluxes

The fluxes of the emission lines from the shell in each of the slits are given in Table 5.4. Assuming a shell radius of 220'', a distance of 443 parsecs using Gaia DR2, and using the H α flux from each slit, I can estimate the total flux from the whole shell. However, it can be seen by examining Figure 5.3 that the shell is fragmented and clumpy and only a small fraction is actually emitting. If I assume that 10% of the full shell is emitting and take an average H α flux from the seven shell slits of 1.70×10^{-17} ergs/cm²/sec/arcsec², I obtain a total H α luminosity of $L = 6.9 (\pm 3.1) \times 10^{30}$ ergs/sec.

The plots of Downes et al. (2001) showing the temporal reduction in the H α luminosities of shells from fast and slow novae, have a lower limit of $\log L = 30$ at 100 years. I note that the source of the V1315 Aql luminosity is likely to include emission from shock interaction with pre-existing ISM. This would enhance the flux, and lead to an underestimate of the age of the shell. I conclude that the shell is likely to be significantly older than 100 years.

5.4.8 Time of nova eruption

In Sahman et al. (2015) I derived the age of the shell using a distance of 356_{-80}^{+65} pc taken from Ak et al. (2007), and a constant shell expansion rate of 2000 km s^{-1} . I measured the radius of the shell at $\sim 2.5'$, which gives an age of 120 yr.

The Gaia DR2 gives the distance to V1315 Aql as 443_{-7}^{+6} pc. The angular radius of the shell in Figure 5.3 is $\sim 3.5'$, giving a physical radius of $1.4 \times 10^{13} \text{ km}$ ($\sim 10^5 \text{ AU}$). Using a constant shell expansion velocity of 1500 km s^{-1} , gives an age of 290 yr. However, this takes no account of any slowing of the ejecta as it encounters CSM. Duerbeck & Seitter (1987) found that the velocity of nova shells reduces by half every 50–100 yrs. This result has been challenged using more accurate measurements of shell expansion, which suggests that much less deceleration than previously thought Harvey (2017). Using my measured expansion velocity of $\sim 25 \text{ km s}^{-1}$, and assuming an initial velocity of 2000 km s^{-1} (see Table 8.1 Bode & Evans 2008), a deceleration half life of 110 yr, would give a final velocity of $\sim 25 \text{ km s}^{-1}$ after ~ 300 yr.

However, if I take more extreme values for the initial ejection velocity, say 1500 km s^{-1} and a deceleration half-life of 150 yrs then the age of the nova increases to 1200 yrs. This leaves us with a considerable age range for the shell of 290–1200 yr.

Assuming the visual magnitude of V1315 Aql was the same prior to the nova event as it is now, $m_V = 14.3$, and taking the average brightening of a nova to be ~ 11 magnitudes (Bode & Evans 2008), the system would have been at $m_V \sim 3.3$ at peak brightness, clearly visible to the naked eye. Novae decline rapidly and so it would have dropped below the naked-eye visibility limit of $m_V \sim 6$ within a few days. I reviewed the catalogues of ancient Chinese and Asian novae and supernovae sightings by Stephenson (1976) which includes sightings from 532 BC up to 1604 AD. I could find no record of an event close to the coordinates of V1315 Aql. If the nova eruption occurred when V1315 Aql was close to the Sun in the sky, and it was brighter than $m_V \sim 6$ for only a few days, it may well have been hidden in twilight and hence gone unnoticed.

5.4.9 Temperature and density of the shell

The method most often used to determine the temperature and density of gaseous nebulae is to measure the ratio of the intensities of particular emission lines from the same species of ions. Two ions which are often used are N[II] and O[III]. We were unable to detect any O[III] lines in our spectra, and the N[II] ratio requires a flux measurement of the 5755Å line, which we were only able to detect very weakly in shell slit 1. It was not present in any other slit. Hence we can only place an upper limit on the electron temperature (T_e) of the shell of 5,000 K using Figure 5.1 from Osterbrock (1989).

5.4.10 Mass of the shell

I can derive a rough estimate of the mass of the shell using the technique set out in Corradi et al. (2015). They derived the ionised hydrogen masses of several planetary nebulae using the formula

$$m_{\text{shell}}(H^+) = \frac{4\pi D^2 F(H\beta) m_p}{h\nu_{H\beta} n_e \alpha_{H\beta}^{eff}(H^0, T_e)}, \quad (5.1)$$

where D is the distance to the object, $F(H\beta)$ is the $H\beta$ flux, m_p is the mass of a proton, $h\nu_{H\beta}$ is the energy of an $H\beta$ photon, n_e is the electron density per cm^3 , and $\alpha_{H\beta}^{eff}(H^0, T_e)$ is the effective recombination coefficient for $H\beta$. This formula is also applicable to nova shells (Osterbrock, 1989).

As I pointed out in Section 5.4.4, the spectra of our four flux calibration stars do not cover $H\beta$ so I am unable to derive a flux directly. However, I can make a rough estimate as follows. The $H\beta$ line is present in four shell slits (Nos. 3, 4, 6 and 7). I can measure the counts for both $H\alpha$ and $H\beta$. The DEIMOS exposure time calculator for a source whose flux is flat in frequency gives the ratio of counts for $H\alpha:H\beta$ as approximately 1:0.3. Assuming that 10% of the full shell is emitting and taking an average $H\alpha$ flux from the seven shell slits of 1.70×10^{-17} ergs/cm²/sec/arcsec² I obtain

a total H α flux of 2.49×10^{-13} ergs/cm²/sec from the whole shell, allowing me to derive an H β flux of $F(H\beta) = 8.9 \times 10^{-14}$ ergs/cm²/sec.

The electron density, n_e , can be estimated using the S[II] 6716 and 6731 line ratio, which I found to be 1.4 (see Section 5.4.4). Figure 5.8 in Osterbrock (1989) shows the electron density versus intensity ratio at $T = 10,000$ K and indicates a scaling of $n_e(10^4/T)^{1/2}$. I found a maximum temperature of 5,000K which gives an electron density of ~ 40 cm⁻³.

Finally, using the Gaia DR2 distance of 443 pc and a value for $\alpha_{H\beta}^{eff}(H^0, T_e)$ of 3.78×10^{-14} , for Case A conditions at $T_e = 5000$ K listed in Table 4.1 of Osterbrock (1989) gives a maximum mass of

$$m_{\text{shell}}(H^+) \simeq 2 \times 10^{-4} M_{\odot}. \quad (5.2)$$

There is no need to correct for extinction as Rutten et al. (1992) found $E(B - V) = 0$ for V1315 Aql using *IUE* spectra of interstellar absorption bands around 2200Å. In view of the many assumptions used to estimate of the mass of the shell, it should be treated as an order of magnitude approximation.

As nova shells expand, they decelerate as they sweep up pre-existing circumstellar gas, which leads to a doubling of their mass every 50–100 yrs (Duerbeck & Seitter, 1987). I estimated the age of the shell in Section 5.4.8 as 500–1200 yrs, so the original ejected mass of the shell would have been substantially lower than the value I have derived above, giving a maximum ejected mass of $\lesssim 10^{-5} M_{\odot}$. This rules out a planetary nebula origin, which typically have masses in the range 0.1–1.0 M_{\odot} (Osterbrock, 1989). Nova shells typically have masses in the range 10^{-4} – $10^{-6} M_{\odot}$ (Yaron et al. 2005), so my estimate of the shell mass in V1315 Aql of $\sim 10^{-5} M_{\odot}$ is in accordance with this.

5.5 Discussion

I can summarise my findings as follows. The shell is broadly spherical and appears to be centred on V1315 Aql, strongly suggesting that the shell is associated with the central binary. The systemic velocity of the shell measured from the sky portion of the V1315 Aql slit and at the edges of the shell are broadly consistent. The absence of $22\mu\text{m}$ emission precludes a planetary nebula origin (Mizuno et al. 2010). I derive an order-of-magnitude estimate of the mass of the shell of $\sim 10^{-5} M_{\odot}$ which rules out a planetary nebula or supernova origin. I conclude that these results indicate that the shell is associated with V1315 Aql.

At this stage of the shell's evolution, the luminosity of the outer edges of the shell is most likely fuelled by two processes, recombination and shock interaction with pre-existing CSM. My flux measurement will include contributions from both of these processes, making it difficult to estimate the physical conditions in the shell as a whole. Furthermore, the lack of other forbidden emission lines in the shell spectra, especially N[II] 6583Å and O[III], means I cannot determine the physical parameters of the shell to confirm conclusively that it exhibits properties consistent with a nova origin.

In Section 4.6, I estimated that the nova-like phase following a nova eruption lasts ~ 5600 yrs. My estimate of the time since the nova eruption on V1315 Aql of 290–1200 yrs is consistent with this timescale, and lies within the overall nova recurrence timescale of 13 000 yrs found by Schmidtobreick et al. (2015).

In the next Chapter, I summarise my research into the evolution of CVs and discuss possible future work.

Chapter 6

Conclusions and Future Work

6.1 Conclusions

In this thesis I have set out the results of my research into two aspects of CV evolution theory; recurrent novae as possible progenitors of SNe Ia and the nova-induced cycle theory to explain how different types of CV can coexist at the same orbital period.

6.1.1 Recurrent Novae as Progenitors of SNIa

As I set out in Chapter 1, the exact nature of the progenitors of SNIa remains an area of active ongoing research. More accurate and more plentiful observations have become available in recent years, and it is apparent that there is a larger diversity of under- and over-luminous subclasses than originally thought. Hence, the number of potential candidate progenitor systems has increased.

For many years, the SD model was the favoured model, as it appeared to readily provide a way to grow a WD up to the Chandrasekhar limit. But it has faced a growing number of challenges. Modelling shows that it is difficult for WDs to accrete matter due to significant mass losses during nova events. Furthermore, no evidence has ever been found of a companion, neither in pre- nor post-explosion images nor in the expected spectral signature of the interaction of the ejecta with a companion. The observed delay time distribution of SNIa in galaxies cannot be reconciled with SD models. And

the continuing difficulty of the SD model is the lack of hydrogen seen in SNIa spectra. As a result, the DD model has gained favour and is now probably the leading contender. Earlier difficulties with the DD model, especially the paucity of observed systems, have now been resolved (Maoz et al., 2018). However, problems remain with all proposed SNIa progenitor models, and many researchers are now suggesting that SNIa are most likely derived from multiple channels (Livio & Mazzali 2018, Patat & Hallakoun 2018).

Recurrent novae are one of the leading progenitor candidates in the SD model. I determined the system parameters of the recurrent nova CI Aql, which had its last outburst in 2000. I used the dynamical mass technique, which is widely accepted to give the most accurate determination of the masses of the two stars. I found that CI Aql harbours a WD with a mass of $1.00 \pm 0.14 M_{\odot}$, and a secondary of mass $2.32 \pm 0.19 M_{\odot}$ and spectral type F8IV, although the recent Gaia DR2 distance suggests it could be an earlier type. These values imply that it is the nuclear evolution of the secondary, which is evolving away from the main sequence, that is driving the mass transfer at high rates ($10^{-8} - 10^{-9} M_{\odot} \text{yr}^{-1}$). The continued expansion of the secondary causes thermal timescale mass-transfer and will ultimately lead to steady hydrogen burning on the surface of the WD. At this point the system will become a supersoft X-ray source. The recurrence period of CI Aql is still subject to debate but if the 20-year period proposed by Schaefer (2001) is correct, then another recurrent nova outburst is imminent. The masses of the two components lie in the region of systems that will ultimately explode as a SNIa, according to the models of Ivanova & Taam (2004). I also point out that the finding by Hachisu & Kato (2018) that CI Aql will not end as a SNIa ignores the fact that once the mass ratio has been reversed, mass transfer will still continue, driven by angular momentum losses, and ultimately the WD will reach M_{Ch} .

6.1.2 Nova-induced cycle theory

The original motivation of Shara to develop the nova-induced cycle theory to explain the conflict between the observed space density of CVs compared to the Galactic nova rate has largely been removed as more CV systems have been discovered. The theory, however, can also provide an explanation of how different categories of CV can co-exist at the same orbital period. It proposes that CVs cycle through nova, novalike, and dwarf nova phases, then possibly become detached and go into hibernation, until orbital momentum losses bring the secondary back into contact with its Roche lobe, and mass transfer resumes, leading ultimately to another nova eruption. The existence of nova shells around DN and NLs would give support to the theory.

I have reported the results of the two observational campaigns searching for nova shells around CVs to constrain aspects of the nova-induced cycle theory. The first campaign examined 31 CVs with the WHT and 74 in IPHAS. The images were examined visually for shells around the CVs, and the radial profiles of the CVs were plotted and compared to field stars, though this was only done for the WHT targets. I found a number of tentative discoveries, one of which was subsequently confirmed in the second campaign (see below).

The second campaign was conducted using the WFC on the INT. I observed 47 CVs but found no new shells, other than a confirmation of the shell around V1315 Aql. Using a simple model of a spherical shell, I estimated that I should be able to identify shells up to ~ 200 yr old, but it is worth noting that the three shells that have been identified around the DNe Z Cam, AT Cnc and Nova Sco 1437 (Shara et al. 2007, 2012, 2017) are much older than this (240–2400 yr, 330 yr, and 581 yr respectively). Similarly, the DN discovered inside the nebula Te 11 is believed to be coincident with the ancient nova dating back to 483 CE (Miszalski et al., 2016). It is likely that the visibility of these old shells is due to shock interaction with the pre-existing ISM, rather than recombination and photo-ionisation by the hot WD which are the usual sources of the shell luminosity.

In summary, I observed 132 CVs, of which 51 were NLs. Combining this result with the search by Schmidtobreick et al. (2015) brings the total to 56 NLs. I found only one shell around these 56 NLs. Assuming that the observations were sensitive to shells up to ~ 200 years old, and assuming that all novae in the last century would have been observed, these results imply a post-nova NL-phase of $\sim 5,600$ yrs. This is broadly consistent with the results of other researchers.

Finally, I described my discovery of a previously unknown nova shell around the V1315 Aql. I found that the shell around V1315 Aql is geometrically centred on the CV and has a comparable systemic velocity to the central binary. Estimates of its composition and mass were difficult due to the lack of key emission lines in its spectra, but my order of magnitude estimate of its mass ($m_{\text{shell}}(H^+) \simeq 2 \times 10^{-4} M_{\odot}$) puts it firmly in the realm of old nova shells, and precludes a planetary nebula or SNIa origin. This leads me to conclude that the shell is associated with the central binary from an earlier nova explosion. The date of the nova explosion is also difficult to establish due to uncertainties in the current velocity and deceleration of the shell. Hence I derive a broad age range of 290–1200 yrs. I searched archival records but could find no record of a nova at the vicinity of V1315 Aql, though it may have been lost in twilight for the week or so that it was visible to the naked eye.

Whilst there have been four old nova shells found around dwarf novae, my discovery of the V1315 Aql shell is the first around a novalike. A second novalike shell discovery was also recently announced (Guerrero et al., 2018). These discoveries show that the underlying CVs have experienced nova eruptions and lend strong support to the nova-induced cycle theory.

6.2 Future work

There are a number of ways in which the two aspects of CV evolution theory I have studied in my thesis can be progressed in the future, which I outline below.

6.2.1 Recurrent Novae as Progenitors of SNIa

As with many areas of astronomy, the study of recurrent novae is hampered by low sample sizes, and only 14 RNe are currently known. Pagnotta & Schaefer (2014) identified many classical novae that they believe are RNe for which only one eruption has been identified. They used seven key characteristics of RNe and looked for CNe that exhibited similar characteristics. They estimate that roughly a quarter of the ~ 400 known Galactic novae are actually RNe. A proportion of these potential RNe systems will be eclipsing so it would be worthwhile to determine the system parameters in cases where this has not been done before. This would provide an accurate baseline of system parameters, including the component star masses, to assist in determining the mass loss or gain from any further recurrent nova eruptions.

Whilst the orbital periods of CVs can be measured to high accuracy, the determination of the masses of the components remains difficult. Members of the Sheffield Astrophysics group use eclipse models incorporating Gaussian processes to determine the masses of eclipsing short-period CVs. It may be possible to use this technique with eclipsing classical and recurrent novae, although in these systems the optical flux is often dominated by the accretion disc, which can obscure the ingress and egress of the bright spot and the WD.

About 11,000 SNIa are currently known. Future all sky surveys eg. DES, Gaia, SDSS V, Euclid, JWST, LSST, TESS, will identify many more. The Dark Energy Survey (DES) is specifically targetting SNIa to study cosmic expansion, and is expected to collect data on $> 10^5$ SNIa and their host galaxy. However, the progenitor problem will be better addressed by earlier, deeper and more prolonged spectroscopic observations, to gather information on the detailed physics of the explosion and the surrounding environment.

The other surveys will uncover many more CVs of all types, some of which will be RNe. In addition, our knowledge of the space density of double WDs will be greatly enhanced by the gravitational wave detections by LISA, which is expected to detect

$> 10^5$ WD pairs (Korol et al., 2018). The most recent Galactic SNIa happened in 1604 and is now known as Kepler's Supernova. They are expected to recur every few 100 yr so we are due another one soon. If it occurs after LISA is operational, then we should be able to determine if it was due to merging WDs.

6.2.2 Nova-induced cycle theory

There is another $H\alpha$ survey underway to provide a southern counterpart to IPHAS. The new survey uses OmegaCAM on the 2.6m VLT Survey Telescope (VST) in Chile. The survey is called the VST Photometric $H\alpha$ Survey of the Southern Galactic Plane and Bulge (VPHAS+, Drew et al. 2014). At the time of writing, the survey has completed 19% of its intended footprint. The main survey strip is 10 degrees wide and is defined in Galactic coordinates as all latitudes within 5 degrees of the Galactic Equator (GE). There are two Bulge extensions that expand this latitude range to 10 degrees away from the GE. It takes a tiling of 2269 OmegaCam fields to cover the ~ 2000 sq.deg footprint. This survey will provide an ideal opportunity to repeat the search I undertook with IPHAS for shells around known CVs. However, this will only cover the footprint of VPHAS so it would also be worthwhile attempting to search all CVs in the southern sky that were not accessible from La Palma. There are more CVs located towards the Galactic centre so this would likely require significant time (of the order of ~ 10 days) on a >2 m telescope.

A number of programmes are underway to digitise old photographic surveys (e.g. the Harvard plate collection - see Grindlay et al. 2012) that will provide a large suite of historical lightcurves. These will possibly reveal previously unrecorded nova explosions, which I could follow up with deep $H\alpha$ imaging to search for nova shells.

Boris Gänsicke (private communication) has pointed out that an old IUE spectrum of V1315 Aql shows that that WD temperature is quite low, compared to what would be expected following a nova eruption, which might cast doubt on whether a nova eruption occurred. However, the IUE spectrum was of low quality. I am planning to apply for

HST time to obtain a more detailed UV spectrum to derive a better measurement of the WD temperature.

Another approach to investigate the nova-induced cycle theory is to examine the mass transfer rate of old novae. The theory predicts that the mass transfer rate in a CV will vary following the nova event, and perhaps switch off completely. Hence the magnitude of the system will vary. An ongoing campaign, led by Claus Tappert at the University of Valparaíso, Chile, has reported its initial findings. They found that most post-nova systems have high mass transfer rates at NL levels (Tappert et al., 2015), supporting the theory that the secondary is bloated by the heated WD, despite the widening of the binary separation.

Further work is needed to monitor these post-nova systems to establish whether the predicted variation in mass transfer rates is observed. Data collated by Shara et al. (2018) shows that mass transfer rates in classical and recurrent novae drop to DN levels. However, there are many systems that show the opposite behaviour i.e. the mass transfer rate increases after the nova event. Ashley Pagnotta at the American Museum of Natural History, USA, is undertaking a project to derive long term light curves, and hence mass transfer rates, for as many Galactic novae as possible (Pagnotta, 2017). This will provide a much more statistically significant dataset than has been available previously.

Bibliography

- Ak T., Bilir S., Ak S., Retter A., 2007, *New Astronomy*, 12, 446
- Amaro-Seoane P., Audley H., Babak S. e. a., 2017, ArXiv e-prints
- Andersen P., Hjorth J., 2018, ArXiv e-prints 1801.00793
- Anupama G. C., 2008, *PASP*, 401, 31
- Anupama G. C., Prabhu T. P., 1993, *MNRAS*, 263, 335
- Badenes C., Hughes J. P., Bravo E., Langer N., 2007, *ApJ*, 662, 472
- Badenes C., Maoz D., 2012, *ApJ*, 749, L11
- Baldry I. K., Glazebrook K., 2003, *ApJ*, 593, 258
- Balman Ş., Yılmaz A., Retter A., Saygıç T., Esenoglu H., 2005, *MNRAS*, 356, 773
- Barentsen G., Farnhill H. J., Drew J. E., González-Solares E. A., Greimel R., Irwin M. J., Miszalski B., Ruhland C., Groot P., Mampaso A., Sale S. E., Henden A. A., Aungwerojwit A., Barlow M. J., Carter P. J., Corradi R. L. M., et al., 2014, *MNRAS*, 444, 3230
- Barnes T., Evans D., 1976, *MNRAS*, 174, 489
- Bayo A., Rodrigo C., Barrado Y Navascués D., Solano E., Gutiérrez R., Morales-Calderón M., Allard F., 2008, *A&A*, 492, 277
- Becker H. J., Duerbeck H. W., 1980, *PASP*, 92, 792
- Bianchi L., 2014, *Ap&SS*, 354, 103
- Bloom J. S., Kasen D., Shen K. J., Nugent P. E., Butler N. R., Graham M. L., Howell D. A., Kolb U., Holmes S., Haswell C. A., Burwitz V., Rodriguez J., Sullivan M., 2012, *ApJ*, 744, L17
- Bode M. F., Evans A., 2008, *Classical Novae*. Cambridge University Press
- Brown P. J., Dawson K. S., de Pasquale M., Gronwall C., Holland S., Immler S., Kuin P., Mazzali P., Milne P., Oates S., Siegel M., 2012, *ApJ*, 753, 22
- Büning A., Ritter H., 2004, *A&A*, 423, 281
- Campbell C. G., Schwobe A. D., 1999, *A&A*, 343, 136

- Chiosi E., Chiosi C., Trevisan P., Piovan L., Orio M., 2015, MNRAS, 448, 2100
- Claret A., Bloemen S., 2011, A&A, 529, A75
- Collazzi A. C., Schaefer B. E., Xiao L., Pagnotta A., Kroll P., Löchel K., Henden A. A., 2009, AJ, 138, 1846
- Corradi R. L. M., García-Rojas J., Jones D., Rodríguez-Gil P., 2015, ApJ, 803, 99
- Darnley M. J., Bode M. F., Kerins E., Newsam A. M., An J., Baillon P., Belokurov V., Calchi Novati S., Carr B. J., Crézé M., Evans N. W., Giraud-Héraud Y., Gould A., et al., 2006, MNRAS, 369, 257
- Darnley M. J., Henze M., Bode M. F., Hachisu I., Hernanz M., Hornoch K., Hounsell R., Kato M., Ness J.-U., Osborne J. P., Page K. L., Ribeiro V. A. R. M., Rodríguez-Gil P., Shafter A. W., Shara M. M., Steele I. A., et al., 2016, ApJ, 833, 149
- della Valle M., Bianchini A., Livio M., Orio M., 1992, A&A, 266, 232
- Dhillon V. S., Marsh T. R., Jones D. H. P., 1991, MNRAS, 252, 342
- Dhillon V. S., Marsh T. R., Jones D. H. P., Smith R. C., 1992, MNRAS, 258, 225
- Dhillon V. S., Rutten R. G. M., 1995, MNRAS, 277, 777
- Downes A. R., Matteo M., Szkody P., Jenner D. C., Margon B., 1986, ApJ, 301, 240
- Downes R. A., Duerbeck H. W., 2000, ApJ, 120, 2007
- Downes R. A., Duerbeck H. W., Delahodde C. E., 2001, Journal of Astronomical Data, 7, 6
- Drew J. E., Gonzalez-Solares E., Greimel R., Irwin M. J., Küpcü Yoldas A., Lewis J., Barentsen G., Eislöffel J., Farnhill H. J., Martin W. E., Walsh J. R., Walton N. A., Mohr-Smith M., Raddi R., Sale S. E. e. a., 2014, MNRAS, 440, 2036
- Drew J. E., Greimel R., Irwin M. J., Aungwerojwit A., Barlow M. J., Corradi R. L. M., Drake J. J., Gänsicke B. T., Groot P., Hales A., Hopewell E. C., Irwin J., Knigge C., Leisy P., Lennon D. J., Mampaso A., Masheder M. R. W. ., et al., 2005, MNRAS, 362, 753
- Dubus G., Otulakowska-Hypka M., Lasota J.-P., 2018, ArXiv e-prints 1805.02110
- Ducati J., Bevilacqua C., Rembold S., Ribeiro D., 2001, ApJ, 558, 309
- Duerbeck H. W., 1987, Space Sci. Rev., 45, 1
- Duerbeck H. W., 1987, The ESO Messenger, 50, 8
- Duerbeck H. W., Seitter W. C., 1987, Astrophys. Sp. Sci., 131, 467
- Eggleton P. P., 1983, ApJ, 268, 368

- Faber S. M., Phillips A. C., Kibrick R. I., Alcott B., Allen S. L., Burrous J., Cantrall T., Clarke D., Coil A. L., Cowley D. J., Davis M., Deich W. T. S., Dietsch K., Gilmore D. K., Harper C. A., Hilyard D. F. e. a., 2003, in Iye M., Moorwood A. F. M., eds, *Instrument Design and Performance for Optical/Infrared Ground-based Telescopes* Vol. 4841 of *Proc. SPIE*. p. 1657
- Gänsicke B. T., Araujo-Betancor S., Hagen H. J., Harlaftis E. T., Kitsionas S., Dreizler S., Engels D., 2004, *A&A*, 418, 265
- Gänsicke B. T., Dillon M., Southworth J., Thorstensen J. R., Rodríguez-Gil P., Aungwerojwit A., Marsh T. R., Szkody P., Barros S. C. C., Casares J., de Martino D., Groot P. J., Hakala P., Kolb U., Littlefair S. P., Martínez-Pais I. G., et al., 2009, *MNRAS*, 397, 2170
- Gill C. D., O'Brien T. J., 1998, *MNRAS*, 300, 221
- Goldstein D. A., Kasen D., 2018, *ApJ*, 852, L33
- Gray D. F., 1992, *The Observation and Analysis of Stellar Photospheres*. Cambridge University Press, Cambridge
- Gray R. O., Corbally C. J., 2009, *Stellar Spectral Classification*. Princeton University Press, Princeton
- Greiner J., Alcalá J., Wenzel W., 1996, *Inf. Bull. Var. Stars*, 4338, 1
- Grindlay J., Tang S., Los E., Servillat M., 2012, in *New Horizons in Time-Domain Astronomy, Proceedings of the International Astronomical Union, IAU Symposium, Volume 285*, p. 29-34 Vol. 285, *Opening the 100-Year Window for Time-Domain Astronomy*. p. 29
- Guerrero M. A., Sabin L., Tovmassian G., Santamaría E., Michel R., Ramos-Larios G., Alarie A., Morisset C., Bermúdez Bustamante L. C., González C. P., Wright N. J., 2018, *ApJ*, 857, 80
- Hachisu I., Kato M., 2003, *ApJ*, 588, 1003
- Hachisu I., Kato M., 2018, *ArXiv e-prints* 1805.09932
- Hachisu I., Kato M., Nomoto K., 1999, *ApJ*, 522, 487
- Hachisu I., Kato M., Nomoto K., 2008a, *ApJ*, 679, 1390
- Hachisu I., Kato M., Nomoto K., 2008b, *ApJ*, 683, 127
- Hachisu I., Kato M., Schaefer B., 2003, *ApJ*, 584, 1008
- Hamuy M., Phillips M. M., Suntzeff N. B., Maza J., González L. E., Roth M., Krisciunas K., Morrell N., Green E. M., Persson S. E., McCarthy P. J., 2003, *Nat*, 424, 651
- Han Z., Podsiadlowki P., 2004, *MNRAS*, 350, 1301

- Hardy L. K., Butterley T., Dhillon V. S., Littlefair S. P., Wilson R. W., 2015, *MNRAS*, 454, 4316
- Harman D. J., O'Brien T. J., 2003, *MNRAS*, 344, 1219
- Harvey E., Redman M. P., Boumis P., Akras S., 2016, *A&A*, 595, A64
- Harvey E. J., 2017, PhD thesis, NUI Galway
- Hillman Y., Prialnik D., Kovetz A., Shara M. M., 2016, *AJ*, 819, 168
- Hillman Y., Prialnik D., Kovetz A., Shara M. M., Neill J. D., 2014, *MNRAS*, 437, 1962
- Horesh A., Kulkarni S., Fox D., Carpenter J., Kasliwal M., Ofek E., Quimby R., Gal-Yam A., Cenko S., de Bruyn A., Kamble A., Wijers R., van der Horst A., Kouveliotou C., Podsiadlowski P., Sullivan M., Maguire K., Howell D., Nugent P., Gehrels N., Others ., 2012, *ApJ*, 746, 21
- Horne K., Lanning H. H., Gomer R. H., 1982, *ApJ*, 252, 681
- Horne K., Marsh T. R., 1986, *MNRAS*, 218, 761
- Horne K., Welsh W. F., Wade R. A., 1993, *ApJ*, 410, 357
- Hoyle F., Fowler W. A., 1960, *ApJ*, 132, 565
- Iijima T., 2012, *A&A*, 544, A26
- Ilkov M., Soker N., 2012, *MNRAS*, 419, 1695
- Ivanova N., Taam R. E., 2004, *ApJ*, 601, 1058
- Kapteyn J. C., 1901, *Astron. Nachr.*, 157, 201
- Kerzendorf W. E., Schmidt B. P., Asplund M., Nomoto K., Podsiadlowski P., Frebel A., Fesen R. A., Yong D., 2009, *ApJ*, 701, 1665
- King R. R., Goodwin S. P., Parker R. J., Patience J., 2012, *MNRAS*, 427, 2636
- Kiss L. L., Gogh N., Vinkó J., Furész G., Csák B., DeBond H., Thomson J. R., Derekas A., 2002, *A&A*, 384, 982
- Knigge C., 2006, *MNRAS*, 373, 484
- Knigge C., Baraffe I., Patterson J., 2011, *ApJS*, 194, 28
- Knigge C., King A. R., Patterson J., 2000, *A&A*, 364, L75
- Kopal Z., 1959, *Close binary systems. The International Astrophysics Series*, London: Chapman & Hall, 1959
- Korol V., Koop O., Rossi E. M., 2018, *ArXiv e-prints*, p. arXiv:1808.05959
- Kozai Y., 1962, *AJ*, 67, 591

- Kushnir D., Katz B., Dong S., Livne E., Fernández R., 2013, *ApJ*, 778
- Langer N., Deutschmann A., Wellstein S., Höflich P., 2000, *A&A*, 362, 1046
- Lederle C., Kimeswenger S., 2003, *A&A*, 397, 951
- Leonard D. C., 2007, *ApJ*, 670, 1275
- Lidov M., 1961, *Artificial Earth Satellites*, 8
- Liimets T., Corradi R. L. M., Santander-García M., Villaver E., Rodríguez-Gil P., Verro K., Kolka I., 2012, *ApJ*, 761, 34
- Littlefair S. P., Dhillon V. S., Marsh T. R., Gänsicke B. T., 2006, *MNRAS*, 371, 1435
- Livio M., Mazzali P., 2018, *ArXiv e-prints* 1802.03125
- Livio M., Pringle J. E., 1994, *ApJ*, 427, 956
- Livio M., Riess A., 2003, *ApJ*, 594, L94
- Lynch D., Wilson J. C., Rudy R. J., Venturini C., Mazuk S., Miller N. A., Puetter R. C., 2004, *AJ*, 127, 1089
- Maoz D., Hallakoun N., Badenes C., 2018, *MNRAS*, 476, 2584
- Marsh T. R., 1988, *MNRAS*, 231, 1117
- Marsh T. R., 2000, in Boffin H., Steeghs D., Cuypers J., eds, *Astrotopography - Indirect Imaging Methods in Observational Astronomy* Springer-Verlag, Berlin
- Marsh T. R., Horne K., 1988, *MNRAS*, 235, 269
- Marsh T. R., Oke J. B., Wade R. A., 1983, *MNRAS*, 205, 33P
- Marsh T. R., Robinson E. L., Wood J. H., 1994, *MNRAS*, 266, 137
- Mason E., Shore S. N., De Gennaro Aquino I., Izzo L., Page K., Schwarz G. J., 2018, *ApJ*, 853, 27
- Miszalski B., Woudt P. A., Littlefair S. P., Warner B., Boffin H. M. J., Corradi R. L. M., Jones D., Motsoaledi M., Rodríguez-Gil P., Sabin L., Santander-García M., 2016, *MNRAS*, 456, 633
- Mizuno D. R., Kraemer K. E., Flagey N., Billot N., Shenoy S., Paladini R., Ryan E., Noriega-Crespo A., Carey S. J., 2010, *AJ*, 139, 1542
- Moraes M., Diaz M., 2009, *AJ*, 138, 1541
- Morris S. L., Naftilan S. A., 1993, *AJ*, 419, 344
- Mróz P., Udalski A., Pietrukowicz P., Szymański M. K., Soszyński I., Wyrzykowski L., Poleski R., Kozłowski S., Skowron J., Ulaczyk K., Skowron D., Pawlak M., 2016, *Nature*, 537, 649

- Mukai K., Naylor T., 1995, in Cataclysmic Variables, Proceedings of the conference held in Abano Terme, Italy, 20-24 June 1994 Publisher: Dordrecht Kluwer Academic Publishers, 1995. Edited by A. Bianchini, M. della Valle, and M. Orio. Astrophysics and Space Science Library Vol. 205. p. 517
- Nakamura A., Tago A., Abe H., 2001, IAU Circ., 7686, 2
- Napiwotzki R., Karl C. A., Nelemans G., Yungelson L., Christlieb N., Drechsel H., Heber U., Homeier D., Koester D., Leibundgut B., Marsh T. R., Moehler S., Renzini A., Reimers D., 2007, in ASP Conf. Ser. 372 p. 387
- Naylor T., Charles P. A., Mukai K., Evans A., 1992, MNRAS, 258, 449
- Nomoto K., Leung S.-C., 2018, Space Sci. Rev., 214, 67
- Nugent P. E., Sullivan M., Cenko S. B., Thomas R. C., Kasen D., Howell D. A., Bersier D., Bloom J. S., Kulkarni S. R., Kandrashoff M. T., Filippenko A. V., Silverman J. M., Marcy G. W., Howard A. W., Isaacson H. T., Maguire K., Suzuki N., Others., 2011, Nat, 480, 344
- Osaki Y., 1974, Pub. Astr. Soc. Japan, 26, 429
- Osterbrock D. E., 1989, Astrophysics of gaseous nebulae and active galactic nuclei. University Science Books, Sausalito, California
- Paczynski B., 1971, Ann Rev Astr Astrophys, 9, 183
- Paczynski B., 1976, in Eggleton P. P., Mitton S., J. W. J. A., eds, Structure and Evolution of Close Binary Systems Reidel, Dordrecht, p. 75
- Pagnotta A., 2015, Acta Polytechnica CTU Proceedings, 2, 199
- Pagnotta A., 2017, in Tremblay P. E., Gaensicke B., Marsh T., eds, 20th European White Dwarf Workshop Vol. 509. p. 535
- Pagnotta A., Schaefer B. E., 2014, ApJ, 788, 164
- Pagnotta A., Zurek D., 2016, MNRAS, 458, 1833
- Pakmor R., Kromer M., Taubenberger S., Springel V., 2013, ApJ, 770, L8
- Patat F., Hallakoun N., 2018, ArXiv e-prints 1805.03207
- Patterson J., Kemp J., Harvey D. A., Fried R. E., Rea R., Monard B., Cook L. M., Skillman D. R., Vanmunster T., Bolt G., Armstrong E., McCormick J., Krajci T., Jensen L., Gunn J., Butterworth N., Foote J., Bos M., Masi G., Warhurst P., 2005, PASP, 117, 1204
- Patterson J., Thorstensen J. R., Fried R., Skillman D. R., Cook L. M., Jensen L., 2001, PASP, 113, 72

- Patterson J., Uthas H., Kemp J., de Miguel E., Krajci T., Foote J., Hambusch F.-J., Campbell T., Roberts G., Cejudo D., Dvorak S., Vanmunster T., Koff R., Skillman D., Harvey D., Martin B., Rock J., Boyd D., Oksanen A., Morelle E., Ulowetz J., Kroes A., Sabo R., Jensen L., 2013, *MNRAS*, 434, 1902
- Payne-Gaposchkin C., 1957, *The Galactic Novae*. Amsterdam: North-Holland Pub. Co.
- Perlmutter S., Aldering G., Goldhaber G., Knop R. A., Nugent P., Castro P. G., Deustua S., Fabbro S., Goobar A., Groom D. E., Hook I. M., Kim A. G., Kim M. Y., Lee J. C., Nunes N. J., Pain R., Pennypacker C. R., Quimby R., Lidman C., Others ., 1999, *ApJ*, 517, 565
- Phillips M. M., 1993, *ApJ*, 413, L105
- Pickles A. J., 1998, *PASP*, 110, 863
- Politano M., 1996, *ApJ*, p. 338
- Rappaport S., Joss P. C., Verbunt F. A., 1983, *ApJ*, 275, 713
- Reiners A., Basri G., 2008, *ApJ*, 684, 1390
- Reinmuth K., 1925, *Astron. Nachr.*, 225, 385
- Ribeiro V. A. R. M., Bode M. F., Darnley M. J., Barnsley R. M., Munari U., Harman D. J., 2013, *MNRAS*, 433, 1991
- Ribeiro V. A. R. M., Bode M. F., Williams R. E., 2014, in Woudt P. A., Ribeiro V. A. R. M., eds, *Stellar Novae: Past and Future Decades Vol. 490 of Astronomical Society of the Pacific Conference Series*. p. 123
- Ribeiro V. A. R. M., Darnley M. J., Bode M. F., Munari U., Harman D. J., Steele I. A., Meaburn J., 2011, *MNRAS*, 412, 1701
- Ribeiro V. A. R. M., Munari U., Valisa P., 2013, *ApJ*, 768, 49
- Riess A., Filippenko A., Challis P., Clocchiatti A., Diercks A., Garnavich P., Gilliland R., Hogan C., Jha S., Kirshner R., Leibundgut B., Phillips M. M., Reiss D., Schmidt B., Schommer R., Smith R., Spyromilio J., Stubbs C., Suntzeff N., Tonry J., 1998, *AJ*, 116, 1009
- Ritter H., Kolb U., 2003, *A&A*, 404, 301, (Update RKCcat 7.20, 2013)
- Rodríguez-Gil P., Santander-García M., Knigge C., Corradi R. L. M., Gänsicke B. T., Barlow M. J., Drake J. J., Drew J., Miszalski B., Napiwotzki R., Steeghs D., Wesson R., Zijlstra A. A., Jones D., Liimets T., Others 2010, *MNRAS*, 407, L21
- Rosswog S., Ramirez-Ruiz E., Hix W. R., 2009, in *Journal of Physics: Conference Series*, Volume 172, Issue 1, id. 012036.
- Rutten R. G. M., van Paradijs J., Tinbergen J., 1992, *A&A*, 260, 213

- Ryan S., Norton A., 2010, *Stellar Evolution and Nucleosynthesis*. Cambridge University Press
- Sahman D. I., Dhillon V. S., Carlisle C., Erram R., Lopez F., Diaz Alfaro M., Vaduvescu O., Sowicka P., Humphries N., Peralta de Arriba L., Stevance H., 2018, in preparation
- Sahman D. I., Dhillon V. S., Knigge C., Marsh T. R., 2015, *MNRAS*, 451, 2863
- Sahman D. I., Dhillon V. S., Littlefair S. P., Hallinan G., 2018, *MNRAS*, 477, 4483
- Sahman D. I., Dhillon V. S., Marsh T. R., Moll S., Thoroughgood T. D., Watson C. A., Littlefair S. P., 2013, *MNRAS*, 433, 1588
- Sato Y., Nakasato N., Tanikawa A., Nomoto K., Maeda K., Hachisu I., 2015, *AJ*, 807, 105
- Schaefer B. E., 2001, *IAU Circ.*, 7750, 2
- Schaefer B. E., 2010, *ApJS*, 187, 275
- Schaefer B. E., 2011, *ApJ*, 742, 112
- Schaefer B. E., 2014, in *American Astronomical Society Meeting Abstracts #224* p. 306.04
- Schaefer B. E., Pagnotta A., 2012, *Nat*, 481, 164
- Schirmer M., 2013, *ApJS*, 209, 21
- Schmidtobreick L., Shara M., Tappert C., Bayo A., Ederoclite A., 2015, *MNRAS*, 449, 2215
- Schneider D. P., Young P. J., 1980, *ApJ*, 238, 946
- Schreiber M. R., Zorotovic M., Wijnen T. P. G., 2016, *MNRAS*, 455, L16
- Shafter A. W., 2017, *ApJ*, 834, 196
- Shafter A. W., Henze M., Rector T. A., Schweizer F., Hornoch K., Orio M., Pietsch W., Darnley M. J., Williams S. C., Bode M. F., Bryan J., 2015, *ApJS*, 216, 34
- Shafter A. W., Kundu A., Henze M., 2017, *Research Notes of the American Astronomical Society*, 1, 11
- Shafter A. W., Szkody P., Thorstensen J. R., 1986, *ApJ*, 308, 765
- Shara M. M., Doyle T. F., Lauer T. R., Zurek D., Neill J. D., Madrid J. P., Mikolajewska J., Welch D. L., Baltz E. A., 2016, *ApJS*, 227, 1
- Shara M. M., Drissen L., Martin T., Alarie A., Stephenson F. R., 2017, *MNRAS*, 465, 739

- Shara M. M., Ikkiewicz K., Mikołajewska J., Pagnotta A., Bode M. F., Crause L. A., Drozd K., Faherty J., Fuentes-Morales I., Grindlay J. E., Moffat A. F. J., Pretorius M. L., Schmidtobreick L., Stephenson F. R., Tappert C., Zurek D., 2017, *Nat*, 548, 558
- Shara M. M., Livio M., Moffat A. F. J., Orio M., 1986, *ApJ*, 311, 163
- Shara M. M., Martin C. D., Seibert M., Rich R. M., Salim S., Reitzel D., Schiminovich D., Deliyannis C. P., Sarrazine A. R., Kulkarni S. R., Ofek E. O., Brosch N., Lépine S., Zurek D., De Marco O., Jacoby G., 2007, *Nat*, 446, 159
- Shara M. M., Mizusawa T., Wehinger P., Zurek D., Martin C. D., Neill J. D., Forster K., Seibert M., 2012, *ApJ*, 758, 121
- Shara M. M., Potter M., Williams R. E., Cohen J., 1989, *ApJ*, 337, 720
- Shara M. M., Prialnik D., Hillman Y., Kovetz A., 2018, *ApJ*, 860, 110
- Shara M. M., Zurek D., De Marco O., Mizusawa T., Williams R., Livio M., 2012, *AJ*, 143, 143
- Shen K. J., Bildsten L., 2007, *ApJ*, 660, 1444
- Shen K. J., Bildsten L., Kasen D., Quataert E., 2012, *ApJ*, 748, 35
- Shen K. J., Guillochon J., Foley R. J., 2013, *ApJ*, 770, L35
- Sim S. A., Fink M., Kromer M., Röpke F. K., Ruiter A. J., Hillebrandt W., 2012, *MNRAS*, 420, 3003
- Simon J. D., Gal-Yam A., Gnat O., Quimby R. M., Ganeshalingam M., Silverman J. M., Blondin S., Li W., Filippenko A. V., Wheeler J. C., Kirshner R. P., Patat F., Nugent P., Foley R. J., Vogt S. S., Butler R. P., Others ., 2009, *ApJ*, 702, 1157
- Simonsen M., Boyd D., Goff W., Krajci T., Menzies K., Otero S., Padovan S., Poyner G., Roe J., Sabo R., Sjöberg G., Staels B., Stubbings R., Toone J., Wils P., 2014, *Journal of the American Association of Variable Star Observers (JAAVSO)*, 42, 177
- Skrutskie M. F., Cutri R. M., Stiening R., Weinberg M. D., Schneider S., Carpenter J. M., Beichman C., Capps R., Chester T., Elias J., Huchra J., Liebert J., Lonsdale C., Monet D. G., Price S., Seitzer P., Jarrett T., Others ., 2006, *ApJ*, 131, 1163
- Slavin A. J., O'Brien T. J., Dunlop J. S., 1995, *MNRAS*, 276, 353
- Smith D. A., Dhillon V. S., 1998, *MNRAS*, 301, 767
- Smith D. A., Dhillon V. S., Marsh T. R., 1998, *MNRAS*, 296, 465
- Sokoloski J. L., Crotts A. P. S., Lawrence S., Uthas H., 2013, *ApJ*, 770, L33
- Solheim J. E., 2010, *Publications of the Astronomical Society of the Pacific*, 122, 1133

- Somers M. W., Mukai K., Naylor T., Ringwald F. A., 1996, in Cataclysmic variables and related objects. Astrophysics and Space Science Library; Proceedings of the 158th colloquium of the International Astronomical Union (IAU); held at Keele; United Kingdom; June 26-30; 1995; Dordrecht: Kluwer Academic Publishers; edited by A. Evans and Janet H. Wood Vol. 208. p. 327
- Somers M. W., Ringwald F. A., Naylor T., 1997, MNRAS, 284, 359
- Starrfield S., Iliadis C., Timmes F. X., Hix W. R., Arnett W. D., Meakin C., Sparks W. M., 2012, Bulletin of the Astronomical Society of India, 40, 419
- Stephenson F. R., 1976, QJRAS, 17, 121
- Stockman H. S., Schmidt G. D., Lamb D. Q., 1988, ApJ, 332, 282
- Strope R. J., Schaefer B. E., Henden A. A., 2010, AJ, 140, 34
- Swope H. H., 1940, Harvard College Observatory Bulletin, 913, 11
- Takamizawa K., Kato T., Yamamoto M., 2000, IAU Circ., 7409, 1
- Tappert C., Ederoclite A., Schmidtbreick L., Vogt N., 2015, Acta Polytechnica CTU Proceedings, 2, 230
- Thoroughgood T. D., Dhillon V., Littlefair S., 2001, MNRAS, 327, 1323
- Thoroughgood T. D., Dhillon V., Watson C., Buckley D., Steeghs D., Stevenson M., 2004, MNRAS, 353, 1135
- Thorstensen J. R., Schwarz R., Schwope A. D., Staude A., Vogel J., Krumpel M., Kohnert J., Nebot Gómez-Morán A., 2009, Publications of the Astronomical Society of the Pacific, 121, 465
- Uthas H., 2011, PhD thesis
- Vaytet N. M. H., O'Brien T. J., Rushton A. P., 2007, MNRAS, 380, 175
- Verbunt F., Zwaan C., 1981, A&A, 100, L7
- Wade R. A., Ciardullo R., Jacoby G. H., Sharp N. A., 1991, AJ, 102, 1738
- Warner B., 1995, Cataclysmic Variable Stars. Cambridge University Press, Cambridge
- Wesson R., Barlow M. J., Corradi R. L. M., Drew J. E., Groot P. J., Knigge C., Steeghs D., Gaensicke B. T., Napiwotzki R., Rodriguez-Gil P., Zijlstra A. A., Bode M. F., Drake J. J., Frew D. J., Gonzalez-Solares E. A., et al., 2008, ApJ, 688, L21
- Whelan J., Iben I., 1973, ApJ, 186, 1007
- Williams R., 2013, AJ, 146, 55
- Williams R. E., 1992, AJ, 104, 725
- Wilson R. E., Honeycutt R. K., 2014, ApJ, 795, 8

- Wright E. L., Eisenhardt P. R. M., Mainzer A. K., Ressler M. E., Cutri R. M., Jarrett T., Kirkpatrick J. D., Padgett D., McMillan R. S., Skrutskie M., Stanford S. A., Cohen M., Walker R. G., Mather J. C., Leisawitz D., Gautier III T. N., McLean I. e. a., 2010, *AJ*, 140, 1868
- Yamaoka H., Shirakami K., 2000, *IAU Circ.*, 7411, 1
- Yaron O., Prialnik D., Shara M. M., Kovetz A., 2005, *ApJ*, 623, 398
- Zhou W.-H., Wang B., Meng X.-C., Liu D.-D., Zhao G., 2015, *Research in Astronomy and Astrophysics*, 15
- Zorotovic M., Schreiber M. R., Parsons S. G., Gänsicke B. T., Hardy A., Agurto-Gangas C., Nebot Gómez-Morán A., Rebassa-Mansergas A., Schwobe A. D., 2016, *MNRAS*, 457, 3867

Appendix A

WHT Nova shell images (in
alphabetical order of constellation)

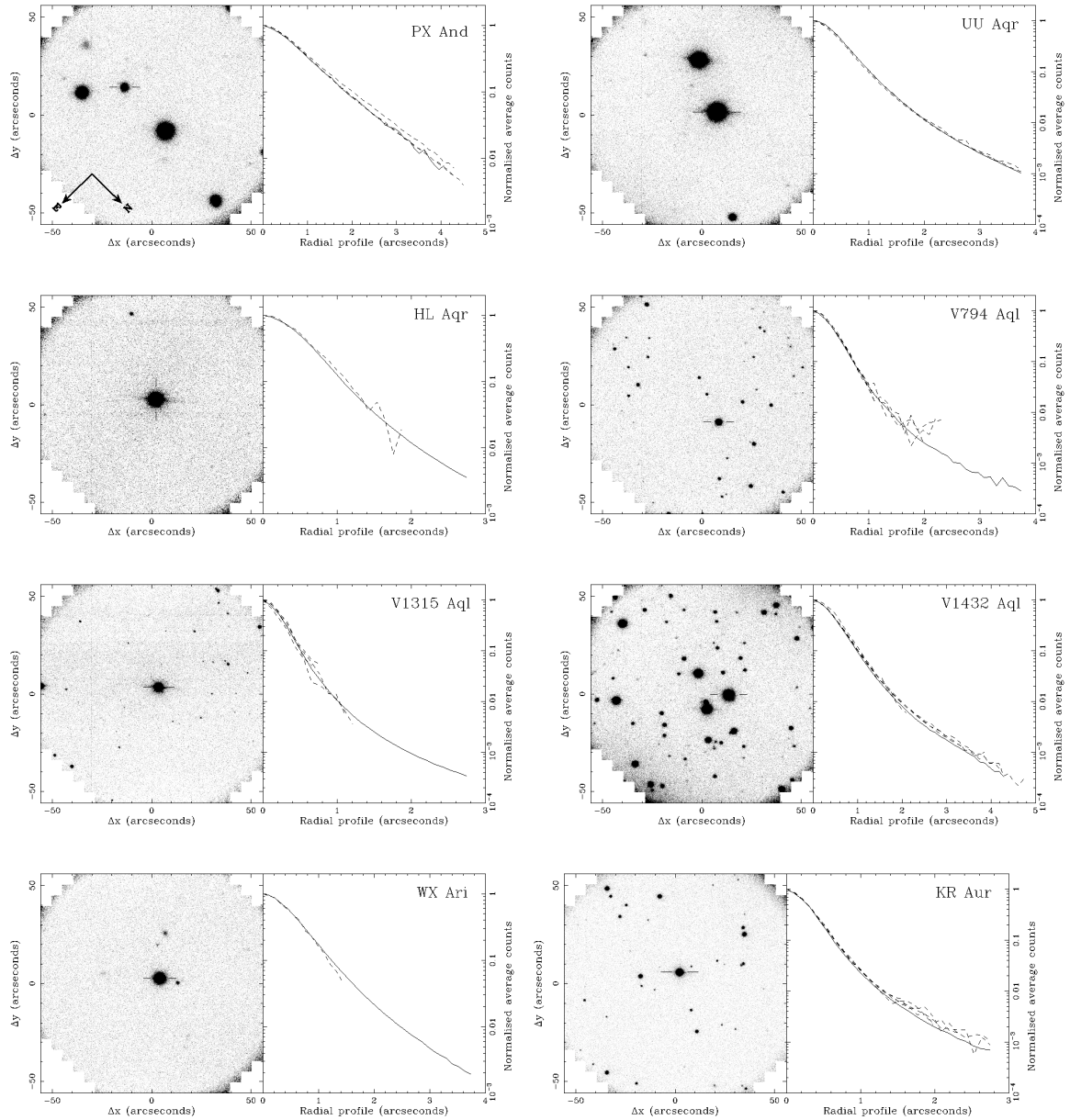


Figure A.1: WHT images of our target CVs (left) and the associated radial profiles (right); the solid line is the radial profile of the CV and the dashed lines are field stars. The radial profiles are normalised to unity and plotted until they reach 1σ above the background level. The CVs are marked by bars and are located towards the centres of the images. The orientation of all images is the same, and is shown in the image of PX And.

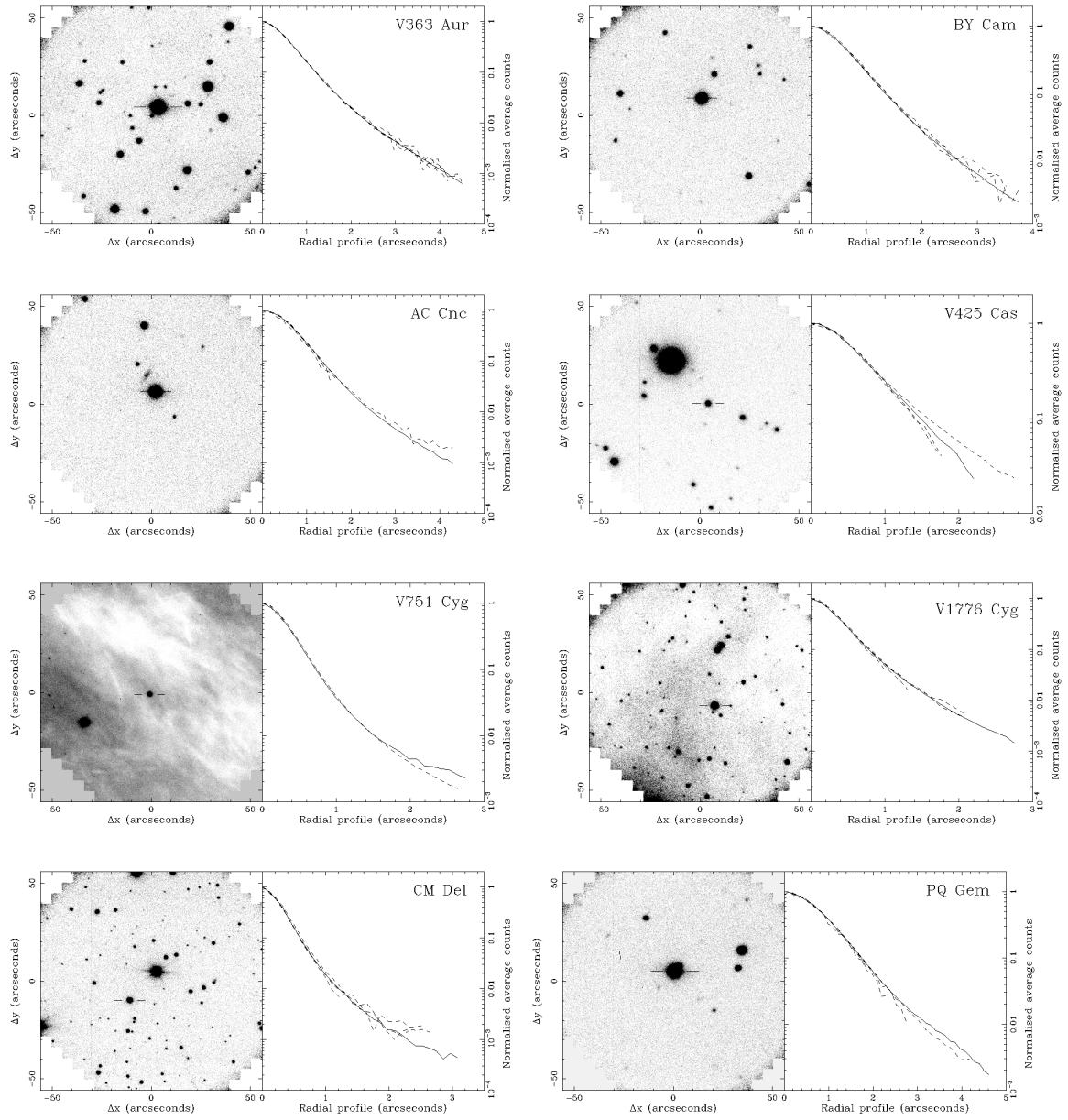


Figure A.2: See caption to Figure A.1 for details.

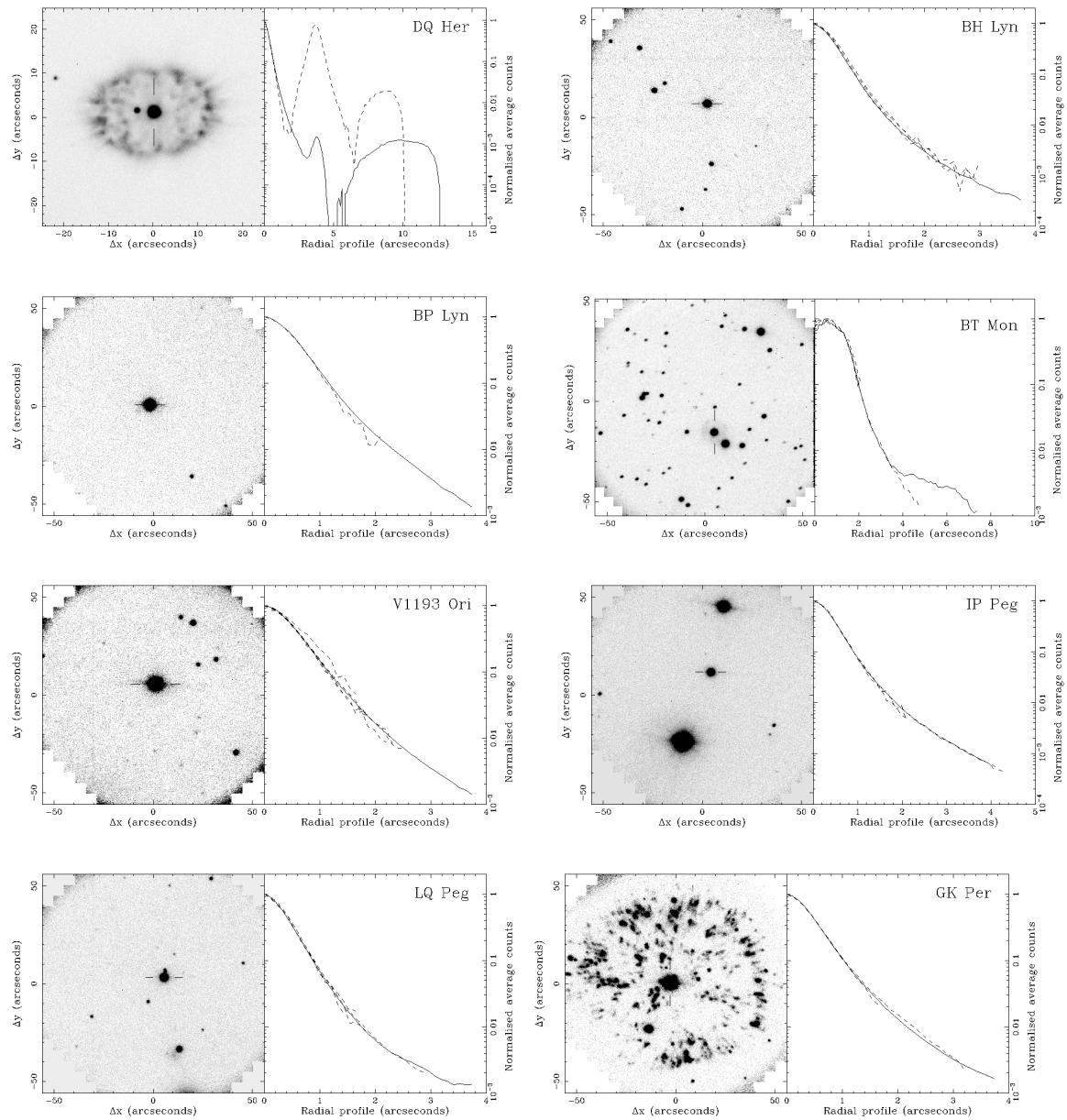


Figure A.3: See caption to Figure A.1 for details.

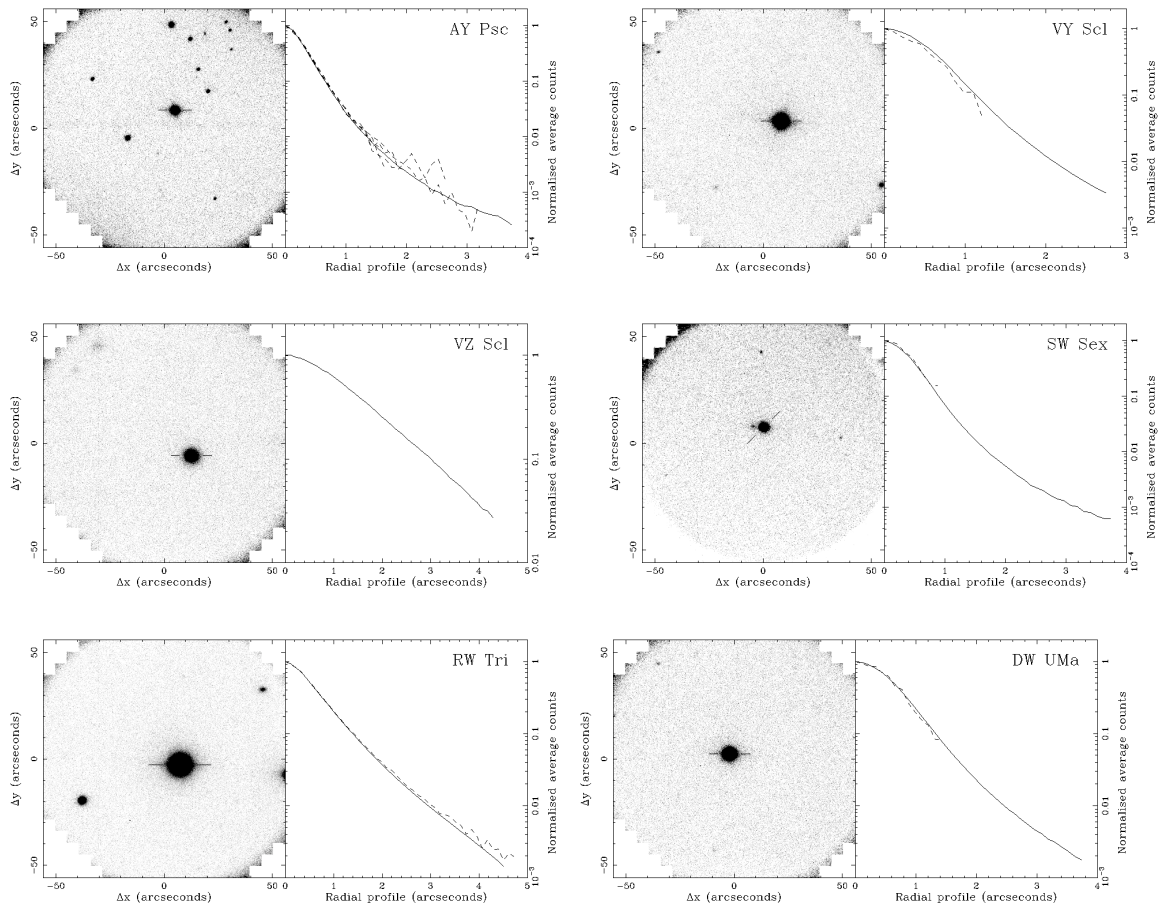


Figure A.4: See caption to Figure A.1 for details.

Appendix B

INT Nova shell images (in
alphabetical order of constellation)

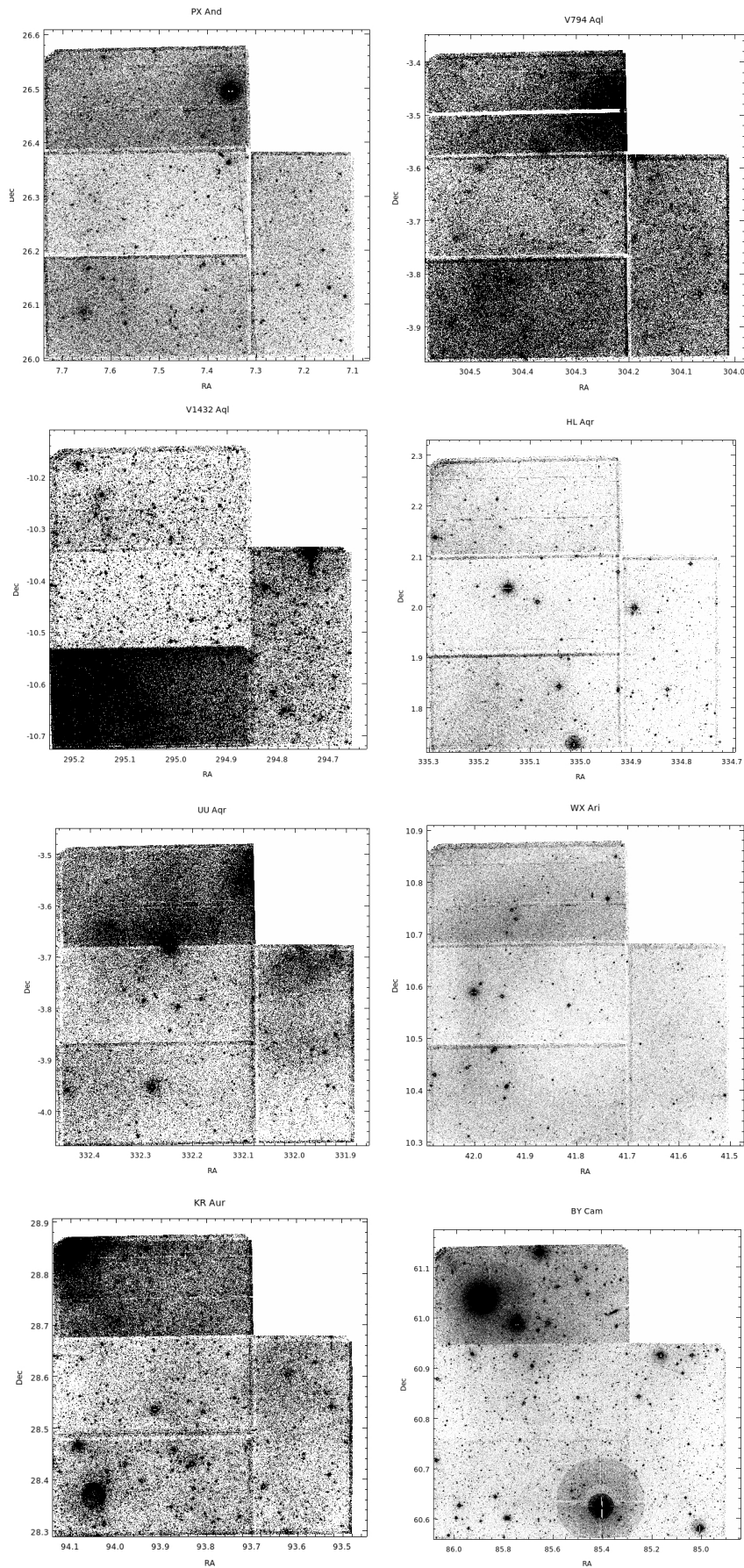


Figure B.1: INT images of our target CVs in order of constellation. In all images, North is up and East is left.

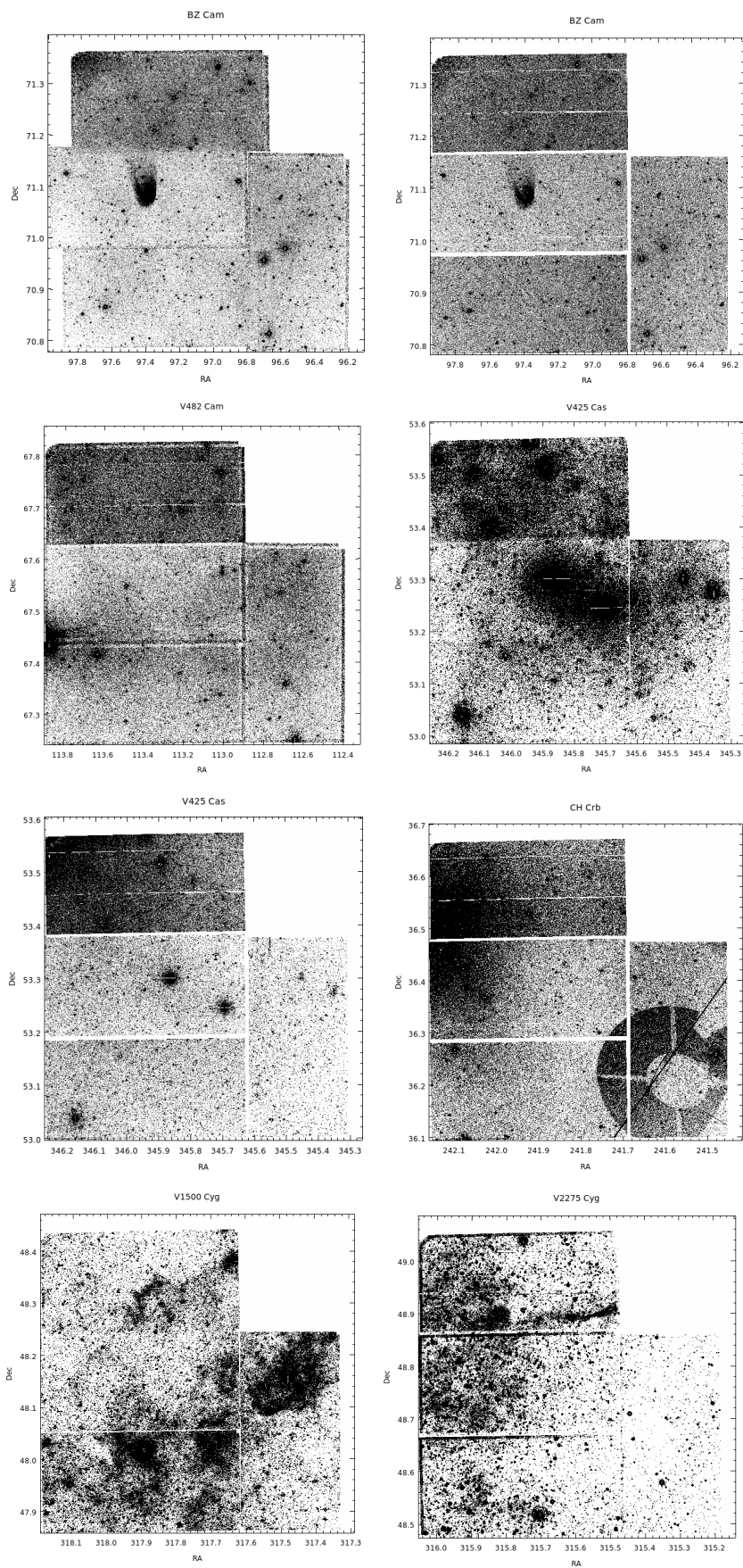


Figure B.2: See caption to Figure B.1 for details.

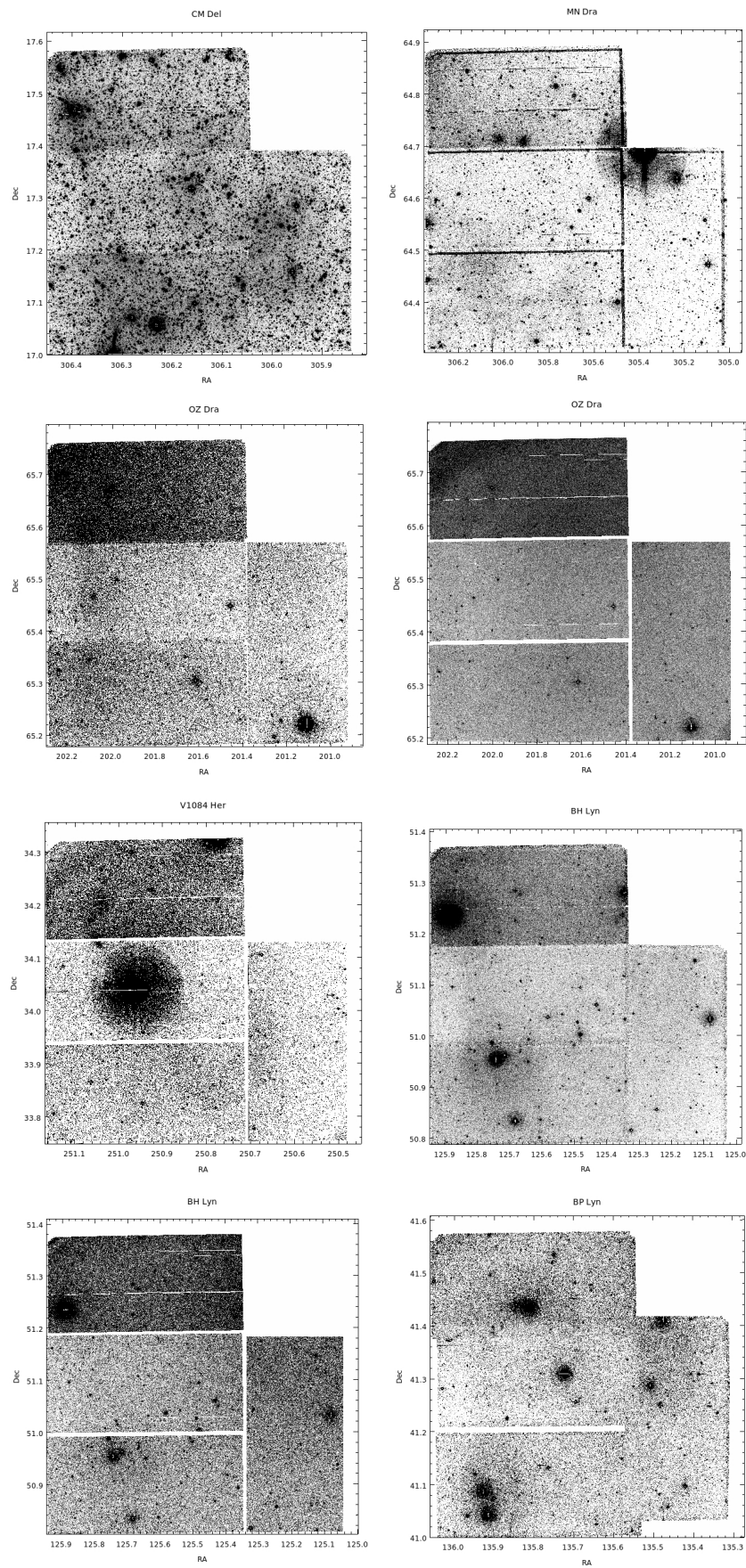


Figure B.3: See caption to Figure B.1 for details.

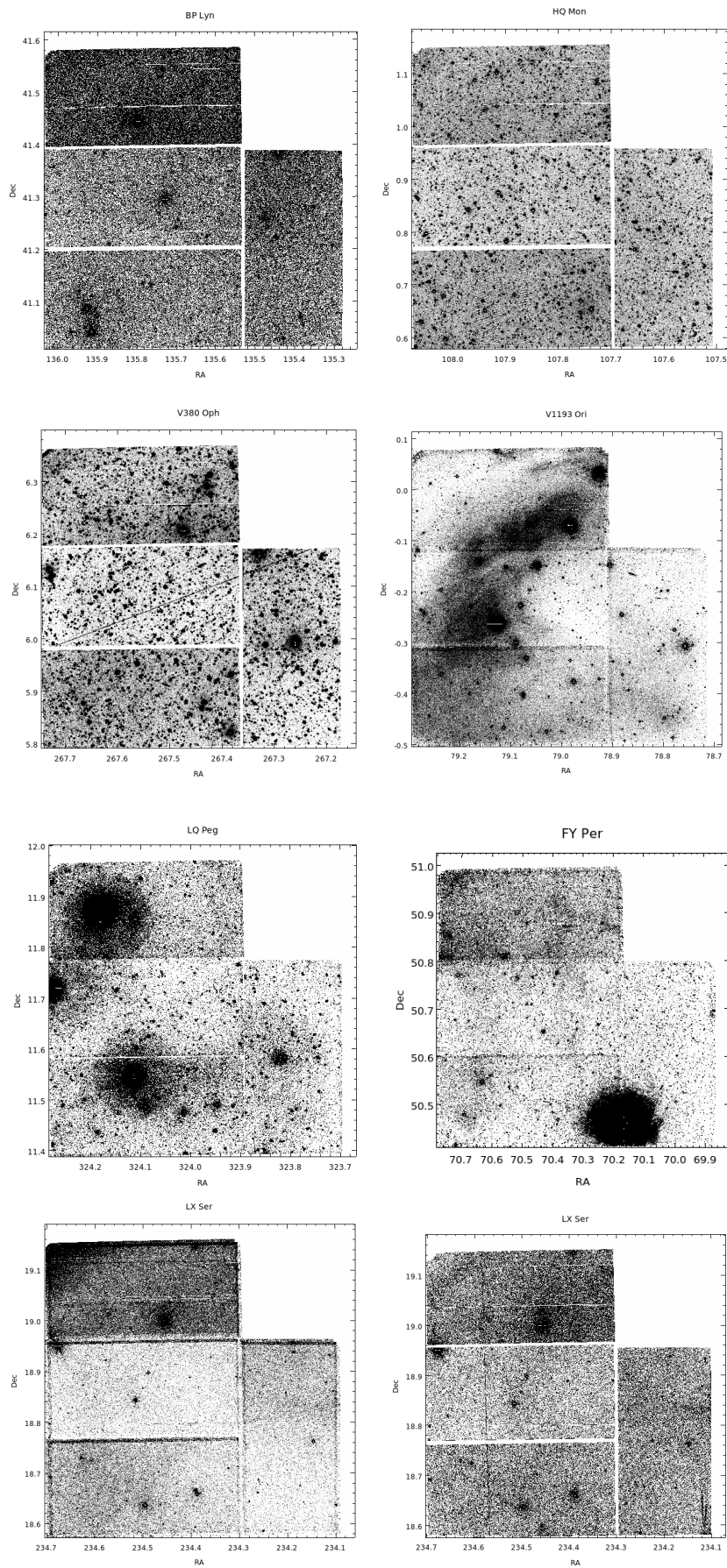


Figure B.4: See caption to Figure B.1 for details.

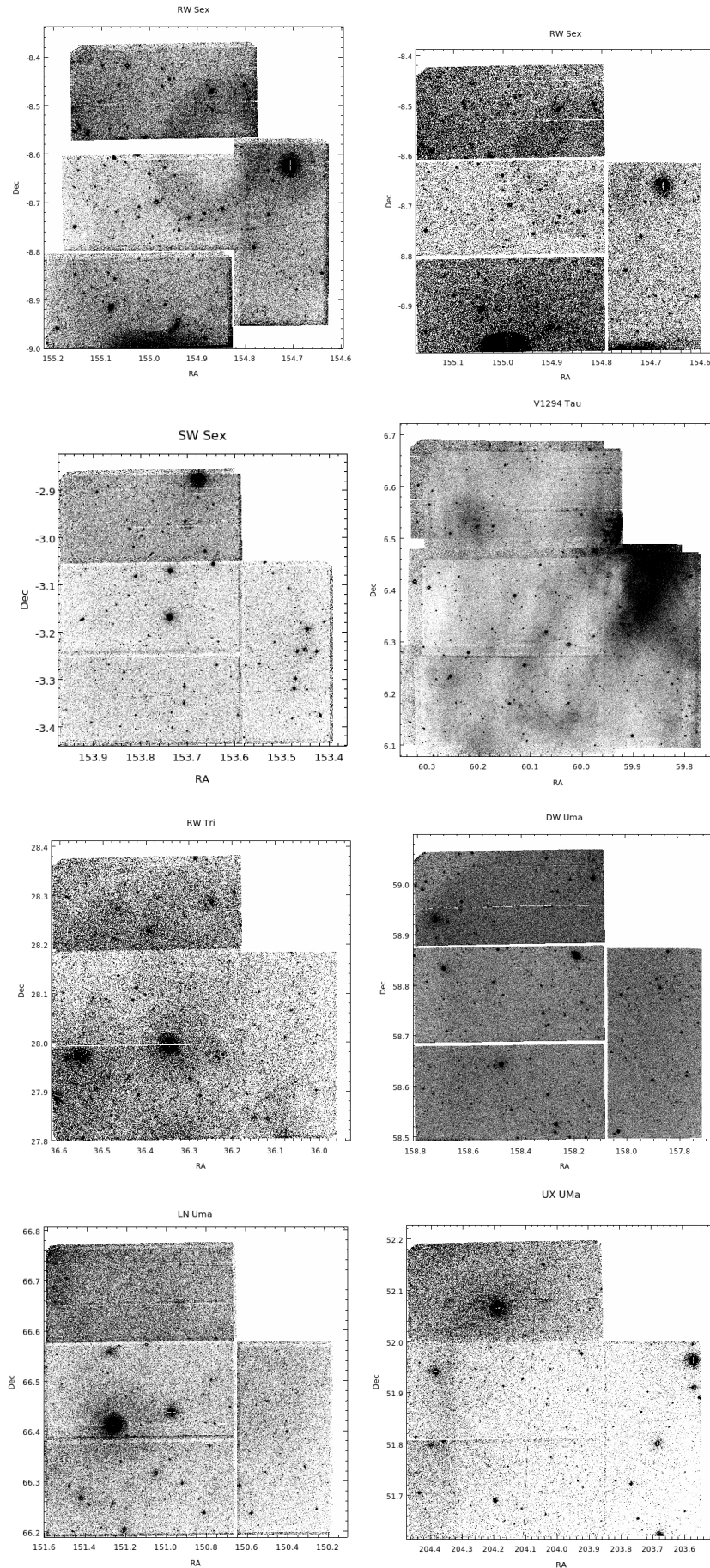


Figure B.5: See caption to Figure B.1 for details.

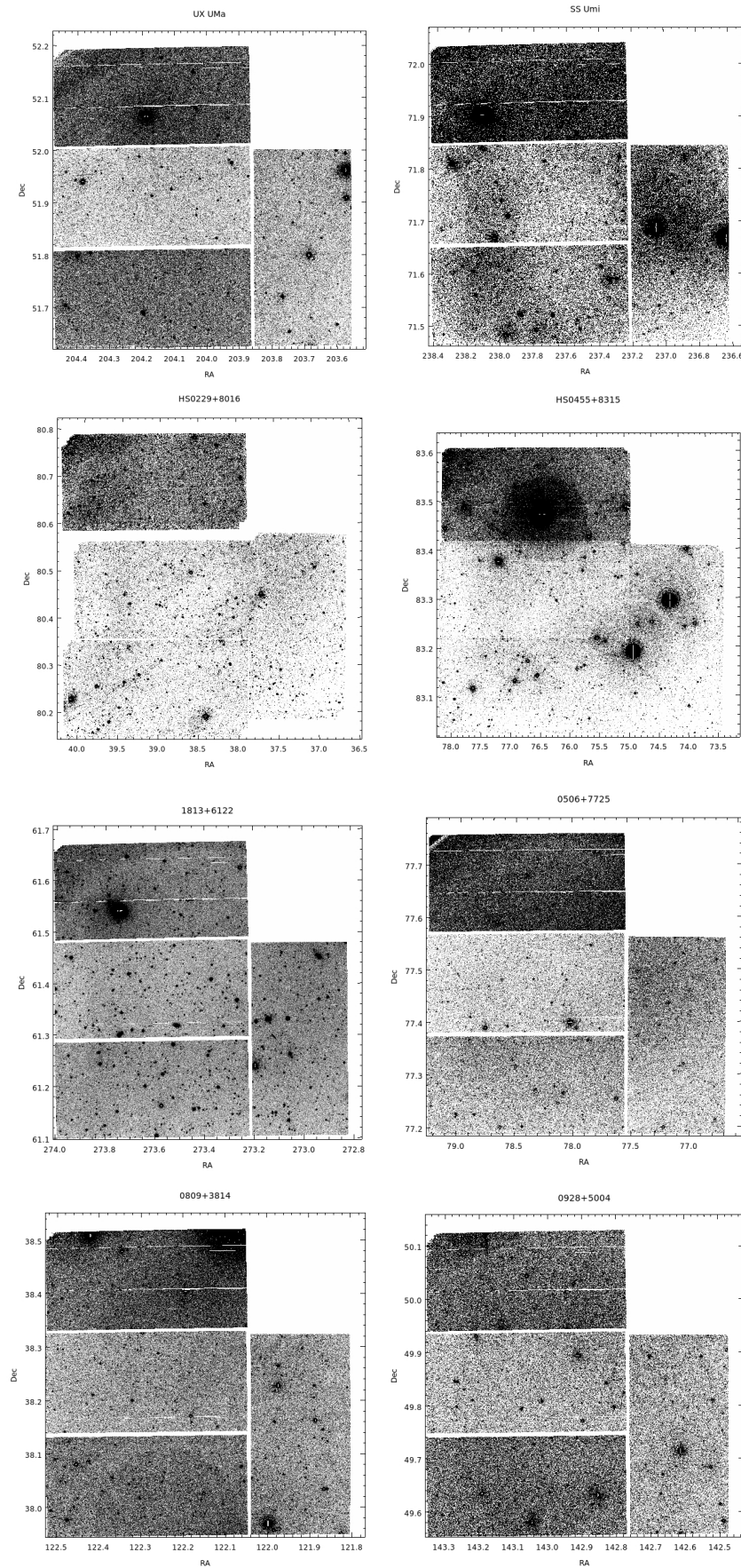


Figure B.6: See caption to Figure B.1 for details.

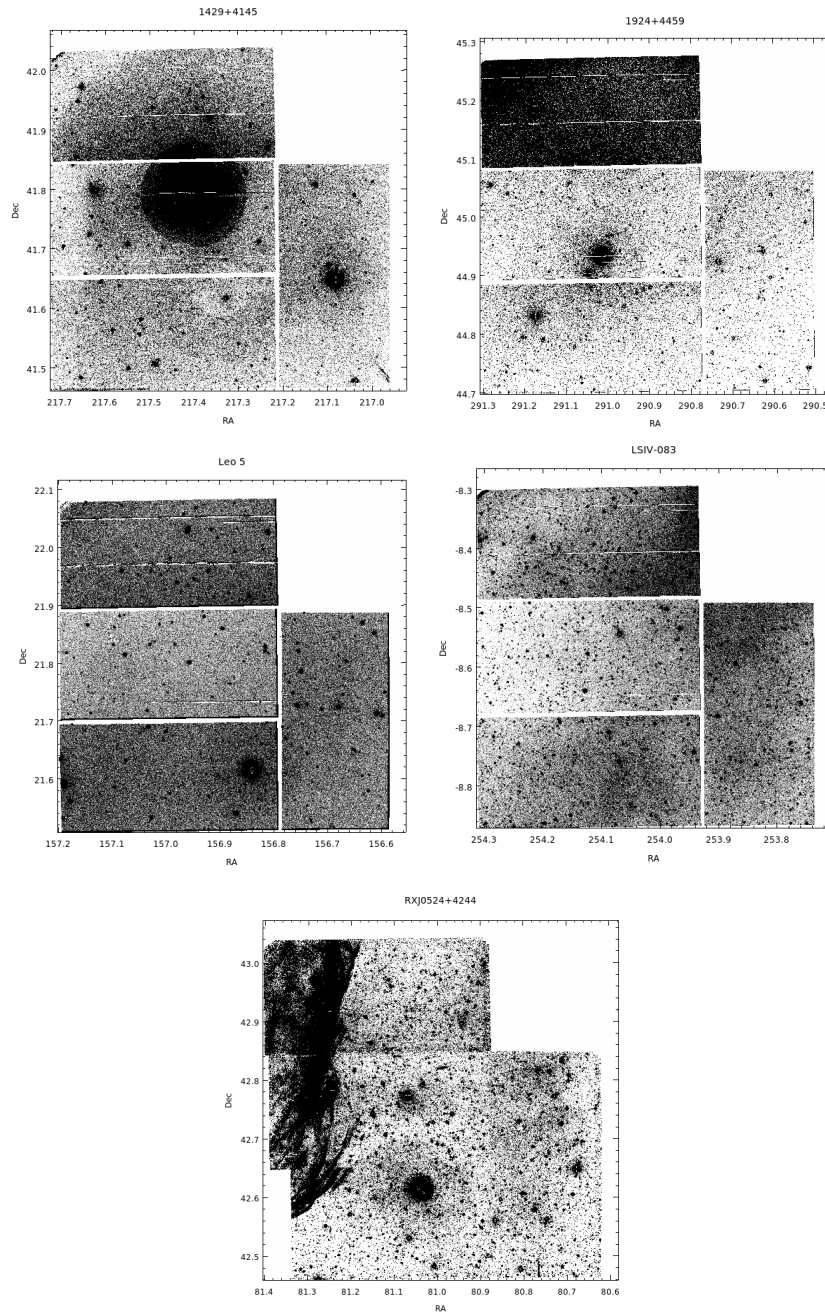


Figure B.7: See caption to Figure B.1 for details.